NORTHERN TERRITORY GEOLOGICAL SURVEY

NTGS RECORD 2019-001

Using tourmaline to identify base metal and tungsten mineralising processes in the Jervois mineral field and Bonya Hills, Aileron Province

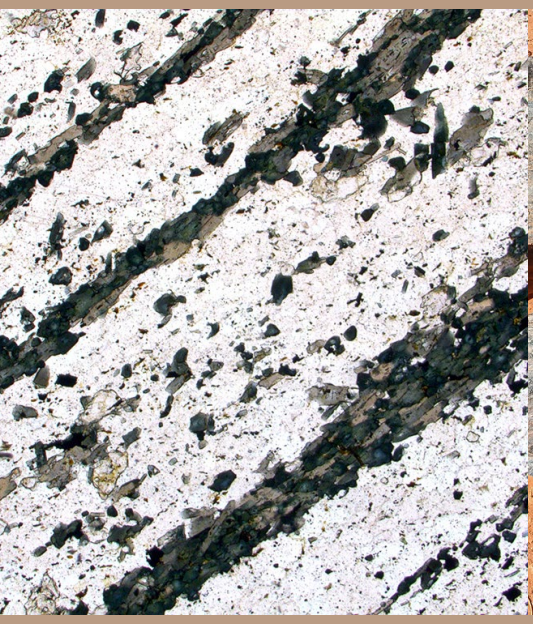

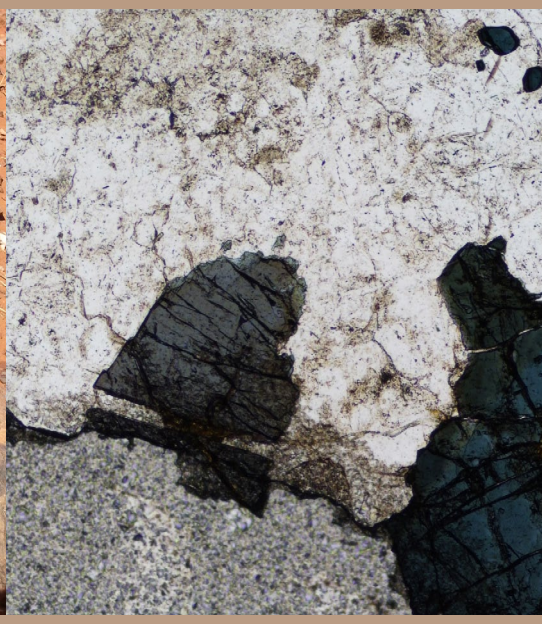

MV McGloin, A Weisheit, RB Trumbull and R Maas

NORTHERN TERRITORY GOVERNMENT

DEPARTMENT OF PRIMARY INDUSTRY AND RESOURCES
MINISTER (ACTING): Hon. Dale Wakefield, MLA
CHIEF EXECUTIVE: Alister Trier

NORTHERN TERRITORY GEOLOGICAL SURVEY
EXECUTIVE DIRECTOR: Ian Scrimgeour

BIBLIOGRAPHIC REFERENCE: McGloin MV, Weisheit A, Trumbull RB[1] and Maas R[2], 2019. Using tourmaline to identify base metal and tungsten mineralising processes in the Jervois mineral field and Bonya Hills, Aileron Province. *Northern Territory Geological Survey, Record* 2019-001.

(Record / Northern Territory Geological Survey ISSN 1443-1149)
Bibliography
ISBN: 978-0-7245-7342-4 (PDF)

Keywords: Tourmaline, Jervois mineral field, Bonya Hills, copper, tungsten, silver, lead, zinc, mineralisation, Marshall, Reward, Jericho, Samarkand, boron, isotopes, terrestrial, diagenesis, dewatering, felsic magmatism, pegmatite, vein, evaporites, Aileron Province.

EDITOR: GC MacDonald. GRAPHICS AND LAYOUT: KJ Johnston, M Fuller.

Northern Territory Geological Survey
3rd floor Paspalis Centrepoint Building
Smith Street Mall, Darwin
GPO Box 4550
Darwin NT 0801, Australia

Arid Zone Research Institute
South Stuart Highway, Alice Springs
PO Box 8760
Alice Springs NT 0871, Australia

For further information contact:
Minerals and Energy InfoCentre
Phone +61 8 8999 6443
Website: www.minerals.nt.gov.au/ntgs
Email: geoscience.info@nt.gov.au

[1] GFZ German Research Centre for Geosciences, Potsdam, Germany
[2] School of Earth Sciences, University of Melbourne, Parkville, Victoria, Australia

Using tourmaline to identify base metal and tungsten mineralising processes in the Jervois mineral field and Bonya Hills, Aileron Province

by
MV McGloin, A Weisheit, RB Trumbull and R Maas

SUMMARY

This Record documents the study of tourmaline as an indicator of palaeoenvironmental conditions and mineralising processes in the northeastern Aileron Province, central Australia. Field and petrographic observations coupled with geochemical, isotopic ($^{11}B/^{10}B$) and chronologic data have been used to constrain the origin and timing of tourmaline in tourmalinites, pegmatites, and quartz veins. The analysed tourmaline in the tourmalinites is associated with metamorphosed synsedimentary base metal and silver mineralisation in the Jervois mineral field, while the tourmaline in pegmatites and quartz veins is associated with epigenetic tungsten and copper mineralisation in the Bonya Hills area. This study provides an enhanced understanding of the mineral systems operating during the Palaeoproterozoic in the northeastern Aileron Province. The results have implications for the tectonic setting and the assessment of the mineral potential for the North Australian Craton between ca 1.80–1.70 Ga.

Tourmalinites form discrete, decimetre- to metre-wide layers in the metasedimentary, ca 1.79 Ga Bonya Metamorphics. In the Jervois mineral field, these tourmalinites are associated with metamorphosed synsedimentary, stratabound Cu–Ag–Pb–Zn mineralisation (eg Green Parrot, Marshall–Reward deposits). Layers of iron, manganese and phosphorous-rich rocks are also associated with mineralisation, all of which, along with the tourmalinites, are interpreted as metaexhalites (metamorphosed hydrothermal chemical sediments). In contrast, regionally widespread tourmaline-bearing pegmatites and tourmaline-bearing quartz veins, which post-date high-temperature, high-pressure metamorphism and deformation, are associated with epigenetic copper and tungsten mineralisation (eg Bonya copper deposit, Jericho and Samarkand tungsten prospects).

Tourmaline analysed in this study has schorl–dravite composition regardless of the associated mineralisation. However, there is some variation in Fe/(Fe + Mg) ratios between vein- and tourmalinite-related tourmaline. The boron isotopic signatures of all the tourmalinites and vein-related tourmaline samples are very low ($\delta^{11}B$ = -23.1 to -16.9‰) and cannot be separated statistically. This signature is distinctly non-marine and consistent with three possible boron sources for the tourmaline: (i) S-type granites, (ii) terrestrial evaporites, and (iii) muds containing large amounts of continental detritus that subsequently underwent diagenesis and/or metamorphism.

Field relationships and structural data indicate that the tourmalinites are stratabound and pre-date regional deformation and peak-pressure metamorphism at ca 1.76 Ga. S-type granites occur in the study area but did not form prior to 1.76 Ga, ruling them out as an epigenetic source for boron in the tourmalinites. Although processes relating to metamorphic fluids cannot be completely precluded, the simplest model for tourmalinite formation involves synsedimentary processes similar to the formation of the nearby base metal mineralisation: boron and base metals were likely transported by hydrothermal fluids that precipitated tourmaline or precursor boron-rich minerals, along with base metal mineralisation and iron–manganese in muds in a basin floor setting. Hydrothermal fluids leached boron from either (i) continentally-influenced muds that had undergone substantial diagenesis and/or low temperature metamorphism, or (ii) borate in terrestrial (non-marine) evaporites. The first interpretation is preferred based on geological evidence for a mud-rich palaeobasin in which the precursors of the Bonya Metamorphics deposited, and lack of evidence for terrestrial evaporites.

Tourmaline $\delta^{11}B$ values from the post-deformational pegmatites and quartz veins are consistent with boron exsolved from magmatic-hydrothermal fluids that are derived from S-type felsic magmatism. The oldest occurrence of S-type magmatism known from the area is post-deformational and dated to ca 1.70 Ga, providing an approximate emplacement age for the pegmatites and veins. Hydrothermal fluids associated with this magmatism (and the boron metasomatism) remobilised pre-existing base metal mineralisation and introduced epigenetic copper- and tungsten mineralisation to the study area.

The results presented in this Record have significant local and regional implications for ore-forming processes. The interpretation of continentally-derived muds deposited as part of the precursors of the Bonya Metamorphics implies that the host palaeobasin had a continentally-influenced depocentre. This interpretation also has implications for genetic and tectonic models in both the study area, and for exploration aimed at sediment-hosted base metal mineralisation in the wider Aileron Province. The proposed depositional setting is more prospective for Broken Hill-type (and volcanogenic massive sulfide mineralisation) than for most other sediment-hosted deposit styles. Also, the tourmalinite $\delta^{11}B$ values outlined in this study are amongst the lowest values known globally. They are similar to tourmaline $\delta^{11}B$ values associated with Pb–Zn–Ag mineralisation at the Broken Hill deposit, New South Wales. Currently, the low tourmaline $\delta^{11}B$ values at Broken Hill are interpreted as originating from terrestrial evaporites, a source rarely reported in tourmaline from other massive sulfide deposits and tourmalinites. Along with the tourmalinites, both the Broken Hill deposit and the Jervois mineral field also share an association with other metaexhalites (eg garnetites, magnetite-rich layers, apatite-rich layers). Also, both have gross similarities in host lithological packages (predominantly metasedimentary successions with significant components of syn–post-depositional mafic and felsic magmatism). These similarities support the interpretation that metamorphosed synsedimentary mineralisation in the Jervois mineral field has affinities to Broken Hill-type mineralisation.

TABLE OF CONTENTS

FIGURES

TABLES

APPENDIX

INTRODUCTION

Understanding ore-forming processes in present-day and ancient mineral systems helps explorers identify exploration targets with metallogenic potential. This knowledge is most useful when an ore-forming process can be translated into a mappable or measureable geological exploration target at a range of scales. However, identifying these processes in ancient ore deposits, particularly those in metamorphosed terranes, is a major challenge (eg Slack *et al* 1989, Spry *et al* 2000, Marshall and Spry 2000) because evidence for primary ore-forming processes, and the original rocks and their depositional setting, is commonly obscured by the effects of deformation, alteration and metamorphism.

In this Record, tourmaline, a common mineral in ore deposits and most geological settings, is used to identify the origin and genesis of mineralisation in the northeastern Aileron Province of central Australia, located ~270 km northeast of Alice Springs (**Figure 1**). The northeastern Aileron Province is a polydeformed and metamorphosed Palaeoproterozoic terrane hosting various styles of mineralisation (eg Scrimgeour 2013) that are locally associated with tourmaline-bearing rocks.

Tourmaline is a robust mineral capable of preserving geochemical information on primary ore-forming processes in different mineral systems (Slack and Trumbull 2011). It is mechanically and chemically stable over a large temperature and pressure range (≤725°C and 4.5 GPa); therefore, it can be used as a geological indicator because it is highly resistant to modification even during high-grade metamorphism and alteration (Henry and Dutrow 1996, Slack 2002, Dutrow and Henry 2011, van Hinsberg *et al* 2011a, van Hinsberg *et al* 2011b, Marschall and Jiang 2011).

This Record documents the examination of tourmaline from tourmalinites, tourmaline-bearing quartz veins and tourmaline-bearing pegmatites that are associated with base metal and tungsten mineralisation in the Jervois mineral field and the Bonya Hills area (**Figure 1**). All the tourmaline occurrences and related mineralisation are hosted within or cross-cut metasedimentary rocks of the ca 1.79 Ga Bonya Metamorphics (Weisheit *et al* in review). In context with their field relationships and petrographic settings, the tourmaline samples were analysed for their major element chemistry, boron isotopic composition and chronology using various techniques. In particular, the use of boron isotopes and Pb–Pb step-leach (PbSL) dating of tourmaline provide relatively new methods that complement tourmaline major element chemistry and petrographic observations. This field- and laboratory-based approach can help determine the origin and nature of tourmaline from the different mineralisation styles.

Boron isotope studies of tourmaline from different mineral deposits (eg Xavier *et al* 2008, Slack and Trumbull 2011, Mercadier *et al* 2012, Trumbull and Slack 2018) have used $^{11}B/^{10}B$ ($\delta^{11}B$) ratios as a tracer for ore-forming fluids and boron sources (eg Palmer and Slack 1989, Marschall and Jiang 2011). These studies found that original primary boron isotope ratios in tourmalines are retained in metamorphic terranes and metamorphosed deposits (eg Slack *et al* 1989, Duncan *et al* 2014) largely because of the mechanical strength, slow diffusivity and the resistance of tourmaline to chemical alteration (Henry and Dutrow 1996, Slack and Trumbull 2011). Along with boron isotopes, the major element composition of tourmalines can be used to constrain the nature and evolution of mineralising fluids (Slack 2002, Slack and Trumbull 2011).

Direct dating of tourmaline can be achieved using the K–Ar, ^{40}Ar–^{39}Ar, fission track, Rb–Sr, Sm–Nd, and Pb–Pb isotope methods (eg Lal *et al* 1977, Andriessen *et al* 1991, Chen *et al* 1996, Frei and Pettke 1996, Jiang 1998, Jiang *et al* 1999, Marschall and Jiang 2011). The variety of isotope dating techniques reflects the large number of elements retained in tourmaline (Marschall and Jiang 2011). In this study, we used the Pb-Pb (PbSL) dating method to obtain formation ages for the analysed tourmaline phases. PbSL dating has successfully been applied in other studies with tourmaline, titanite, hornblende, clinopyroxene, orthopyroxene, epidote, garnet, staurolite, magnetite and sulfides (Frei and Kamber 1995, Frei and Pettke 1996, Kamber *et al* 1998, Buick *et al* 1999, Duncan *et al* 2006, Duncan and Maas 2014). Confidence in using the PbSL dating technique can be taken from a study in the Mount Isa Inlier, Queensland in which Duncan *et al* (2006) successfully dated metamorphic and hydrothermal tourmaline. This mineralised Proterozoic terrane shares many geological similarities with the Aileron Province.

The Aileron Province is interpreted to be located at the southern margin of the North Australian Craton (NAC, eg Betts and Giles 2006, Betts *et al* 2016). The NAC is economically significant due to its large endowment of mineral wealth (eg Betts and Giles 2006; Betts *et al* 2016). However, the Aileron Province is relatively underexplored compared to the wider NAC and contains only small known mineral deposits (eg Huston *et al* 2006a, 2006b, 2006c, Scrimgeour 2013). The tectonic setting and genesis of mineralisation in the Aileron Province is poorly constrained; detailed provincial studies of mineralisation and metallogeny are rare (eg Scrimgeour 2013). The province is therefore a key area to understand the plate margin and tectonic processes involved in the evolution of the NAC, and related Palaeoproterozoic-aged mineral deposits. In the northeastern Aileron Province, previous studies on mineralisation have focused on base metal and tungsten mineralisation in both sediment-hosted and granite[3]-related settings (eg Peters *et al* 1985, Raith *et al* 2004, McGloin and Weisheit 2015, Bennett *et al* 2017).

In the Jervois mineral field (**Figure 2**), iron-, manganese-, boron-, and phosphorous-rich mineral assemblages, which form garnetites, banded iron-rich rocks, tourmalinites, and apatite-rich rocks (eg Peters *et al* 1985), all occur within 0.25–2 km of metamorphosed synsedimentary[4] Cu-Ag-Pb-Zn mineralisation. These unusual Fe-, Mn-, B- and P-rich rocks are interpreted as metaexhalites associated with basin floor alteration. Metaexhalites are hydrothermal chemical sediments (exhalites) that were subsequently metamorphosed (eg Spry *et al* 2000). Metaexhalites are commonly spatially and temporally associated with metamorphosed stratabound

[3] The term granite in this study includes granite and other felsic intrusive rocks with similar chemistry and mineralogy.

[4] The term synsedimentary is used herein to define processes occurring during active sedimentation or during diagenesis (and replacement) below or at the sediment–water interface early in the history of the host basin.

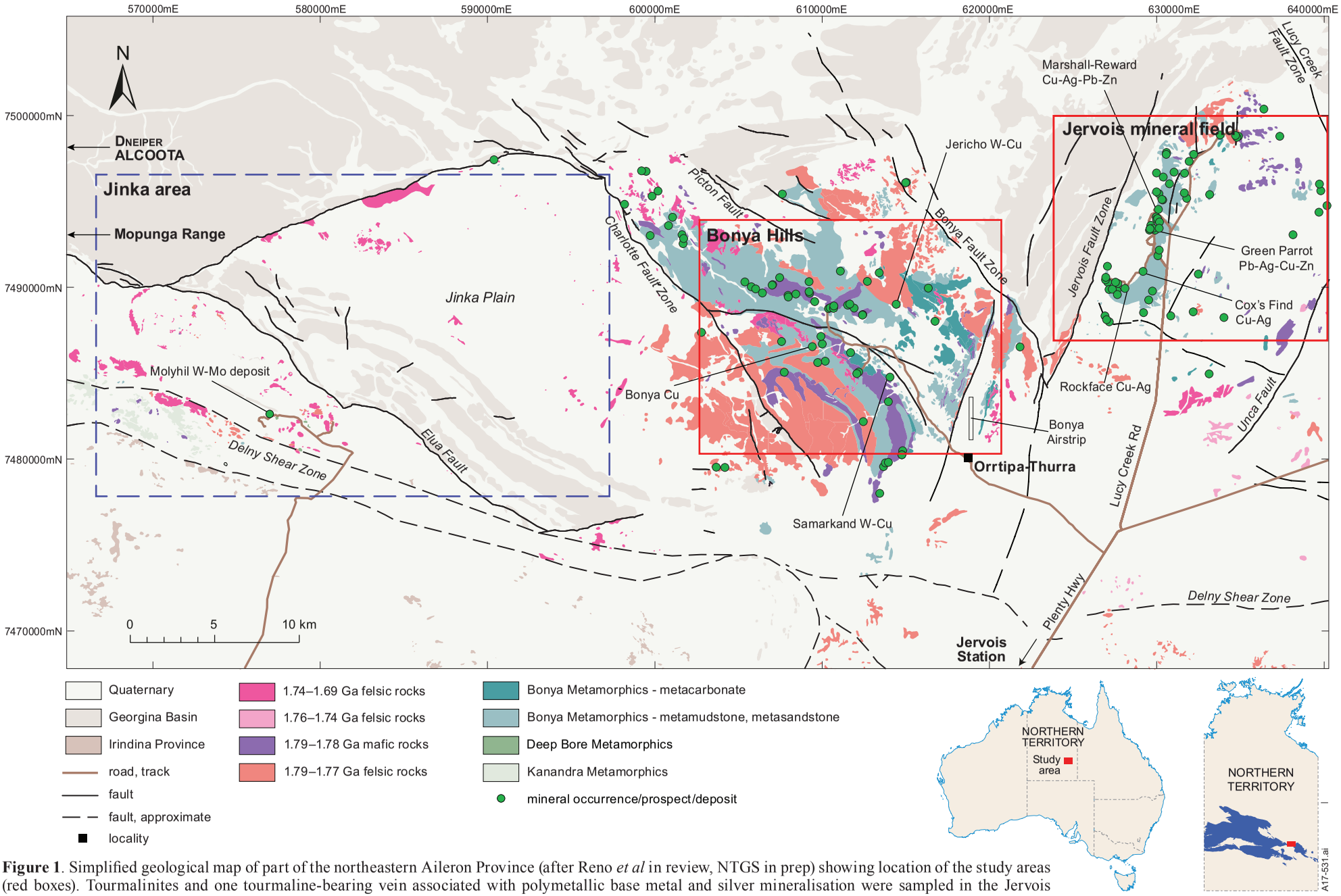

Figure 1. Simplified geological map of part of the northeastern Aileron Province (after Reno *et al* in review, NTGS in prep) showing location of the study areas (red boxes). Tourmalinites and one tourmaline-bearing vein associated with polymetallic base metal and silver mineralisation were sampled in the Jervois mineral field. In the Bonya Hills area, vein- and pegmatite-related tourmaline associated with tungsten and copper mineralisation were sampled. Skarn-related tungsten–molybdenum mineralisation also occurs in the Jinka area (blue dashed box).

massive sulfide deposits that form in subaqueous basins (eg Broken Hill-type [BHT] and volcanogenic massive sulfide deposits [VMS]; Ridler 1971, Slack 1982, Parr and Plimer 1993, Spry *et al* 2000). Metaexhalites provide evidence for relic palaeohydrothermal activity. They commonly form discrete stratigraphic layers above, below, within or along strike from exhalative mineral deposits (Spry *et al* 2000); thus, the distribution and chemistry of metaexhalites can indicate possible vectors to mineralisation and potentially record mineralising processes. Identifying metaexhalites in the Jervois mineral field therefore provides an important local guide for mineral exploration. In this study, tourmalinites from the Jervois mineral field were analysed in detail to help determine the origins of the metaexhalites and nearby base metal mineralisation. This analysis also included tourmaline from veins that overprint the host succession to synsedimentary mineralisation in the Jervois mineral field (McGloin and Weisheit in review).

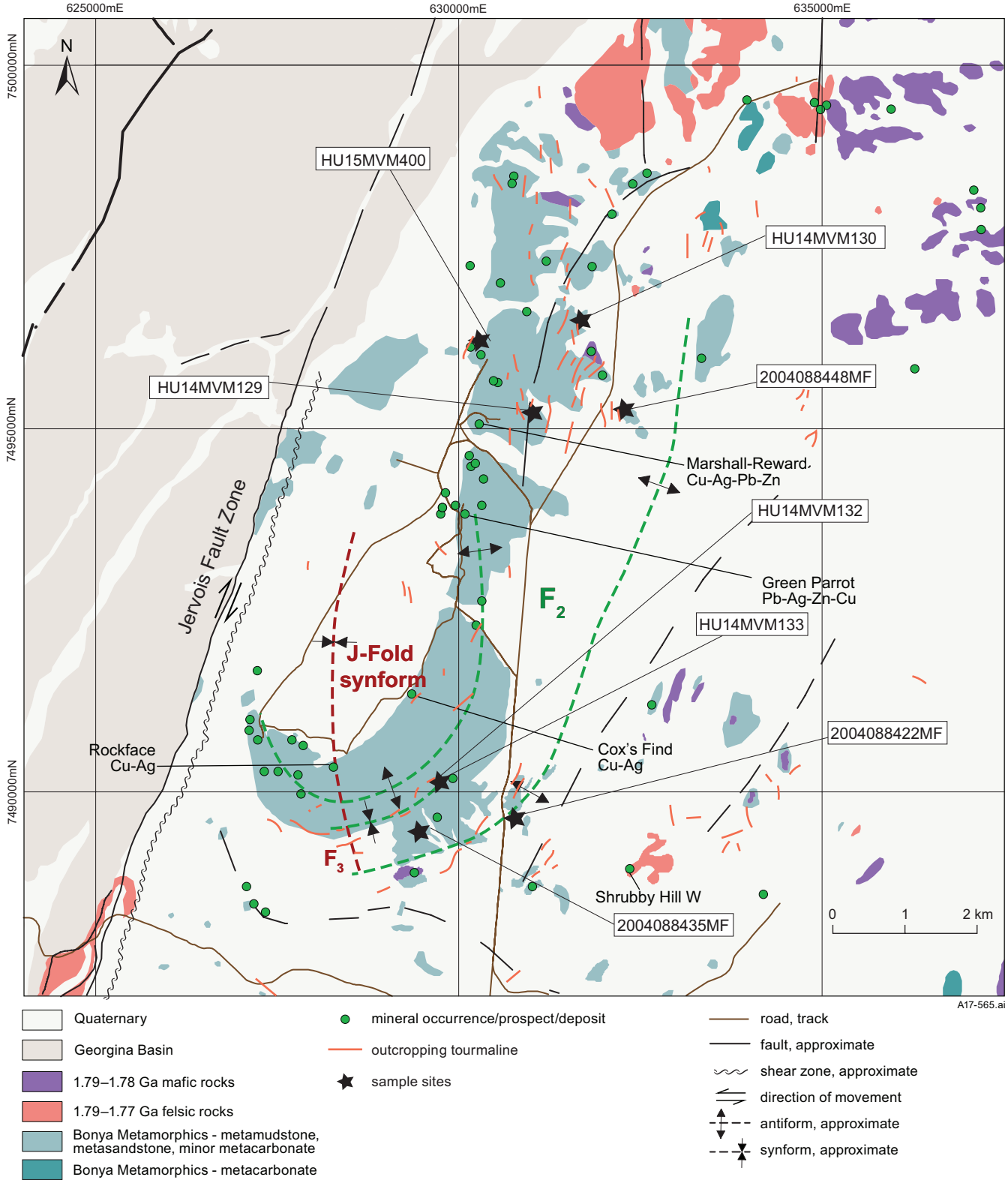

Figure 2. Simplified geological map of the Jervois mineral field. The map shows tourmaline sample locations (stars) in this study along with mineral deposits, prospects and occurrences (green dots) and structural constraints (annotated throughout). The red-coloured tourmaline sites shown are adapted from Peters *et al* (1985).

In the Bonya Hills area (**Figure 3**), only rare tourmalinites are reported (Raith *et al* 2004); these are found near epigenetic copper and tungsten prospects (rather than synsedimentary base metal mineralisation), but there is no direct association between these tourmalinites and mineralisation. However, abundant, post-deformational tourmaline-bearing pegmatites and tourmaline-bearing quartz veins (see Weisheit *et al* in review, Reno *et al* in review) do occur directly with copper and tungsten mineralisation, suggesting a genetic link between felsic magmatism, veining and this epigenetic mineralisation (Raith *et al* 2004, McGloin and Weisheit in review). This study analysed tourmaline from pegmatite and quartz veins to further characterise epigenetic mineralisation in the Bonya Hills.

GEOLOGICAL SETTING AND MINERALISATION

The northeastern Aileron Province study area (**Figure 1**) comprises a supracrustal succession that has undergone a tectonothermal cycle including regional high-thermal-gradient metamorphism, deformation, and various episodes of related felsic and mafic magmatism between ca 1.80–1.70 Ga (eg Scrimgeour 2013, Reno *et al* 2017, Weisheit *et al* in review). The oldest rocks exposed in the Bonya Hills area and the Jervois mineral field are the Bonya Metamorphics, a metasedimentary succession of metamudstone, metasandstone and metacarbonate rocks (Freeman 1986, Weisheit *et al* in review). The timing of deposition for the Bonya Metamorphics is constrained to ca 1.79 Ga (Kositcin *et al* 2015, Reno *et al* 2017, Beyer *et al*

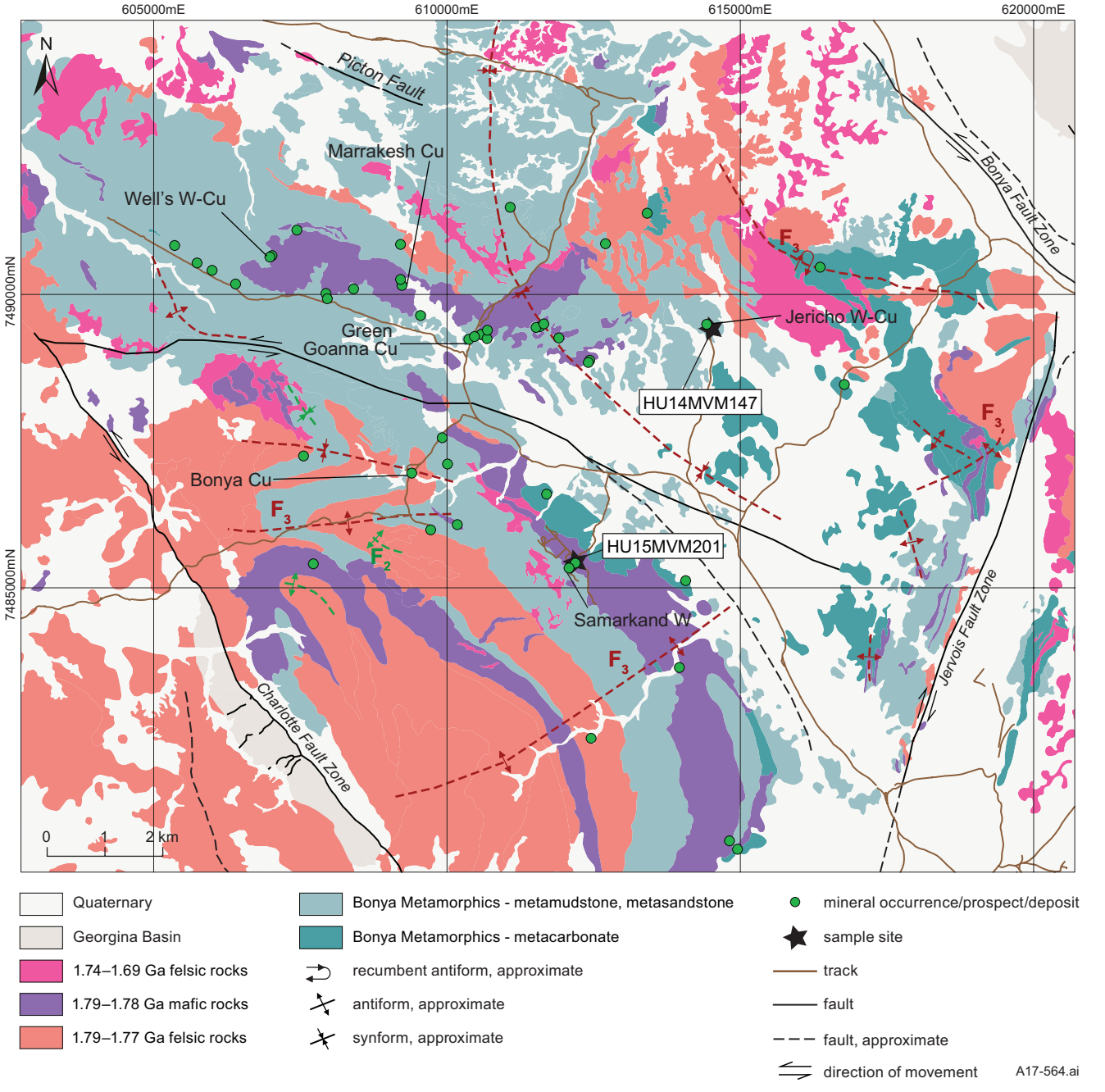

Figure 3. Simplified geological map of the Bonya Hills area (after Reno *et al* in review). The map shows tourmaline sample locations (stars) in this study along with mineral deposits, prospects and occurrences (green dots) and structural constraints (annotated throughout).

2018). The succession was intruded by voluminous igneous rocks of the Baikal Supersuite (including the Attutra Metagabbro and the Kings Legend Metadolerite, as well as associated minor diorite and granodiorite dykes and shallow level felsic intrusions) at ca 1.79–1.77 Ga (Claoué-Long and Hoatson 2005, Weisheit *et al* in review). Magmatism at ca 1.79 Ga was bimodal, contemporaneous with sedimentation and possibly emplaced under extensional conditions (D_n; "n" representing one or more deformation events; Beyer *et al* 2018, Weisheit *et al* in review). The geochemical and isotopic characteristics of the synsedimentary igneous suites are consistent with magmatism in a continental back-arc basin setting (Zhao and McCulloch 1995, Beyer *et al* 2016, Weisheit *et al* 2016, Reno *et al* 2017, Weisheit *et al* in review).

Synsedimentary mineralisation in the Jervois mineral field is hosted within the Bonya Metamorphics succession and spatially associated with the ca 1.79 Ga bimodal igneous rocks (**Figure 2**; McGloin and Weisheit 2015, McGloin *et al* in prep). Evidence from Pb model ages of metamorphosed and deformed sulfides (including galena) from the Green Parrot and Marshall–Reward deposits (**Figure 2**) suggest that the synsedimentary mineralisation formed at ca 1.79 Ga (Warren *et al* 1995, Hussey *et al* 2005), pointing to a temporal association with shallow bimodal magmatism and sedimentation (McGloin *et al* in prep). Additionally, the metaexhalites (including tourmalinites in this study) are spatially associated with the synsedimentary mineralisation (**Figure 4a-d**, eg Peters *et al* 1985). These unusual rocks form stratigraphic marker layers in the Bonya Metamorphics succession and occur in proximity to the stratabound mineralised lode sequence along a ~14 km-scale synformal fold structure ("J-Fold", **Figure 2**; eg Grainger 1967, Peters *et al* 1985, Whiting 1986, Weisheit *et al* in review).

The intrusion of the Baikal Supersuite is interpreted to have provided the heat source that initiated long-lived high-thermal gradient metamorphism in the study area until ca 1.70 Ga (Reno *et al* 2017, Beyer *et al* 2018, Weisheit *et al* in review). Peak-pressure conditions reaching amphibolite facies, occurred by ca 1.75 Ga (Reno *et al* 2016). Metamorphism was accompanied by crustal-scale thermal weakening, progressive regional deformation, and subsequent strain localisation (Weisheit *et al* 2016, 2017). This resulted in the formation of a regional gneissic to schistose main foliation (S_2) at around 1.76 Ga (Reno *et al* 2016). The S_2 foliation is axial planar to asymmetric, isoclinal folds (F_2) at cm- to km-scales (**Figures 2, 3, 4e–h**). D_2 structures overprint and locally remobilise the synsedimentary base metal mineralisation in the Jervois mineral field (**Figure 4i**, McGloin *et al* in prep, Weisheit *et al* 2016).

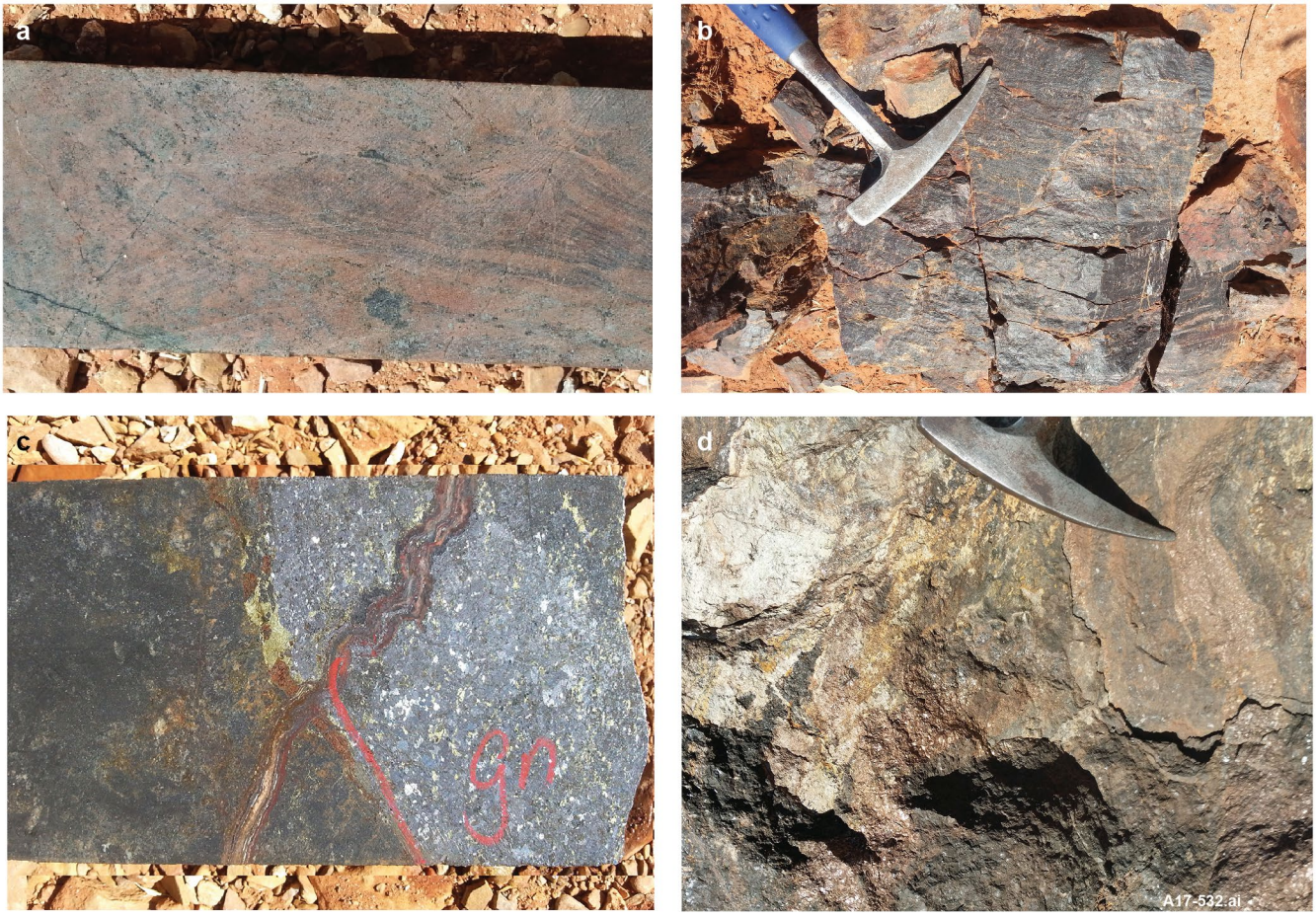

Figure 4. Field photographs showing examples of alteration, mineralisation and structures in the northeastern Aileron Province. (**a**) Zone of layered, massive Fe- and Mn-rich garnetite in drill core from the Marshall–Reward deposit in the Jervois mineral field, interpreted as originating from a hydrothermal sedimentary protolith (width of drill core = 6 cm). (**b**) 2 m wide outcrop of banded magnetite-rich rock near Cox's Find prospect in the Jervois mineral field. 33 cm long geopick for scale. (**c**) Recrystallised galena–chalcopyrite–pyrite–sphalerite–magnetite mineralisation in drill core from the Marshall–Reward deposit. Width of drill core = 6 cm. (**d**) Recrystallised and layered sphalerite-galena mineralisation exposed in Green Parrot pit. 33 cm long geopick for scale (*Figure 4 continued next page*).

Following the formation of D_2 structures and peak-pressure conditions, strike-slip movements along the bounding shear zones (eg Jervois Fault Zone, Bonya Fault Zone, Charlotte Fault Zone, **Figures 2** and **3**) are interpreted to have resulted in D_3 structures in the study area. D_3 structures range from cm-scale crenulation (**Figure 4g**) to 10 m-scale asymmetric folds (F_3) with locally developed axial planar schistosity or grain shape foliation (S_3). Ten km-scale, steeply plunging drag folds formed in the hanging walls of the bounding shear zones during D_3 (eg the J-Fold, or folds in the Bonya Hills area, **Figure 2**; Weisheit *et al* 2017, in review). The minimum age of D_3 is constrained by a ca 1.73 Ga Re–Os molybdenite age from the Bonya copper deposit (see **Figure 3**) where the host quartz vein overprints a D_3 fold structure (McGloin and Weisheit in review).

Felsic magmatism and crustal-scale fluid-flow continued in the study area until at least ca 1.70 Ga, forming I- type (derived from igneous rocks) and minor S-type granites and pegmatites (derived from sedimentary rocks) as well as widespread veining and alteration (eg Samarkand Pegmatite; **Figures 1–3;** Raith *et al* 2004, Beyer *et al* 2016, Reno *et al* 2017, Beyer *et al* 2018, Weisheit *et al* in review). The continuing magmatism likely drove and focused crustal fluids into regional and local D_2 and D_3 foliation and fold structures (Weisheit *et al* 2016). These fluids caused metasomatism of the host rocks and led to the formation of undeformed epigenetic copper and tungsten mineralisation, and extensive hydrothermal skarn and propylitic alteration (Raith *et al* 2004, McGloin and Weisheit in review, **Figures 1–3, 4i–m**). Examples of

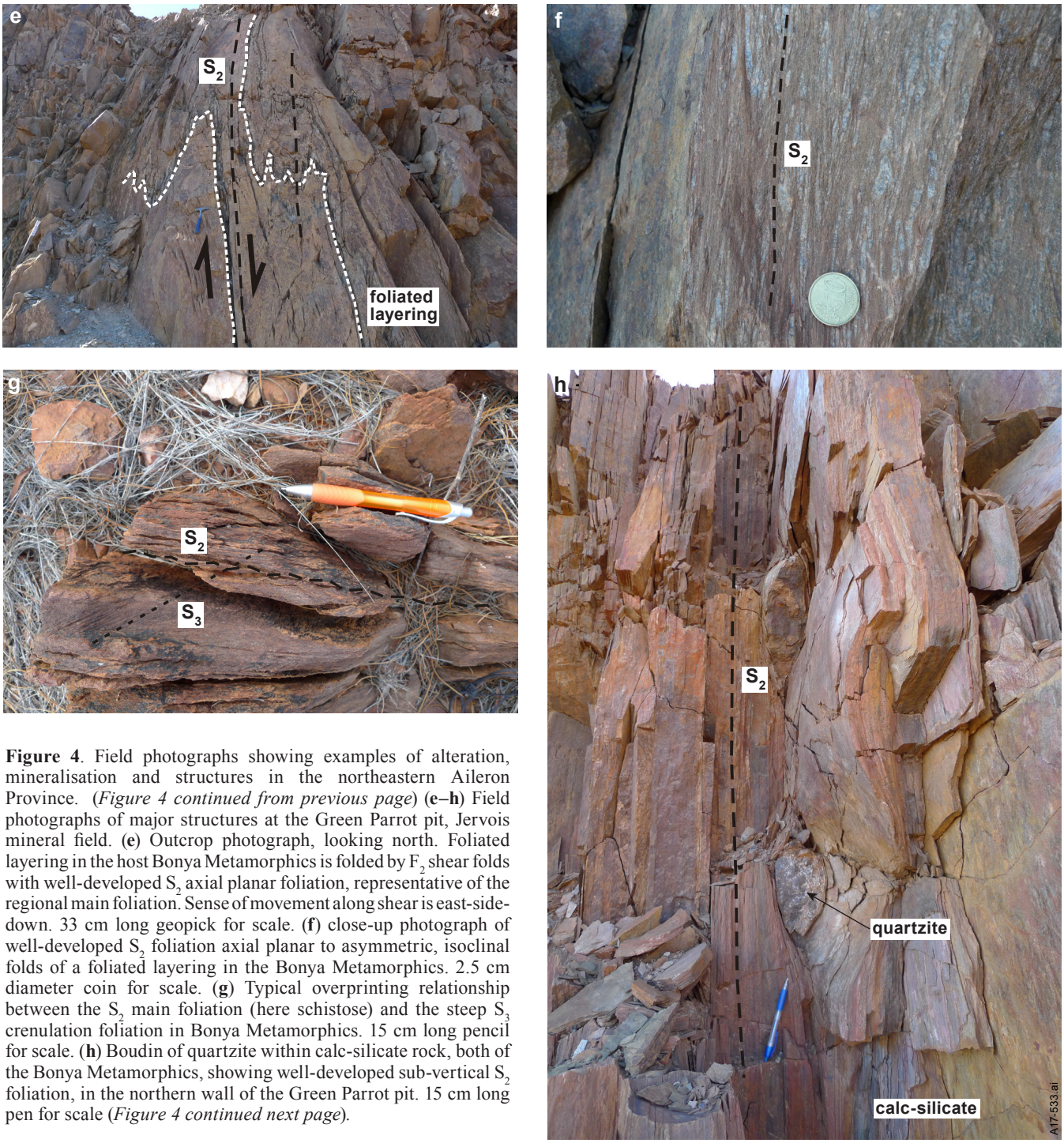

Figure 4. Field photographs showing examples of alteration, mineralisation and structures in the northeastern Aileron Province. (*Figure 4 continued from previous page*) (**e–h**) Field photographs of major structures at the Green Parrot pit, Jervois mineral field. (**e**) Outcrop photograph, looking north. Foliated layering in the host Bonya Metamorphics is folded by F_2 shear folds with well-developed S_2 axial planar foliation, representative of the regional main foliation. Sense of movement along shear is east-side-down. 33 cm long geopick for scale. (**f**) close-up photograph of well-developed S_2 foliation axial planar to asymmetric, isoclinal folds of a foliated layering in the Bonya Metamorphics. 2.5 cm diameter coin for scale. (**g**) Typical overprinting relationship between the S_2 main foliation (here schistose) and the steep S_3 crenulation foliation in Bonya Metamorphics. 15 cm long pencil for scale. (**h**) Boudin of quartzite within calc-silicate rock, both of the Bonya Metamorphics, showing well-developed sub-vertical S_2 foliation, in the northern wall of the Green Parrot pit. 15 cm long pen for scale (*Figure 4 continued next page*).

epigenetic mineralisation and alteration include the Molyhil W-Mo deposit in the Jinka area, the Bonya Cu deposit in the Bonya Hills, tungsten-bearing veins at the Jericho and Samarkand prospects, and minor copper and tungsten occurrences in the Jervois mineral field (**Figures 1–3, 4j–m**). Molybdenite from mineralisation at Molyhil and Bonya yielded Re–Os ages of ca 1.73–1.72 Ga (Cross 2007, McGloin and Bradey 2017, McGloin and Weisheit in review). Many regional examples of vein mineralisation overprint F_3 fold hinges, which indicates a post-D_3 timing for the copper and tungsten mineralisation. In the Jervois mineral field, this epigenetic mineralising episode may have also remobilised synsedimentary mineralisation and/or introduced new copper and tungsten that overprinted pre-existing synsedimentary mineralisation and alteration (eg Rockface, Marshall–Reward deposits; see **Figure 2** and **Figure 4 l–m**; McGloin *et al* in prep).

After the end of the Palaeoproterozoic metamorphism, deformation and igneous activity in the study area at ca 1.70 Ga (Reno *et al* 2017, Weisheit *et al* in review), the next recorded event was the formation of the Neoproterozoic to Palaeozoic Georgina Basin. The basin unconformably overlies the Aileron Province to the north of the Jervois mineral field and the Bonya Hills area (**Figures 1–3**, eg Kruse *et al* 2013). This sedimentation and subsequent localised high-grade metamorphism during the Larapinta Event (in the Irindina Province to the southwest of the study area; eg Hand *et al* 1999; **Figure 1**) is interpreted to have been initiated and accompanied by normal movement along the bounding shear zones (eg Greene 2010, Weisheit *et al* 2015). Compressional deformation during the Upper Ordovician to late Carboniferous Alice Springs Orogeny (eg Collins and Teyssier 1989, Scrimgeour 2013) resulted in brittle reactivation of pre-existing shear zones in the

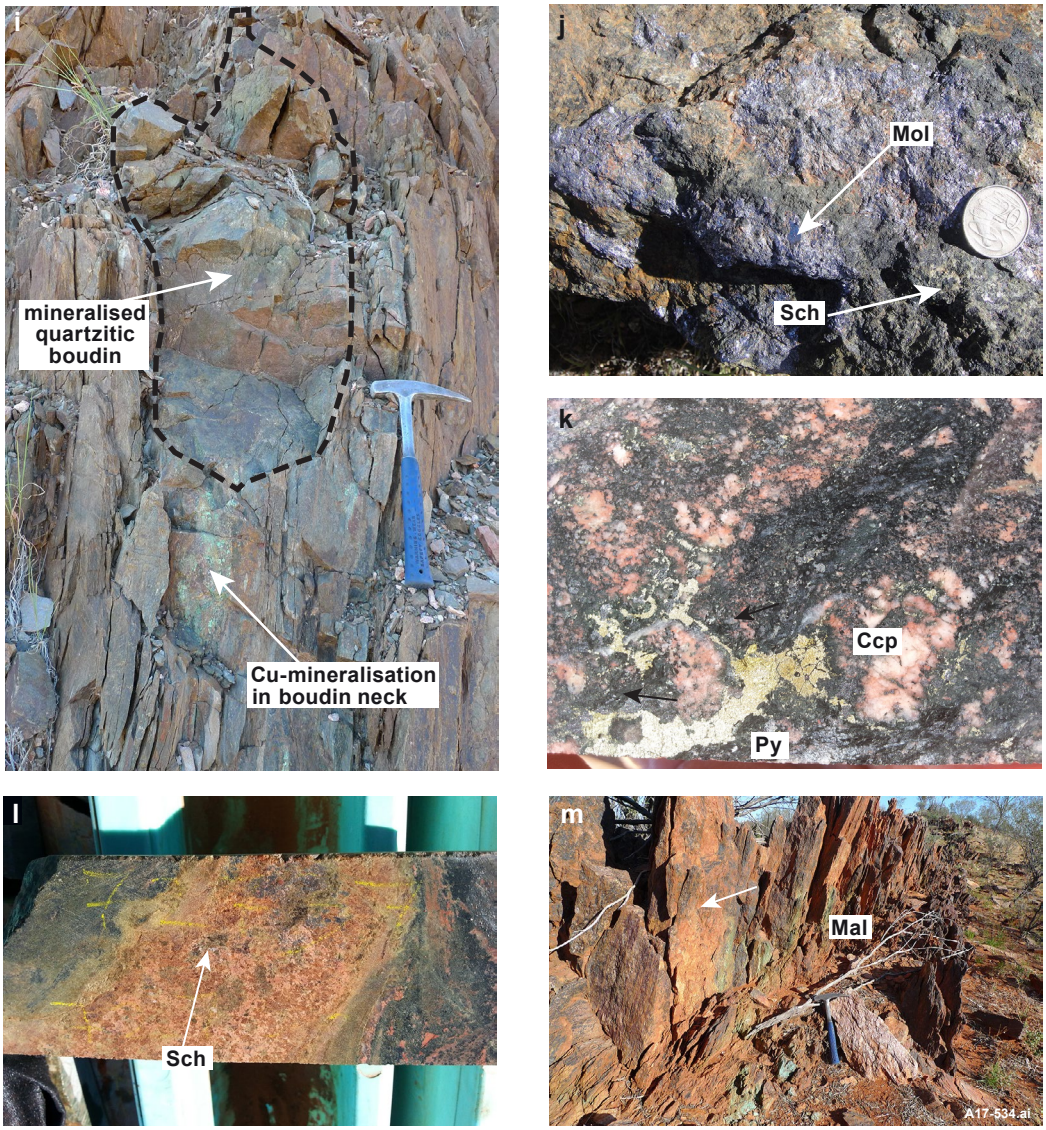

Figure 4. Field photographs showing examples of alteration, mineralisation and structures in the northeastern Aileron Province (*Figure 4 continued from previous page*). (**i–m**) Field photographs of regional mineralisation: (**i**) D_2-boudinaged copper mineralisation in a quartzitic boudin within sericite schist of the Bonya Metamorphics from the Green Parrot pit. Minor amounts of copper were remobilised during the formation of the boudin and concentrated in the dilational boudin neck. 33 cm long geopick for scale. (**j**) magnetite-scheelite (Sch)-molybdenite (Mol) skarn mineralisation from the Molyhil deposit. 2.5 cm diameter coin for scale. (**k**) Drill core from the Bonya deposit showing chalcopyrite (Ccp)–pyrite (Py) mineralisation associated with quartz veining and hematite alteration (width of drill core = 6 cm). (**l**) Drill core showing veined post-D_2 scheelite (Sch) that overprints earlier sulfide mineralisation at the Marshall–Reward deposit (width of drill core = 6 m). (**m**) Minor occurrence of vein-related post-deformational malachite (Mal) mineralisation, overprinting the S_2 foliation in the host quartz-mica-chlorite schists of the Bonya Metamorphics in the Jervois mineral field. 33 cm long geopick for scale.

study area and the juxtaposition of the Aileron Province with Georgina Basin rocks (eg Weisheit *et al* 2016, 2017, Reno *et al* 2017). Both Palaeozoic deformation events had no apparent effect on the tourmaline and mineralisation discussed in this Record.

PREVIOUS WORK ON TOURMALINE

Four previous studies have reported on field geological and structural relationships, and the petrology, composition, and genesis of tourmaline in the study area. Peters *et al* (1985) investigated tourmalinites and tourmaline veins and pods associated with stratabound mineralisation in the Jervois mineral field. Tourmaline genesis in the Jervois mineral field was also briefly discussed by Ypma (1983, 1985). Raith *et al* (2004) studied tourmaline associated with tungsten-copper mineralisation in the Bonya Hills area.

Peters *et al* (1985) identified three tourmaline phases with distinct timings hosted in the Bonya Metamorphics in the Jervois mineral field:

1. *Pre-D_2 tourmaline*: commonly associated with quartz and magnetite; occurs in thin stratiform beds that form prominent stratigraphic marker horizons extending for tens to hundreds of metres along strike. These tourmalinite beds are locally banded, and intensely folded by D_2 into tight-isoclinal folds.
2. *Post-D_2 tourmaline*: circular or oval segregations and pods ≤3 m in size that replace micaceous andalusite–cordierite-bearing schists.
3. *Syn- or post-D_3 tourmaline*: found in quartz veins that intruded along fractures and kink bands and overprint the regionally pervasive S_2 foliation and F_3 folds.

All three tourmaline phases are alkali-group composition with intermediate dravite [end member $NaMg_3Al_6(Si_6O_{18})(BO_3)_3(OH)_3OH$] to schorl compositions [end member $NaFe_3Al_6(Si_6O_{18})(BO_3)_3(OH)_3OH$], with Na>Ca and Fe>Mg (eg Henry *et al* 2011). In Peters *et al* (1985), the tourmalinites were interpreted as metamorphosed boron-rich sediments formed from submarine exhalative processes, the same processes inferred to have formed the stratabound base metal mineralisation. This interpretation was largely based on the apparent stratiform nature of the tourmalinites. No genetic models were proposed for the post-D_2 and syn- to late-D_3 tourmaline. Ypma (1983) and Ypma (1985) tentatively suggested from field observations that the tourmalinites had a continental evaporite source, with initially volcanogenic boron.

In the Bonya Hills area, Raith *et al* (2004) investigated epigenetic vein and granite-related tourmaline associated with tungsten-copper mineralisation: tourmalinised metapelite, tourmaline-bearing quartz veins and tourmaline within leucogranite and pegmatite. Stratiform, finely laminated (S_2) tourmalinite was described from only one locality and interpreted as an S_2-deformed metaexhalite. Raith *et al* (2004) also noted a close spatial association between epigenetic tourmaline-bearing rocks, felsic igneous rocks and tungsten-copper mineralisation, suggesting a genetic link. This interpretation was based on observation of tourmalinised metasedimentary rocks and tourmaline-bearing quartz veins in aureoles up to 1.5 km from leucogranite and pegmatite intrusions associated with mineralisation. Epigenetic tourmaline alteration in the Bonya Hills post-dates (overprints or cross-cuts) the main S_2 foliation fabric in the Bonya Metamorphics; tourmaline post-dates peak-metamorphism indicated by tourmaline replacement of poikiloblastic cordierite (Raith *et al* 2004).

Like tourmaline in the Jervois mineral field, all analysed tourmaline in the Bonya Hills were classified as alkali-group tourmaline (Raith *et al* 2004). Most tourmaline compositions ranged between schorl and dravite, with Na>Ca and intermediate Fe-Mg ratios (Raith *et al* 2004). The exceptions were two leucogranite-hosted tourmaline samples that trended towards the foitite end member [$\square$ ($Fe^{2+}{}_2Al$)$Al_6(Si_6O_{18})(BO_3)_3OH$][5] rather than schorl. Similar rare earth element patterns in tourmaline separates and their tourmalinised schistose host rocks were interpreted to indicate rare earth element buffering by metasedimentary protoliths, supporting a replacement origin (Raith *et al* 2004). In contrast, tourmaline from tourmaline-bearing veins and granite yielded low REE contents and more Fe-rich compositions, which indicates crystallisation from fluids associated with fractionated granitic melts. Raith *et al* (2004) concluded that the epigenetic tourmaline formed from boron-bearing magmatic-hydrothermal fluids (derived from felsic intrusions) interacting with metasedimentary country rocks.

METHODS

Fieldwork, sampling and petrography

Field reconnaissance was undertaken at ten localities encompassing the various tourmaline-bearing lithologies. These rocks were characterised to establish the relative timing of tourmaline formation compared to host stratigraphy. Representative samples were collected from localities for petrographic, geochemical and isotopic studies (**Table 1; Figures 2** and **3**). These samples were supplemented with four samples previously collected in the Jervois mineral field during NTGS fieldwork in 2004–2005 (Frater 2006). Locations cited in this Record are based on the Map Grid of Australia (MGA) zone 53K coordinates and the GDA94 map datum; they are deemed accurate to ± 10 m. Grid references are provided as UTM eastings and northings to the nearest metre. Fieldwork was conducted by foot traverse, assisted by four-wheel drive vehicles.

In the Jervois mineral field, seven outcrops were examined; all host tourmalinite interlayered with metasedimentary rocks of the Bonya Metamorphics exposed in the J-Fold (**Table 1, Figure 2**). These outcrops occur 0.25–2 km from stratabound mineralisation (**Figure 2**). Three samples of epigenetic tourmaline were collected: a tourmaline-bearing quartz vein intimately associated with pegmatite intrusions and tungsten mineralisation at the Jericho W-Cu prospect in the Bonya Hills (**Figure 3**), a tourmaline-bearing pegmatite from the Samarkand W-Cu prospect in the Bonya Hills (**Figure 3**), and a tourmaline-bearing quartz vein that overprints tourmalinite from the J-Fold in the Jervois mineral field (**Figure 2**).

[5] $\square$ denotes a cation vacancy in the X site in the structure of foitite.

Tourmaline-bearing samples of up to 1 kg weight were collected from these outcrops for petrological and laboratory studies. Coarse tourmaline crystals were separated directly from pegmatitic quartz veins and tourmaline-bearing pegmatites. Mineral assemblages were identified in polished thin sections (<30 µm) and polished 1 inch blocks using a Nikon Eclipse LV100N polarising microscope by reflected and transmitted light microscopy at the NTGS, Darwin.

Mineral phase searches to confirm sample mineralogy were performed on polished thin sections of two tourmalinite samples treated with 20 nm thick carbon coatings at the University of Tasmania, Hobart. Analyses were conducted using a FEI Quanta 600 tungsten scanning electron microscope (SEM), controlled by an automated software package (Mineral Liberation Analyser - MLA). The SEM was equipped with an EDAX Genesis 7000 energy dispersive x-ray spectrometry (EDS) system with two Sapphire SUTW Si (Li) detectors. MLA software version 3.1 was used to locate mineral phases in the sample (Fandrich *et al* 2007). This technique creates a high resolution backscattered electron (BSE) image of the thin section; mineral phases are identified by using relative BSE intensity and energy dispersive x-ray spectroscopy.

Electron microprobe analyses

Major element content in tourmaline cores and rims were measured using the Cameca SX50 electron microprobe (EMP) at the University of Melbourne. Tourmaline was analysed from three tourmalinites, one tourmaline-bearing pegmatite and one tourmaline-bearing quartz vein. Analyses were carried out on carbon-coated polished thin sections using a 35 nA electron beam, acceleration potential of 15 kV, and a 20 second background count time. A mixture of natural and synthetic standards was used for quality control. EMP results for tourmaline were based on 19 cations, 3 B cations and 4 hydroxyl groups per unit formula (Henry and Dutrow 1996, Duncan *et al* 2006). Based on previous studies of tourmalines in the same area, Fe was assumed to be ferrous (Raith *et al* 2004). Lithium was not analysed because previous studies of tourmalines from the area show negligible Li contents (Peters *et al* 1985, Raith *et al* 2004).

Boron isotope analyses

Boron isotopes in tourmaline were measured on four samples after microprobe data capture. Isotopes were measured using a Cameca 1280-HR secondary ion mass spectrometer (SIMS) at GFZ in Potsdam, Germany. Prior to SIMS analysis, samples were repolished with 1 µm alumina to remove carbon coats, cleaned with ethanol in an ultrasonic bath, and sputter-coated with 35 nm of high-purity gold. Analytical sites were ablated with a 5 nA $^{16}O^-$ primary ion beam with an energy of 13 keV and a beam diameter of 5 µm. Positive secondary ions were extracted using a +10 kV potential, with no offset voltage. Each analysis was preceded by a 90 second pre-sputtering to remove the gold coat and establish stable sputter conditions. The analyses were done in static multicollection mode using Faraday detectors; a single run consisted of twenty, 4 s integration cycles. The instrument was operated at a mass resolution $M/\Delta M \approx 2000$, which is more than adequate to separate $^{11}B^+$ and $^{10}B^1H^+$. The typical count rate for $^{11}B^+$ under these conditions was about 1.3 x 10^7 ions per second. A single analysis typically yielded a within-run uncertainty of 0.1 to 0.2‰ [1 standard deviation (1σ)[6]]. Instrumental mass fractionation (IMF) was estimated and corrected by analyses of two tourmaline reference materials, Harvard 112566 schorl and Harvard 108796 dravite (Dyar *et al* 2001). Repeated analyses of each reference tourmaline yielded an external repeatability of <0.4‰ (1σ). The combined variation of both tourmalines together was ± 0.8‰ (1σ), which is used as an estimate of the total analytical uncertainty. After correction for IMF, $^{11}B/^{10}B$ ratios in unknowns were converted to $\delta^{11}B$ values relative to $^{11}B/^{10}B = 4.04362$ for the National Bureau of Standards reference material SRM951 (Catanzaro *et al* 1970).

Pb–Pb step-leaching

Pb–Pb step-leach (PbSL) isotope analyses of four tourmaline samples (two tourmalinites, one tourmaline-bearing pegmatite and one tourmaline-bearing quartz vein) were undertaken at the University of Melbourne. Tourmaline was handpicked from 0.2–0.4 mm crushed material, in some cases after pre-concentration with sodium polytungstate (SPT) heavy liquid. Following cleaning in distilled acetone and hot distilled water, ~100 mg splits of the separates were exposed to a 6-step leach sequence involving HCl–HBr, HBr, HNO_3 and HF at 100°C (see Duncan *et al* 2006). After centrifuging, the respective leach solutions were removed from beakers, the residues rinsed and centrifuged again; the rinse was added to the leach acid. The residues dissolved completely during the HF steps.

Coarse K-feldspar from two samples of pegmatite was handpicked from 1–2 mm crushed material, cleaned with warm 0.1 M HNO_3 and distilled water, dried and hand-ground to fine sand in an agate mortar. Splits of this material (50 mg) were exposed to a 4-step acid leach procedure to remove soluble U-rich impurities and non-feldspar Pb (DeWolf and Mezger 1994, Maas *et al* 2015). The residues were dissolved in HF–HNO_3. Trace element concentrations of the feldspar residues were measured in small splits of the feldspar solutions using an Agilent 7700x quadrupole inductively coupled plasma mass spectrometer (ICP–MS). Pb was extracted from the tourmaline PbSL and feldspar residue fractions using a double pass on 0.1 ml columns of AG1-X8 (100–200 mesh) anion exchange resin (eg Kamber and Gladu 2009). Pb isotopic ratios were measured on a Nu Plasma multi collector (MC)–ICP–MS with sample uptake by aspiration through a Glass Expansion Opalmist nebulizer and CETAC-Adrius desolvating system, providing a sensitivity of around 160 V/ppm Pb. Mass bias was corrected using thallium-doping, which produces data with external precisions near ± 0.03–0.06% (2σ) for Pb signals of 5–10 V (Woodhead 2002). Total procedural blanks averaged 50 ± 20 pg Pb and blank corrections were applied accordingly (see **Results**).

[6] σ indicates the uncertainty of the measurement as specified, ie 1σ (68.3%) and 2σ (95.4%) confidence intervals.

RESULTS

Field relationships and petrological observations

The studied tourmaline occurs as three main styles: (1) tourmalinites, (2) tourmaline-bearing pegmatites, and (3) tourmaline-bearing quartz veins. The tourmaline-bearing quartz veins cross-cut both the tourmalinites and tourmaline-bearing pegmatites. This section discusses the relative field relationships and petrographic observations of the tourmaline from sample locations in the Jervois mineral field and the Bonya Hills area.

Tourmalinites and tourmaline-bearing quartz veins in the Jervois mineral field

All seven studied outcrops of tourmalinite in the Jervois mineral field (**Figure 2, Table 1**) are interlayered with metasedimentary rocks of the Bonya Metamorphics and overprinted by the sub-vertical main regional foliation S_2. Sample HU14MVM129 was collected from a ~1.5 m thick, sub-vertical, north-trending tourmalinite outcrop located ~280 m east of the sulfide-magnetite mineralised horizon at the Marshall–Reward deposit on the eastern limb of the J-Fold (**Figure 2**). This tourmalinite is fine-grained and comprises foliated, mm- to cm-scale alternating quartz- and tourmaline-rich layers (S_2, **Figure 5a**). The tourmalinite is interlayered and layer-sub-parallel with andalusite–muscovite–quartz schist of the Bonya Metamorphics, which is overprinted by the same sub-vertical S_2 foliation. Locally, the tourmalinite shows evidence for boudinage, which is characteristic of competent metasedimentary rocks that have been deformed during D_2. In places, the S_2-foliated tourmalinite and schist are cross-cut by ≤2.5 cm-wide tourmaline-bearing quartz veins. Host rocks may show muscovite alteration on contacts with these small veins.

In thin section, HU14MVM129 shows two phases of tourmaline: 1) tourmaline in mm-wide, irregular bands of tourmaline- and quartz-rich layers, both containing muscovite, magnetite, and minor chloritised biotite (**Figure 5b**); and 2) tourmaline in porphyroclasts (**Figure 5a, c**). Quartz that occurs in the compositional layering in this rock is medium-grained and undulose; it contains sub-grains and is characterised by irregular grain boundaries and weak stretching parallel to the compositional layering, indicating dynamic recrystallisation during the formation of S_2. Tourmaline is medium-grained, massive to poikiloblastic and euhedral to anhedral. Most of the tourmaline grains are aligned parallel to the layering and quartz stretching, indicating pre- to syn-deformational growth. Some tourmaline grains are only weakly aligned, or overgrow the fabric, indicating syn- to post-deformational growth (**Figure 5b**). Fine-grained muscovite (with minor biotite) dominates some layers; they are aligned with a lattice-preferred orientation parallel to the quartz-tourmaline layering. MLA and BSE imagery shows abundant apatite and magnetite (both ≤1–5% of the mineral modal abundance). Apatite appears in only some compositional layers (**Figure 5d**), whereas magnetite is distributed throughout the rock in most layers. Magnetite, occasionally martitised, appears as stretched and oriented crystals, or overgrowths to the compositional layering and S_2 foliation. BSE and MLA imaging also shows trace pyrite and accessory monazite, xenotime, titanite and zircon (**Figure 5d**), typically disseminated along grain boundaries or included in tourmaline or quartz. Thin veinlets, containing variable amounts of monazite, xenotime, magnetite, muscovite and sulfide, cross-cut the layered foliated tourmalinite. The cm-wide porphyroclast in sample HU14MVM129 contains inclusions of the same minerals as the compositionally layered matrix (**Figure 5c**). Tourmaline and muscovite are coarser-grained inside the porphyroclast compared to the matrix; muscovite is commonly altered to sericite. Zircon, monazite and titanite are similarly distributed both within and outside of the porphyroclast. A weak alignment and stretching of quartz and tourmaline inside the porphyroclast define an internal foliation, which is oblique to the external S_2 foliation in the sample. This indicates either a pre- or syn-D_2 formation of the porphyroclast.

The tourmalinite sample HU14MVM130 was collected from outcrop 650 m east of mineralisation at the Marshall–

Sample	Tourmaline type	Location	Easting (mE)	Northing (mN)
HU14MVM129	Tourmalinite	280 m east of the Marshall–Reward Cu-Ag(Pb-Zn) deposit , JMF	630630	7495107
HU14MVM130	Tourmalinite	650 m east of the Marshall–Reward Cu-Ag (Pb-Zn) deposit, JMF	631208	7495884
HU15MVM400	Tourmalinite	175m east of the northern Reward mineralised horizon, JMF	630563	7495670
HU14MVM132	Tourmalinite	Near Cox's Find prospect, JMF	629896	7490231
HU14MVM133	Tourmaline–bearing quartz vein cross-cutting tourmalinite	Near Cox's Find prospect, JMF	629896	7490231
HU14MVM147	Tourmaline–bearing quartz vein	Jericho W-Cu prospect, BH	614491	7489414
HU15MVM201	Tourmaline-bearing pegmatite	Samarkand W-Cu prospect, BH	612180	7485442
2004088422MF	Tourmalinite	Near Chubko, JMF	630730	7489780
2004088435MF	Tourmalinite	Near Chubko, JMF	629560	7489690
2004088447MF	Tourmalinite	East of Marshall-Reward, JMF	631850	7495165
2004088448MF	Tourmalinite	East of Marshall-Reward, JMF	631850	7495165

Table 1. Location of sampled tourmaline occurrences. Sample coordinates are referenced to the Map Grid of Australia 1994 (MGA94), Zone 53. JMF = Jervois mineral field, BH = Bonya Hills.

Reward deposit (**Figure 6a**). At this location, a 1 m-wide, sub-vertical, north-trending tourmalinite layer is interlayered within andalusite–muscovite–quartz schist of the Bonya Metamorphics (**Figure 6a**). The sampled tourmalinite is cross-cut by a small <20 cm-wide tourmaline-bearing quartz vein. The vein cuts the sub-vertical, layer-parallel S_2 foliation in the host rock and other tourmalinites locally (**Figure 6b**).

In thin section, tourmalinite sample HU14MVM130 consists of irregular tourmaline-quartz layering (**Figure 6c**) with minor muscovite and chloritised biotite. MLA and BSE imagery shows abundant magnetite and apatite grains (about 10% and 5% mineral mode, respectively), which commonly form layered bands similar to quartz and tourmaline (**Figure 6d**). The petrology of sample HU14MVM130 is distinct from sample HU14MVM129. Tourmaline in HU14MVM130 is finer-grained, massive and anhedral in shape. Magnetite, occasionally martitised, is more abundant; it mostly occurs as bands concentrated within the tourmaline-rich layers (**Figures 6c–d**). There is less muscovite and sericite than in sample HU14MVM129. Quartz is characterised by similarly irregular grain boundaries and undulose texture, indicative of dynamic recrystallisation. In contrast to sample HU14MVM129, no foliation parallel to compositional layering was observed in sample HU14MVM130. Compositional layering is however crenulated at the mm-scale with rare development of axial planar alignment and recrystallisation of the tourmaline and quartz, and some axial planar shear zones, typical for D_3 structures (**Figure 6c**). HU14MVM130 contains very minor traces of chalcopyrite and pyrite. Accessory minerals, including zircon, titanite, monazite and xenotime, are disseminated in the matrix. One hematite-bearing quartz vein was observed cross-cutting the crenulated layering.

Sample HU15MVM400 was collected from subcrop comprising tourmalinite (**Figure 7**) interlayered within sub-vertical, north-trending muscovite–quartz schist of the Bonya Metamorphics. This tourmalinite occurs <30 m from small costeans that expose minor scheelite mineralisation in skarnoid metacarbonate rocks of the Bonya Metamorphics

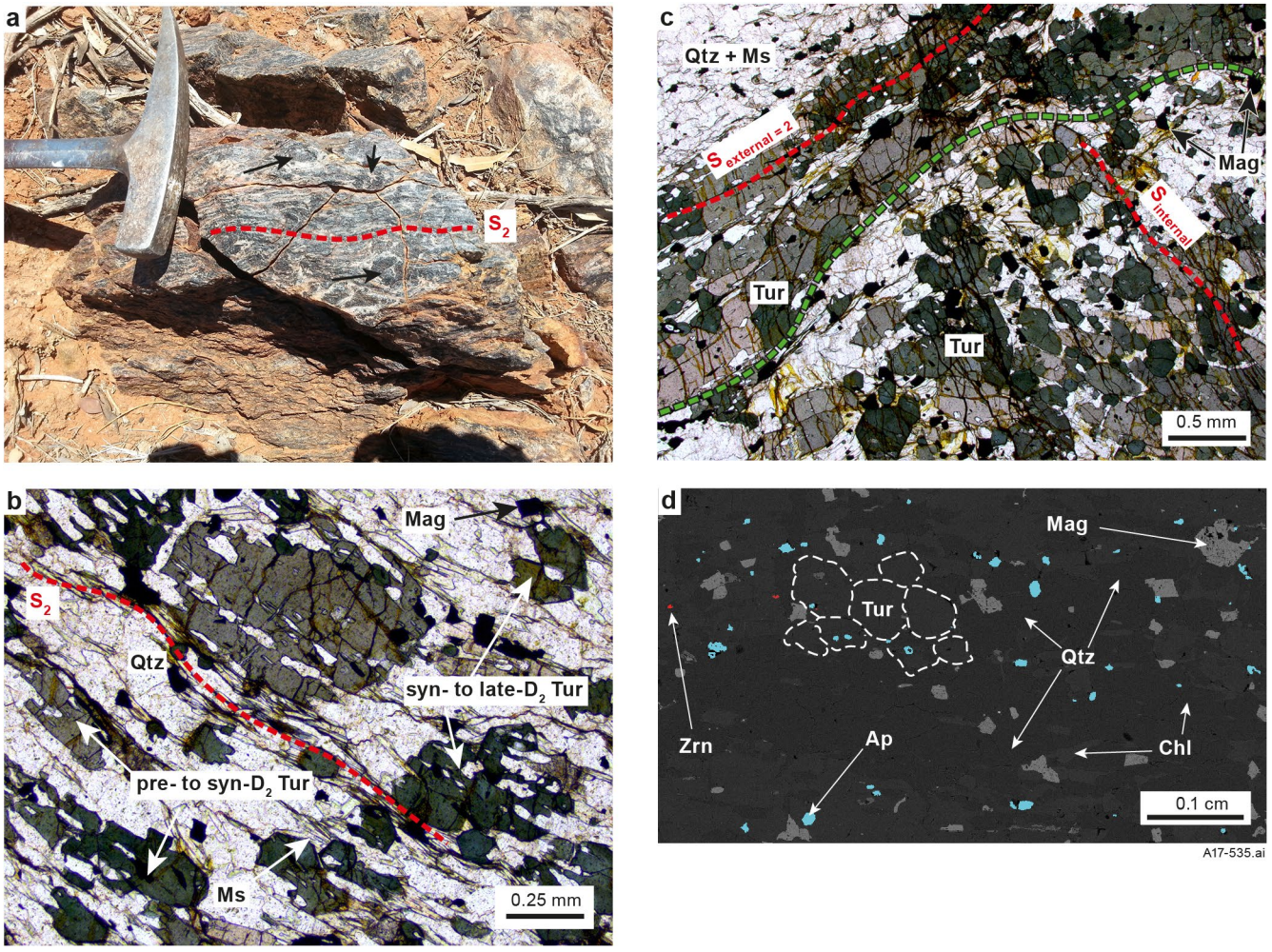

Figure 5. Outcrop and petrographic photos of tourmalinite sample HU14MVM129. (**a**) Outcrop of tourmalinite interlayered within andalusite–muscovite–quartz schists of the Bonya Metamorphics near the Marshall–Reward deposit. The sub-vertical, south-trending main foliation S_2 (red dashed line) is subparallel to the lithological boundary with the mica schist (not seen in image). Concretions of tourmaline and quartz form porphyroclastic structures in the tourmalinite (black arrows). 19 cm long head of geopick for scale. (**b**) Photomicrograph taken under plain light indicating that the main foliation S_2 in the sample is parallel to a weak compositional layering of tourmaline–quartz±muscovite–magnetite. Euhedral to anhedral, poikiloblastic tourmaline occurs deformed or overgrowing; it is interpreted to have grown both pre- to syn-deformation and syn- to post-deformation. (**c**) Photomicrograph taken under plain polarised light of a mm-sized porphyroclast of tourmaline, quartz, muscovite and magnetite (downright of the green dashed line) surrounded by a compositionally layered and deformed matrix of the same minerals (above green dashed line). A weak internal foliation is oblique to the external S_2 foliation. (**d**) MLA image of a thin section showing the typical mineral assemblage and paragenetic relationships. This image highlights the occurrence of apatite (blue) and zircon (red). Ap = apatite, Chl = chlorite, Mag = magnetite, Ms = muscovite, Qtz = quartz, Tur = tourmaline, Zrn = zircon.

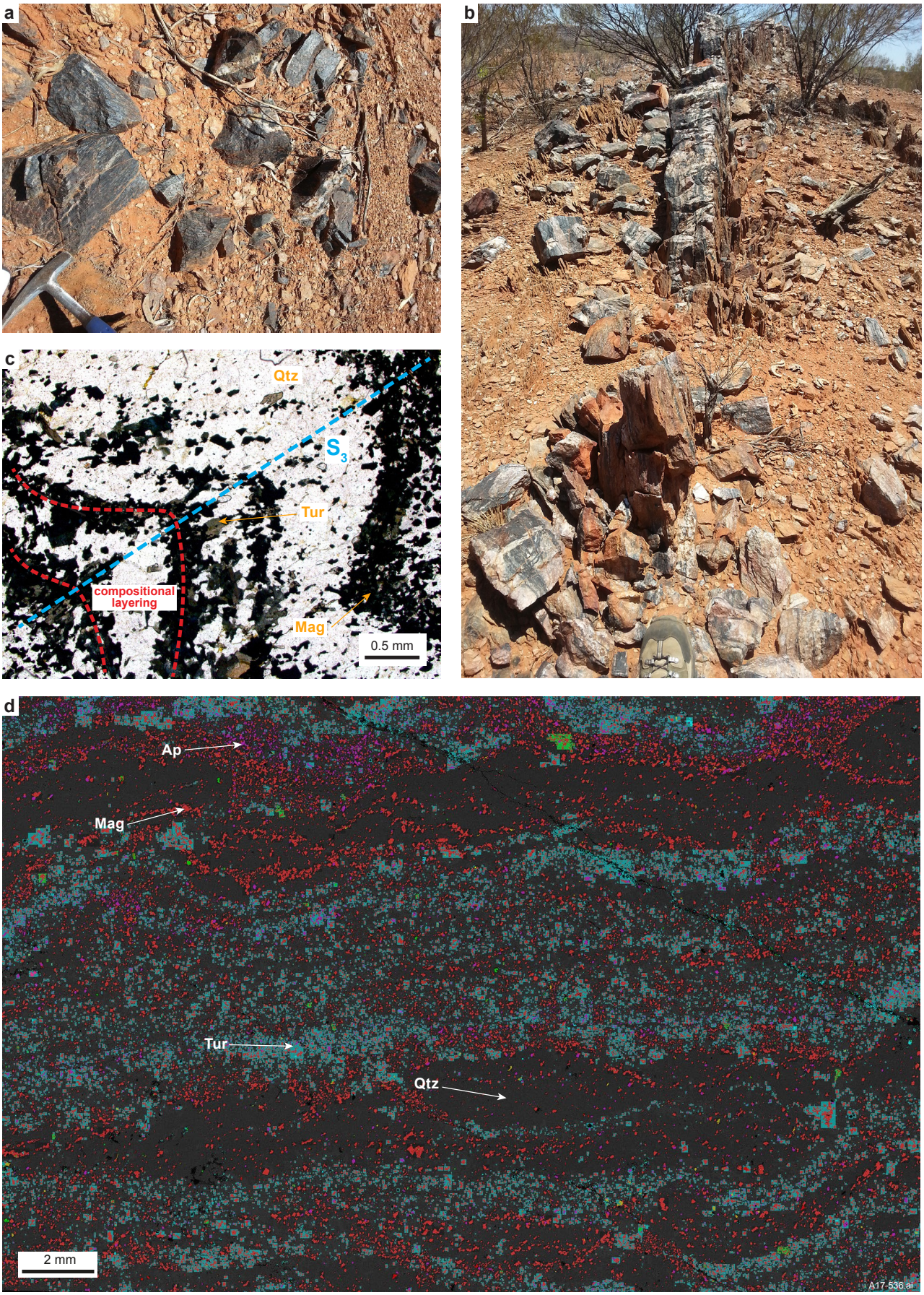

Figure 6. Outcrop and petrographic photos of tourmalinite sample HU14MVM130. (**a**) Subcrop of layered tourmalinite with S_2-foliation and minor cross-cutting tourmaline-bearing quartz vein. 19 cm long head of geopick for scale. (**b**) Image of larger tourmaline-bearing quartz vein nearby to the sampled outcrop (width of vein = ~35 cm). The vein slightly cross-cuts the S_2-schistosity in the host Bonya Metamorphics. (**c**) Photomicrograph taken under plane light of the tourmalinite of Fig. 5a. Compositional layers of fine-grained, anhedral tourmaline (Tur)-magnetite (Mag) and quartz (Qtz) ±muscovite are crenulated; a weak axial planar foliation (S_3) is developed. (**d**) MLA image of a thin section showing compositional layering of tourmaline (Tur; light blue zones), quartz (Qtz; black), magnetite (Mag; red) and apatite (Ap; purple).

(**Figure 2**). This location is also 175 m east of a base metal mineralised layer north of the Marshall–Reward deposit. The tourmalinite of sample HU15MVM400 has a similar strike to that of HU14MVM129, trending sub-vertically north-south. Also like HU14MVM129, the tourmalinite is characterised by mm- to cm-thick, foliated, quartz- or tourmaline-dominant layers containing cm-sized quartz-tourmaline porphyroclasts (**Figure 7**; see **Figure 5a, c**). The field relationships demonstrate a consistent geological setting for the different tourmalinite outcrops in the Jervois mineral field.

Sample HU14MVM132 was collected from a tourmalinite that outcrops ~1.1 km southeast of Cox's Find Cu-Ag prospect and ~1.5 km east of Rockface Cu-Ag deposit (**Figure 2**). At this location, the sub-vertical tourmalinite trends northeast-southwest and reaches thicknesses of ≤10 m. The tourmalinite is interlayered with muscovite–quartz schist of the Bonya Metamorphics (**Figure 8a**). A polished thin section of sample HU14MVM132 contains foliated bands of quartz and tourmaline with minor oriented muscovite and abundant apatite and magnetite **(Figure 8b,c)**. Quartz and tourmaline are recrystallised, aligned and weakly stretched in the S_2 foliation, parallel to the sub-mm to cm-wide layering. Quartz-rich layers are isoclinally folded by F_2. As with sample HU14MVM129, the tourmaline in HU14MVM132 occurs in three phases. Older, pre-D_2 tourmaline occurs as fine-grained layers of rounded and zoned crystals that are folded isoclinally with quartz-rich layers. Younger, syn-D_2 tourmaline occurs as medium-grained, elongate crystals containing inclusions of the pre-D_2 tourmaline (**Figure 8b**). Both tourmaline phases contain inclusions of the matrix minerals. HU14MVM132 is crenulated; locally pre-existing tourmaline is remobilised and is oriented parallel to the fold axial plane, forming an S_3 foliation (**Figure 8c**). Minor phases of hematite, pyrite and chalcopyrite are identified in the sample overprinting these structures. Some pyrite, chalcopyrite and magnetite sits in the cleavage plane of S_2 foliated muscovite.

Sample HU14MVM133 was collected from a large metre-wide tourmaline-bearing quartz vein that cross-cuts the foliated tourmalinite sampled in HU14MVM132 at the same outcrop (**Figure 9a**). A thin section of sample HU14MVM133 shows ≤1 cm wide, euhedral and subhedral tourmaline hosted within a coarse-grained quartz vein (**Figure 9b**). Some of these tourmalines show evidence for zonation, with light blue bands in the tourmaline cores. Traces of magnetite-ilmenite, with very minor pyrite and chalcopyrite, occur in the sample. In contrast to other samples, HU14MVM133 lacks chlorite, muscovite and sericite.

This study also examined four polished thin sections from historical NTGS sampling of tourmalinites interlayered within metasedimentary rocks of the Bonya Metamorphics, which were collected near the Rockface deposit in the Jervois mineral field (Frater 2006; **Figures 2** and **10, Table 1**). Outcrop photographs were not available for these locations. In thin section, samples 2004088422MF, 2004088435MF and 2004088447MF show regular, variably thick, cm- to mm-scale S_n layering of tourmaline–quartz±muscovite that is overprinted by a weak to pervasive S_2 foliation (**Figure 10a-c**). Sample 2004088448MF contains S_2-foliated and S_3-crenulated quartz-tourmaline layers with a cm-sized cluster of pure tourmaline, indicating that tourmaline replacement was not uniform across the original host rock (**Figure 10d**).

Tourmaline-bearing pegmatites and tourmaline-bearing quartz veins in the Bonya Hills

Sample HU14MVM147 was taken from a tourmaline-bearing quartz vein at the Jericho W-Cu prospect located ~15 km northwest of Orrtipa-Thurra in the Bonya Hills area (**Figure 3**). This vein contains minor muscovite and K-feldspar-rich selvages. It is one of several north-south trending extensional veins exposed within quartz–mica±andalusite schist and calc-silicate rocks of the Bonya Metamorphics. The vein is exposed in the centre

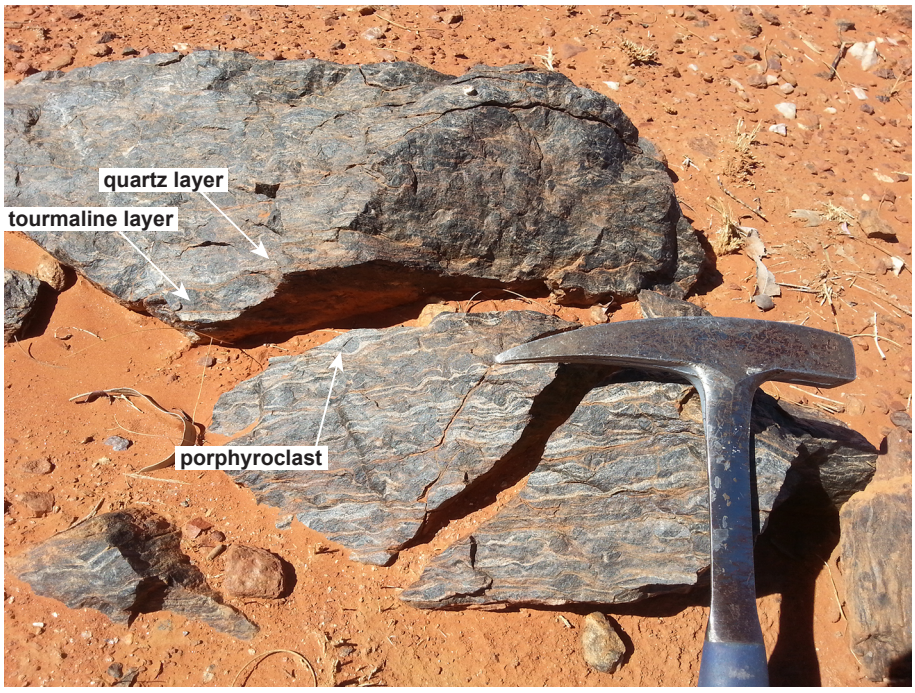

Figure 7 Photo of site location of HU15MVM400 showing a subcrop of quartz-tourmaline rock comprising a foliated layering S_2. Aggregates of tourmaline and quartz form porphyroclasts similar to sample HU14MVM129 (see **Figure 5a,c**). 19 cm long head of geopick for scale.

of a 100 m x 20 m north-south trending costean. In this area, tourmaline-bearing quartz veins are undeformed (**Figure 11a,b**) and developed in brittle tension fractures parallel to (but overprinting) the main S_2 foliation. The veins are spatially associated with a large muscovite–tourmaline-bearing pegmatite intrusion that cross-cuts the foliated host rocks. The pegmatite and veins are intimately associated with scheelite (partly oxidised to powellite), and chalcopyrite and pyrite mineralisation (oxidised to malachite and hematite), which is exposed in the costean (and nearby abandoned ore dumps). This mineralisation is disseminated and replaces metasedimentary rocks where pegmatite intrudes coarse-grained, altered calc-silicate rock (producing epidote, garnet and diopside skarn assemblages), or less frequently, andalusite–quartz–muscovite schist that is commonly hornfelsed. Much of the surrounding mica-schist at the prospect has been strongly tourmalinised by the pegmatite intrusion. A one-inch polished block of sample HU14MVM147 contains euhedral greenish-blue tourmaline hosted within a pegmatitic quartz vein (**Figure 11c**). Minor sericite and fluorite were identified along mineral boundaries.

Sample HU15MVM201 was taken from a tourmaline-bearing pegmatite at the Samarkand W-Cu prospect, located ~3 km southeast of Bonya copper deposit in the Bonya Hills area (**Figure 3**). At the Samarkand prospect, numerous north-south trending pegmatites intrude quartz–muscovite schist and calc-silicate rock of the Bonya Metamorphics at the contact with mafic intrusions of the Kings Legend Metadolerite. Some of the schist and calc-silicate rock is locally tourmalinised. The calc-silicate rock is overprinted by a sub-vertical, northwest dipping regional S_2 foliation, which is cross-cut by pegmatites and associated epidote-, garnet- and tourmaline-bearing quartz veins. The sampled pegmatite was taken from a costean where patchy malachite and trace chrysocolla and scheelite mineralisation are visible in boulders. The sampled green mica–muscovite-bearing pegmatite is coarse-grained with a graphic texture (**Figure 12a, b**) and contains abundant coarse-grained tourmaline crystals (≤4 cm long) intergrown with the other minerals.

Tourmaline mineral chemistry

Average compositions of tourmaline in the tourmalinites, tourmaline-bearing pegmatite and tourmaline-bearing quartz veins are listed in **Table 2**. Most of the analysed tourmalines are saturated or oversaturated in aluminium relative to end member schorl–dravite compositions (ie ≥6 Al atoms per formula unit). In terms of X-site occupancy, the tourmalines belong to the alkali group with Na>Ca. Fe/(Fe+Mg) ratios are intermediate between the schorl and dravite end members (**Figure 13**). Further classification is not possible because several diagnostic components (OH^-, O^{2-}, Li, Fe^{2+}/Fe^{3+}) cannot be directly determined by electron microprobe.

There are some systematic differences in tourmaline composition when comparing the tourmalinites with tourmaline-bearing pegmatite or vein samples, although a general degree of overlap between the two groups is

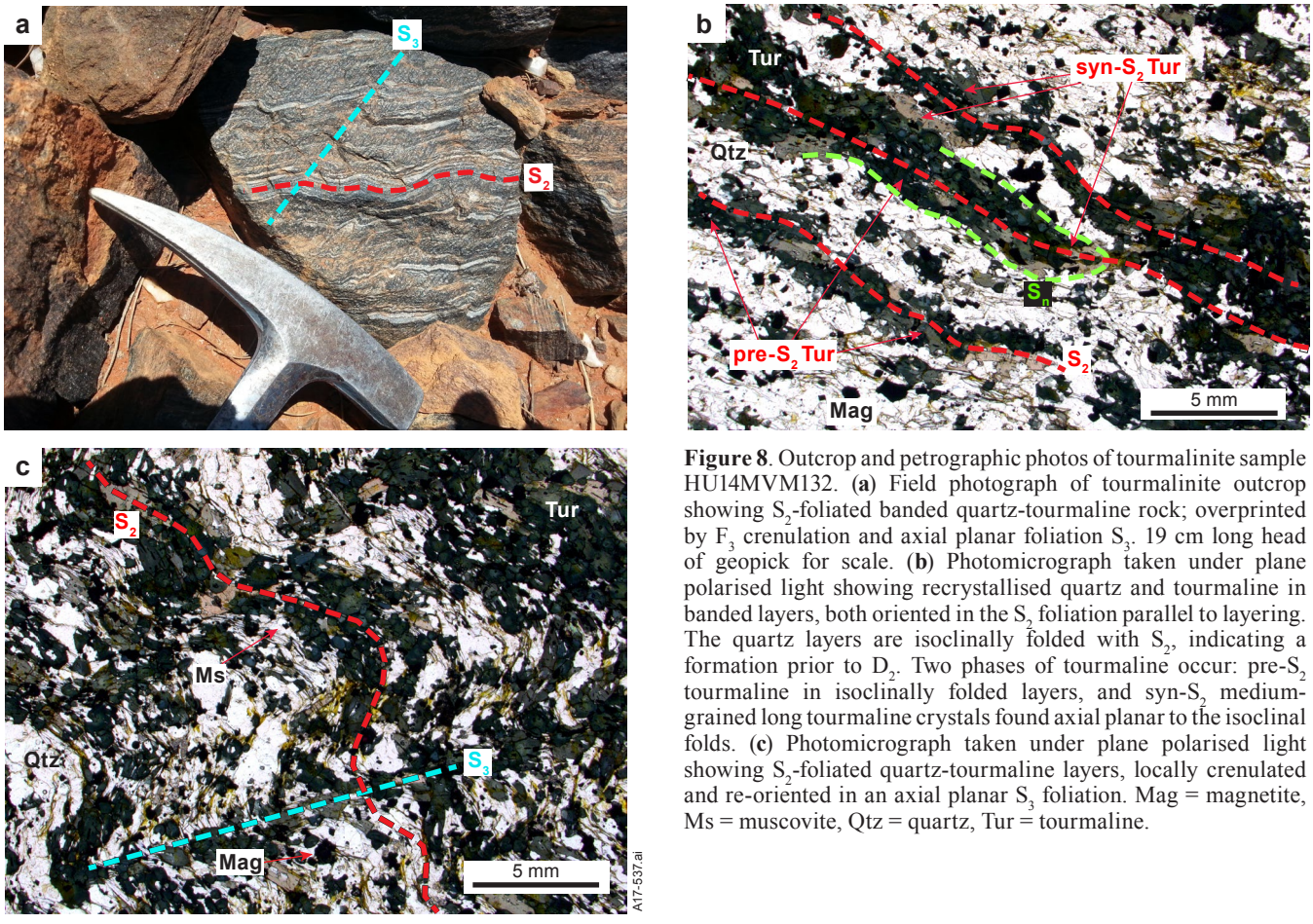

Figure 8. Outcrop and petrographic photos of tourmalinite sample HU14MVM132. (**a**) Field photograph of tourmalinite outcrop showing S_2-foliated banded quartz-tourmaline rock; overprinted by F_3 crenulation and axial planar foliation S_3. 19 cm long head of geopick for scale. (**b**) Photomicrograph taken under plane polarised light showing recrystallised quartz and tourmaline in banded layers, both oriented in the S_2 foliation parallel to layering. The quartz layers are isoclinally folded with S_2, indicating a formation prior to D_2. Two phases of tourmaline occur: pre-S_2 tourmaline in isoclinally folded layers, and syn-S_2 medium-grained long tourmaline crystals found axial planar to the isoclinal folds. (**c**) Photomicrograph taken under plane polarised light showing S_2-foliated quartz-tourmaline layers, locally crenulated and re-oriented in an axial planar S_3 foliation. Mag = magnetite, Ms = muscovite, Qtz = quartz, Tur = tourmaline.

notable. In terms of the Fe/(Fe+Mg) ratio, tourmaline from tourmalinite tends to have more dravitic composition whereas the pegmatite- and vein-related samples trend towards more Fe-rich compositions (**Figure 13**). Fourteen analyses from HU14MVM147 plot as a discrete cluster with a consistent Fe-rich composition (schorl) and variable Na/(Na+Ca) ratios, although five analyses overlap with sample HU14MVM130. Tourmaline from sample HU14MVM133, collected from a tourmaline-bearing quartz vein that cross-cuts an older tourmalinite sequence,

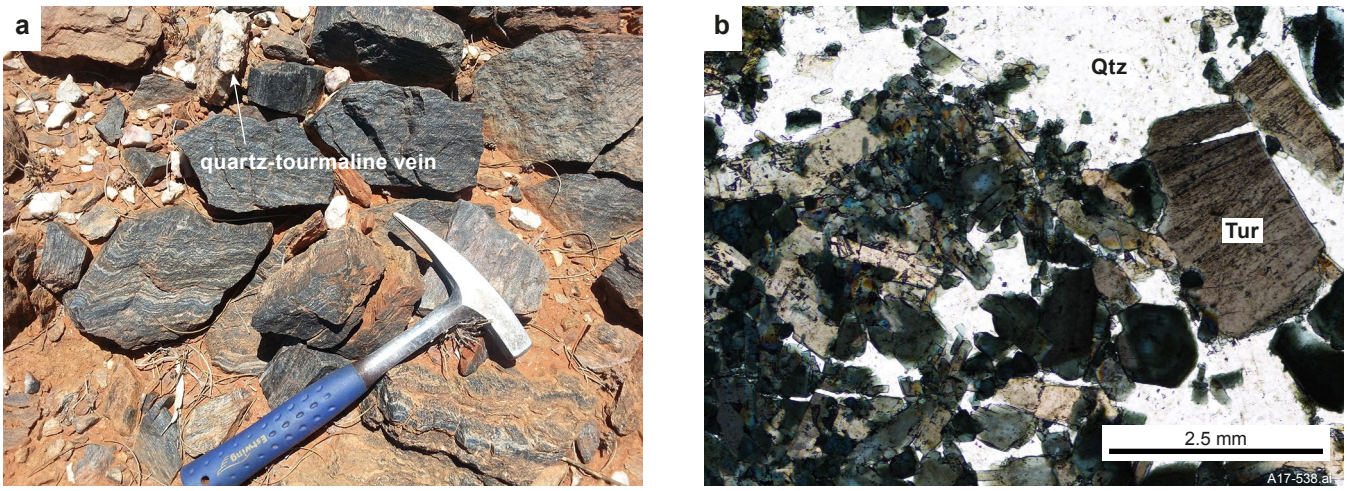

Figure 9. Outcrop and petrographic photos of tourmaline-bearing quartz vein sample HU14MVM133. (**a**) Outcrop photo showing folded and S_2-foliated tourmalinite sub-crop of sample HU14MVM132, cross-cut by the quartz veining sampled as HU14MVM133. 33 cm long geopick for scale. (**b**) Photomicrograph of sample HU14MVM133 taken under plane polarised light showing euhedral and subhedral tourmaline (Tur) ≤1 cm wide (green and grey) hosted within a coarse quartz (Qtz) vein.

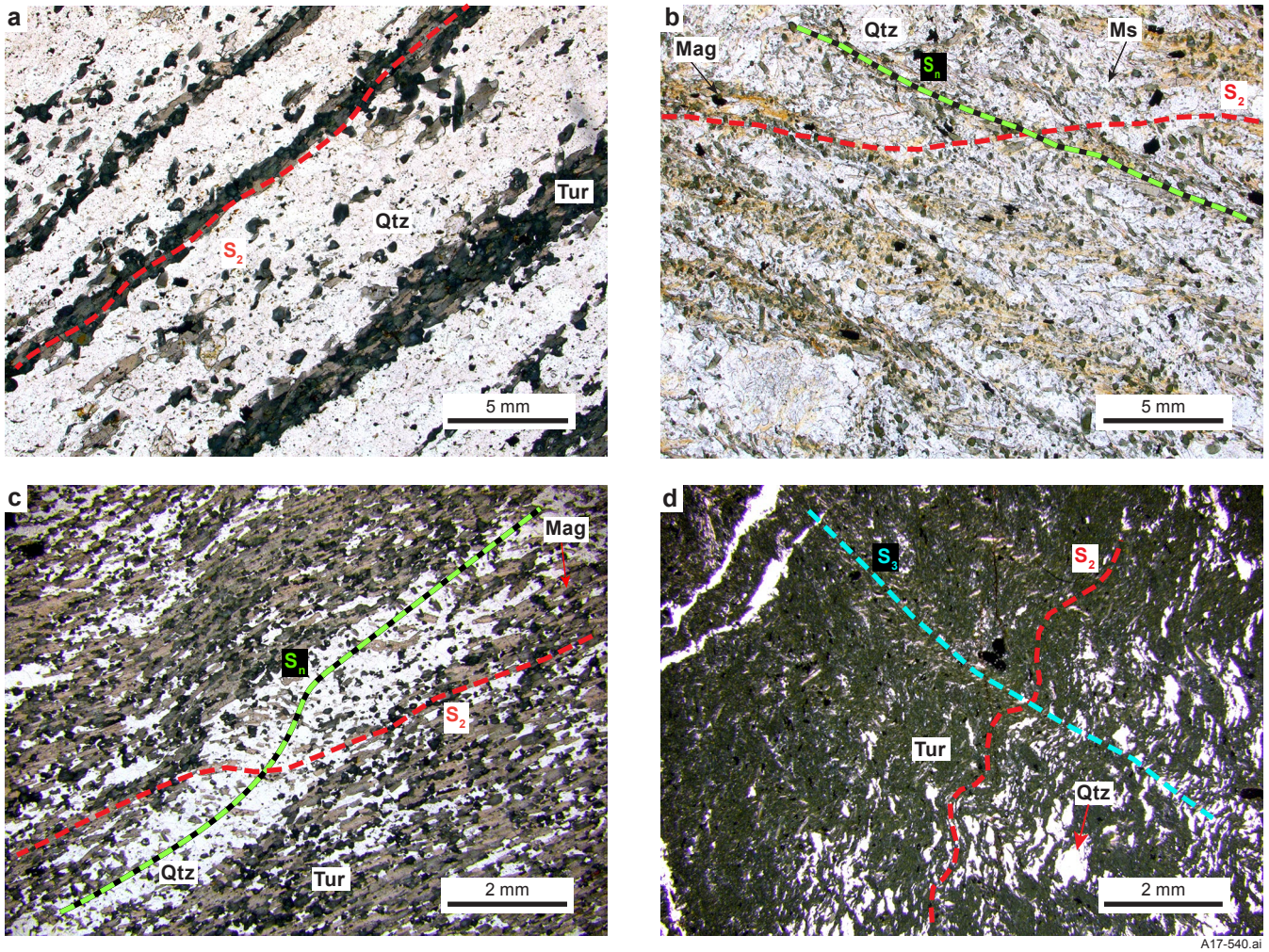

Figure 10. Photomicrographs of historical thin sections from tourmalinites in the east and southeast of the J-Fold structure in the Jervois mineral field. (**a**) 2004088-422MF showing layered and S_2-foliated quartz and tourmaline. (**b**) 2004088-435MF showing a quartz-tourmaline layering (S_n), overprinted by a slightly oblique, weak S_2 foliation. (**c**) 2004088-447MF showing quartz-tourmaline layers, overprinted by a slightly oblique, pervasive S_2 foliation. (**d**) 2004088-448MF showing a large cluster of tourmaline in a S_3-crenulated quartz-tourmaline rock. Red lines indicate crenulation. Mag = magnetite, Ms = muscovite, Qtz = quartz, Tur = tourmaline.

also has more Fe-rich compositions than the tourmalinites; its Na/(Na+Ca) ratio is near 1 (**Figure 13**).

An overview of the main compositional variations are summarised on the Na_2O–MgO–FeO ternary diagram in **Figure 14**. The FeO proportions are high in all samples with subordinate MgO and low Na_2O concentrations (**Figure 14**). **Table 2** shows high FeO concentrations with large variations (9.51–16.42 wt%), whereas TiO_2 (0.21–0.39 wt%) and MnO (≤0.41 wt%) concentrations are uniformly low. No significant chemical zoning was observed from multiple analyses of middle (core) and outer (rims) zones of several tourmaline grains (**Table 2**).

Tourmaline boron isotope composition

The measured boron isotope values ($\delta^{11}B$) in tourmaline from the tourmalinites, tourmaline-bearing pegmatites and tourmaline-bearing quartz veins range in total from -16.9 to -23.1‰ (**Table 3** and **Figure 15**). No within-grain isotopic heterogeneity was detected (**Table 3**). Despite the limited isotopic range of the data set (Δ 6.2‰), there is important inter-sample variation; this is considered significant in terms of the boron source (see **Discussion**).

Tourmaline from tourmalinite sample HU14MVM130 yields an average $\delta^{11}B$ of -22.7 ± 0.6‰ (n = 10) whereas the other tourmalinite sample HU14MVM129 has

Figure 11. Outcrop and petrographic photos of tourmaline-bearing quartz vein sample HU14MVM147 from the Jericho tungsten prospect. 33 cm long geopick for scale. (**a**) View of mineralised costean showing tourmaline-bearing quartz veins cross-cutting altered (hornfelsed) muscovite schist of the Bonya Metamorphics, parallel to the main foliation S_2. (**b**) Close-up of quartz veining containing minor tourmaline and muscovite. (**c**) Photomicrograph taken under plane polarised light showing euhedral dark green to blue tourmaline within quartz. Ms = muscovite, Qtz = quartz, Tur = tourmaline

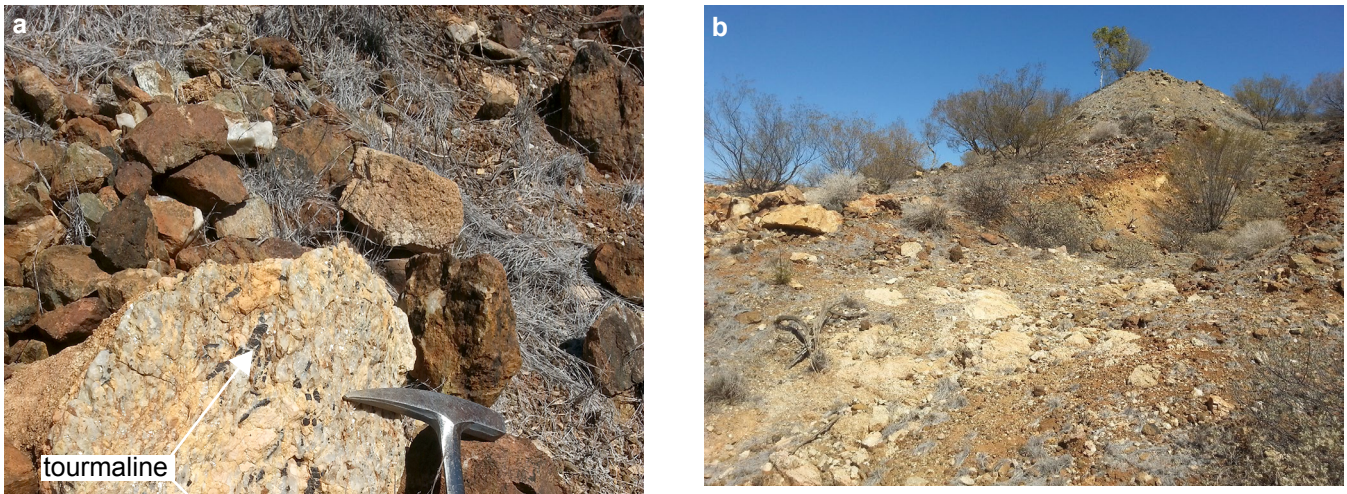

Figure 12. Field location photographs for sample HU15MVM201 from the Samarkand tungsten prospect. (**a**) Samarkand Pegmatite showing coarse-grained black tourmaline. 33 cm long geopick for scale. (**b**) Costean from the prospect containing scheelite and minor malachite mineralisation in skarn surrounding intruding tourmaline-bearing pegmatite. Width of foreground in photo is about 10 m.

slightly higher and more variable $\delta^{11}B$ values (average of -20.5 ± 1.5‰, n = 12). Tourmaline from tourmaline-bearing quartz vein HU14MVM133 yields $\delta^{11}B$ values between the two tourmalinite samples (average of -21.7 ± 1.4‰; n = 8). In contrast, tourmaline from the quartz vein at the Jericho prospect (HU14MVM147) has higher $\delta^{11}B$ values (average of -18.6 ± 1.9‰; n = 21) than the other three samples. However, it must be noted that the difference in isotopic composition between samples may be more apparent than real when considering the variations within each sample, and the analytical uncertainty of the measurements (± 0.8‰). An independent samples t-test was conducted to compare boron isotope compositions of the two most contrasting samples: tourmalinite HU14MVM130 and vein-related tourmaline HU14MVM147. The results of the test indicated no significant difference in the B isotope values between these samples [mean = -22.7‰; 1σ = 0.14 and mean = -18.6‰; 1σ = 1.48 respectively, where t (26) = 14.06, p = 2.06].

In summary, two features of the boron-isotope composition of tourmalines from this study stand out: first, the $\delta^{11}B$ values are very low relative to most known boron isotope reservoirs (see **Discussion**); and second, the analysed samples show remarkably little variation in isotope ratios within and between samples compared to many other tourmaline suites (eg Marschall and Jiang 2011).

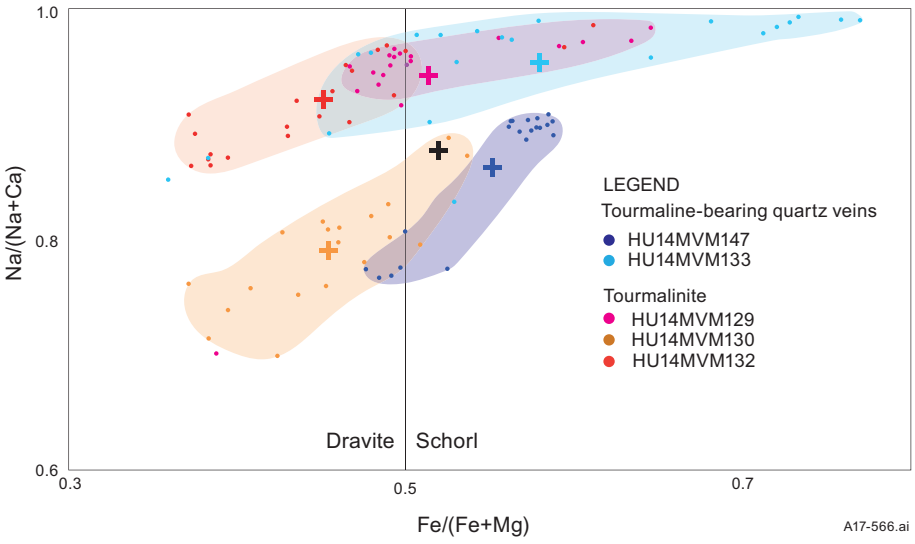

Figure 13. EMP chemical plot of individual analyses of tourmaline from tourmalinite, pegmatite and quartz vein samples. Plot indicates mixed compositions between schorl and dravite sodic sub-group chemistry based on X and Y sites (diagram adapted from Hawthorne and Henry 1999). Although there is some overlap, the tourmalinite samples appear to have a more Mg-rich dravite chemistry compared to the pegmatite- and quartz vein-related tourmaline that has more Fe-rich chemistry. The different coloured + symbols indicate mean values for different samples (black + indicates the mean average for all data). Note that statistical outliers are excluded from the shaded datasets.

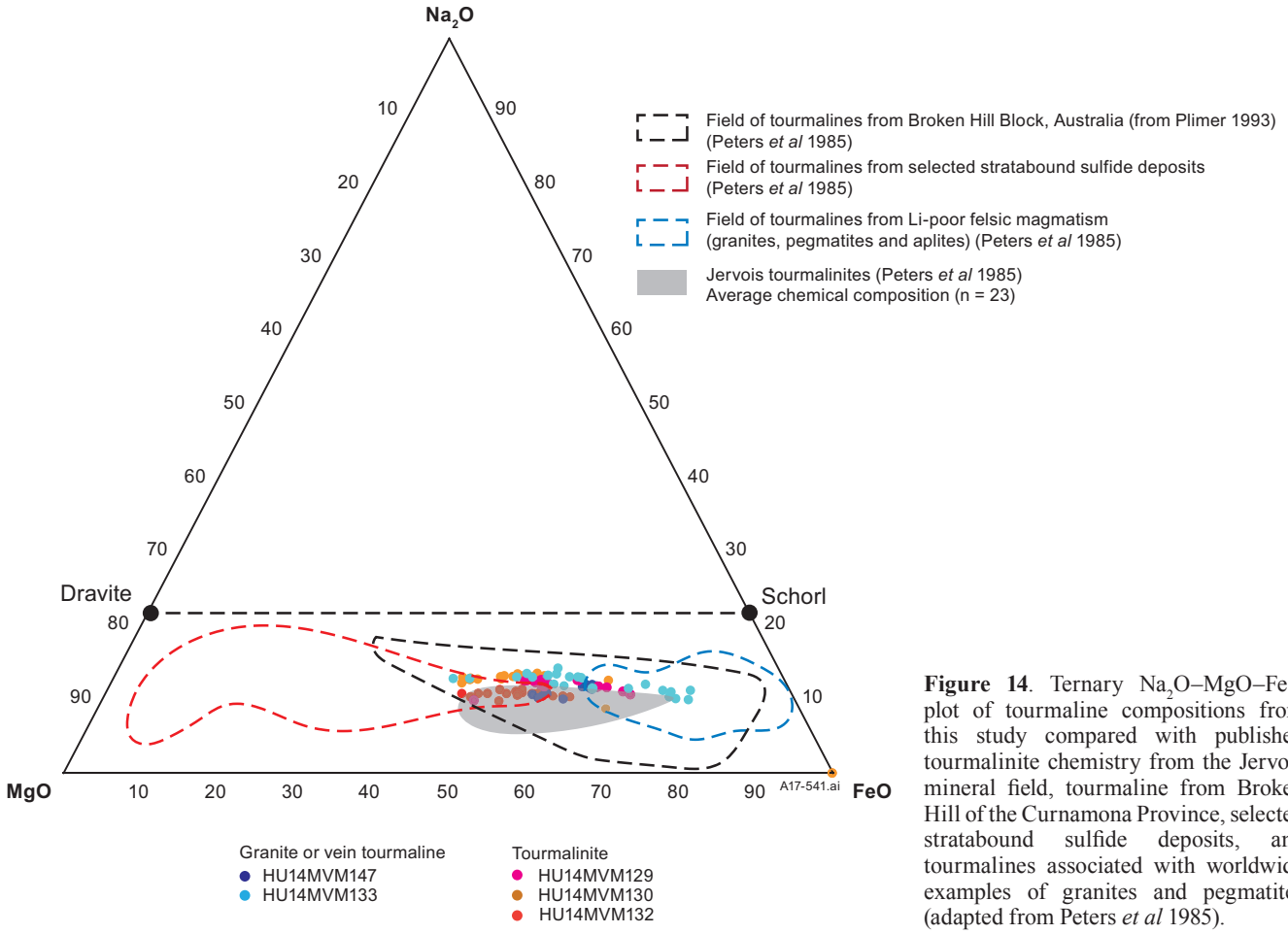

Figure 14. Ternary Na_2O–MgO–FeO plot of tourmaline compositions from this study compared with published tourmalinite chemistry from the Jervois mineral field, tourmaline from Broken Hill of the Curnamona Province, selected stratabound sulfide deposits, and tourmalines associated with worldwide examples of granites and pegmatites (adapted from Peters *et al* 1985).

PbSL DATING

PbSL data for the four tourmaline samples (HU14MVM129, HU14MVM130, HU14MVM147, HU15MVM201) are heterogeneous (**Table 4**). Tourmaline from tourmalinite HU14MVM129 ($^{206}Pb/^{204}Pb$ = 15.9 to 25.1) yields a poorly defined $^{207}Pb/^{204}Pb$ versus $^{206}Pb/^{204}Pb$ array with a nominal Pb–Pb age of 1522 ± 430 Ma (2σ, 5 steps, MSWD[7] = 79; **Figure 16**). If leach step 4 is omitted (it has anomalously high $^{208}Pb/^{204}Pb$ and is a clear outlier), the age shifts to 1737 ± 260 Ma (4 steps, MSWD =19). Leach steps L5 and L6 contain 49% and 40% of the total Pb recovered from this tourmaline respectively. These steps also have the least radiogenic $^{206}Pb/^{204}Pb$, $^{207}Pb/^{204}Pb$ and $^{208}Pb/^{204}Pb$ isotope ratios (eg L6 has $^{206}Pb/^{204}Pb$ = 16.61, $^{207}Pb/^{204}Pb$ = 15.46, $^{208}Pb/^{204}Pb$ = 36.25).

In contrast to HU14MVM129, tourmaline from tourmalinite HU14MVM130 ($^{206}Pb/^{204}Pb$ = 17.5 to 44.2) yielded very young ages. Regression of all 6 leach steps results in a poorly defined

[7] A mean square weighted deviation (MSWD) tests the goodness of fit for isochrons used in isotopic dating. Values >>1 (as seen in this study) indicate a poor model fit.

Sample	Analysis position	SiO_2	Al_2O_3	T_iO_2	FeO	MnO	MgO	Cr_2O_3	CaO	Na_2O	K_2O	B_2O_3	Tourmaline composition
HU14MVM129 Tourmalinite	rim (n = 3)	36.10	31.67	0.36	8.94	0.07	6.74	0.01	1.05	1.94	0.03	10.59	dravite
	core (n = 17)	36.02	31.51	0.40	9.74	0.06	6.31	0.01	0.91	1.93	0.03	10.56	schorl
HU14MVM130 Tourmalinite	rim (n = 3)	36.10	31.67	0.36	8.94	0.07	6.74	0.01	1.05	1.94	0.03	10.59	dravite
	core (n = 17)	36.02	31.51	0.40	9.74	0.06	6.31	0.01	0.91	1.93	0.03	10.56	dravite
HU14MVM132 Tourmalinite	rim (n = 3)	36.10	31.67	0.36	8.94	0.07	6.74	0.01	1.05	1.94	0.03	10.59	dravite
	core (n = 17)	36.02	31.51	0.40	9.74	0.06	6.31	0.01	0.91	1.93	0.03	10.56	schorl
HU14MVM133 Tourmaline-bearing quartz vein	rim (n = 3)	36.10	31.67	0.36	8.94	0.07	6.74	0.01	1.05	1.94	0.03	10.59	schorl
	core (n = 17)	36.02	31.51	0.40	9.74	0.06	6.31	0.01	0.91	1.93	0.03	10.56	schorl
HU14MVM147 Tourmaline-bearing quartz vein	rim (n = 3)	36.10	31.67	0.36	8.94	0.07	6.74	0.01	1.05	1.94	0.03	10.59	dravite
	core (n = 17)	36.02	31.51	0.40	9.74	0.06	6.31	0.01	0.91	1.93	0.03	10.56	schorl

Table 2. Abridged table of EMP average analyses of tourmaline major element compositions. Data reported as oxide weight percent. See **Appendix** for full dataset.

Tourmaline-bearing quartz vein, HU14MVM147		
Point	**δ^{11}B corrected (‰)**	**Internal precision (‰)**
G1-1	-20.5	0.15
G1-2	-20.5	0.11
G1-3	-20.5	0.09
G1-4	-20.5	0.10
G1-5	-19.8	0.10
G1-6	-19.2	0.12
G1-7	-18.9	0.13
G1-8	-18.8	0.10
G1-9	-18.7	0.13
G1-10	-18.6	0.11
G1-11	-18.6	0.10
G1-12	-18.6	0.13
G1-13	-18.5	0.10
G1-14	-17.8	0.15
G1-15	-17.7	0.09
G1-17	-17.6	0.16
G1-18	-17.4	0.12
G1-19	-17.3	0.13
G2-20	-17.1	0.10
G2-21	-17.0	0.13
G1-22	-16.9	0.10
Mean	**-18.6**	
Max	**-16.9**	
Min	**-20.5**	
Tourmaline-bearing quartz vein, HU14MVM133		
Point	**δ^{11}B corrected (‰)**	**Internal precision (‰)**
A1	-20.3	0.11
A2	-22.2	0.09
A3	-20.9	0.09
A4	-21.6	0.12
A5	-21.8	0.11
A6	-21.6	0.13
A7	-22.6	0.11
B8	-22.6	0.11
Mean	**-21.7**	
Max	**-20.3**	
Min	**-22.6**	
Tourmalinite, HU14MVM129		
Point	**δ^{11}B corrected (‰)**	**Internal precision (‰)**
A13	-21.1	0.08
A14	-20.3	0.13
A16	-20.1	0.12
A15	-20.7	0.09
B1	-20.6	0.12
B2	-20.1	0.09
B4	-21.0	0.10
B3	-20.4	0.10
C1	-20.8	0.10
C2	-19.0	0.12
C3	-20.8	0.11
C4	-20.6	0.14
Mean	**-20.5**	
Max	**-19.0**	
Min	**-21.1**	
Tourmalinite, HU14MVM130		
Point	**δ^{11}B corrected (‰)**	**Internal precision (‰)**
A1	-22.8	0.10
A2	-22.4	0.09
A3	-22.5	0.12
B1	-22.8	0.12
B2	-23.1	0.06
B3	-22.2	0.12
B4	-23.0	0.10
B5	-22.1	0.09
C1	-22.6	0.12
C2	-23.1	0.10
Mean	**-22.7**	
Max	**-22.1**	
Min	**-23.1**	

Table 3. SIMS boron isotope data for tourmalines in this study.

$^{207}Pb/^{206}Pb$ age of 1249 ± 270 Ma (MSWD = 358). Removal of two outliers (L1, L4) reduces scatter but does not change the age significantly (1307 ± 160 Ma, MSWD = 54).

Tourmaline from a tourmaline-bearing quartz vein associated with pegmatite (HU14MVM147) yields $^{206}Pb/^{204}Pb$ ratios of 16.6 to 58.1 and produces a $^{207}Pb/^{206}Pb$ isochron age of 1710 ± 42 Ma (n = 8, MSWD = 62). This isochron age calculation includes a data point for an acid-leached K-feldspar with unradiogenic Pb ($^{206}Pb/^{204}Pb$ = 16.01). This K-feldspar produced an individual Pb model age of ca 1.72 Ga (**Table 4**).

Tourmaline from pegmatite HU15MVM201, produced the most radiogenic Pb isotope ratios ($^{206}Pb/^{204}Pb$ = 42.0 to 853), consistent with elevated bulk $^{238}U/^{204}Pb$ (>100). An acid-leached K-feldspar from this pegmatite had considerable radiogenic Pb ($^{206}Pb/^{204}Pb$ = 32.3; **Table 4**). A Pb–Pb isochron age could not be obtained from these data because the Pb isotope ratios do not correlate. Leach steps L2 and L4, which released the most radiogenic Pb measured in this sample ($^{206}Pb/^{204}Pb$ = 853 for L2 and $^{206}Pb/^{204}Pb$ = 416 for L4), have very low $^{207}Pb/^{206}Pb$ (0.0477 ± 0.0001, 0.0619 ± 0.0025), indicating the presence of a young radiogenic component (the radiogenic $^{207}Pb/^{206}Pb$ model age for L2 is 86 ± 5 Ma).

DISCUSSION

Petrological constraints on tourmaline formation

Tourmalinites

The tourmalinites in the Jervois mineral field form traceable, discrete, stratabound layers within the metasedimentary Bonya Metamorphics (**Figure 2**). At the km-scale, the tourmalinite layers, together with other metaexhalites (garnetites, layered iron-rich rocks and apatite-rich rocks) and the rest of the Bonya Metamorphics succession, are folded by a prominent F_3 structure that forms the characteristic, synformal J-Fold geometry (**Figure 2**). In micro-scale, some tourmaline in the tourmalinite samples are re-crystallised and are oriented axial planar to F_3 crenulation (**Figures 6c** and **8c**). This indicates that the tourmalinites formed prior to D_3, an observation consistent with conclusions by Peters *et al* (1985).

The majority of the tourmalinites do not show signs of remobilisation and alteration after D_3; however, there are some exceptions. Locally, post-D_3 tourmaline-bearing quartz veins cross-cut tourmalinites (eg HU14MVM133, **Figure 9a**). In some cases (eg HU14MVM129), randomly oriented magnetite (eg **Figures 5b, c**) and sulfide minerals overprint the S_2 foliation in the tourmalinites, indicating later introduction, or more likely, minor remobilisation of these minerals. These observations are supported by evidence from some mineralised zones in the Jervois mineral field that shows post-D_2, possibly post-D_3 magnetite overprinting pre-existing alteration assemblages (eg magnetite-associated epigenetic copper mineralisation at the Rockface deposit; see Mayes and Bennett 2017; McGloin 2017).

The geometry, structural, and textural characteristics of the layered tourmalinites in the Jervois mineral field indicate a pre- to syn-D_2 timing of formation (eg **Figures 5–10**). The majority of the tourmaline, magnetite and apatite in the tourmalinites are foliated by a pervasive regional S_2

	Sample	Pb (ng)	$^{206}Pb/^{204}Pb$	2 se*	$^{207}Pb/^{204}Pb$	2 se*	$^{208}Pb/^{204}Pb$	2 se*	$^{207}Pb/^{206}Pb$	2 se*
tourmalinite HU14MVM129	129 L1	51	20.128	0.001	15.812	0.001	40.687	0.003	0.78557	0.00007
	129 L2	108	22.699	0.001	16.121	0.001	43.634	0.002	0.71020	0.00001
	129 L2▲		22.667	0.001	16.085	0.001	43.507	0.002	0.7096	0.00001
	129 L3	0.1	21.973	0.001	16.055	0.001	51.906	0.002	0.7308	0.00001
	129 L4	2.0	25.44	0.13	16.249	0.022	66.85	0.49	0.6387	0.0028
	129 L5	805	15.942	0.001	15.398	0.001	35.570	0.002	0.96592	0.00002
	129 L6	655	16.613	0.001	15.461	0.001	36.247	0.002	0.93069	0.00001
tourmalinite HU14MVM130	130 L1	14.4	37.31	0.05	17.055	0.005	64.462	0.068	0.45708	0.00049
	130 L2	52.0	41.813	0.018	17.641	0.003	70.907	0.025	0.42157	0.00015
	130 L2▲		41.817	0.018	17.642	0.003	70.851	0.025	0.4219	0.025
	130 L3	0.4	40.14	2.66	17.53	0.28	69.9	3.1	0.437	0.022
	130 L4	1.1	44.22	0.93	17.76	0.10	67.4	1.0	0.4015	0.0065
	130 L5	63.1	17.519	0.001	15.577	0.001	36.369	0.002	0.88918	0.00002
	130 L6	134	23.470	0.001	16.142	0.001	43.201	0.002	0.68773	0.00001
tourmaline-bearing quartz vein HU14MVM147	147 L1	257	50.173	0.004	19.045	0.003	43.361	0.005	0.37960	0.00001
	147 L2	97	47.687	0.002	18.717	0.001	45.015	0.002	0.39250	0.00000
	147 L2▲		47.663	0.005	18.701	0.002	44.966	0.006	0.39235	0.00001
	147 L3	0.9	51.08	1.357	19.10	0.16	63.4	1.0	0.3742	0.0071
	147 L4	3.9	58.12	0.568	19.74	0.07	117.0	1.1	0.3396	0.0023
	147 L5	41.6	16.65	0.001	15.467	0.001	35.783	0.002	0.92874	0.00001
	147 L6	265	18.75	0.001	15.642	0.001	36.632	0.002	0.83445	0.00001
	147 Kf	503	16.01	0.001	15.422	0.001	35.642	0.002	0.96305	0.00001
tourmaline-bearing pegmatite HU14MVM201	201 L1	29.7	353.5	1.5	38.32	0.10	68.01	0.13	0.10842	0.00017
	201 L2	46.1	853.2	5.0	40.72	0.15	72.77	0.21	0.04773	0.00011
	201 L3	28.8	42.00	0.03	17.887	0.003	44.842	0.008	0.42589	0.00019
	201 L4	1.8	416	29	25.75	0.77	61.7	1.8	0.06193	0.00250
	201 L5	44.2	139.1	0.2	22.349	0.011	56.839	0.029	0.16065	0.00013
	201 Kf	16.8	32.329	0.024	17.401	0.004	41.838	0.008	0.53825	0.00030

	Sample	Pb (ml)	Pb (ng)	$^{206}Pb/^{204}Pb$	2 se*	$^{207}Pb/^{204}Pb$	2 se*	$^{208}Pb/^{204}Pb$	2 se*	$^{204}Pb/^{206}Pb$	2 se*	$^{207}Pb/^{206}Pb$	2 se*	$^{208}Pb/^{206}Pb$	2 se*
feldspars	#147 fs	7.5	503	16.013	0.001	15.422	0.001	35.642	0.002	0.062448	0.000004	0.96305	0.00001	2.22580	0.00004
	#201 fs	0.5	17	32.273	0.005	17.393	0.002	41.821	0.004	0.030986	0.000005	0.53893	0.00002	1.29581	0.00005
	#201 fs	corrected with Pb blanks		32.329	0.024	17.401	0.004	41.838	0.008	0.030932	0.000023	0.53825	0.00030	1.29412	0.00076

Table 4. Pb–Pb step leaching raw values of tourmaline and K-feldspar analysed in this study. Pb contents estimated from Pb signals measured on the MC-ICPMS are minimum estimates. Results corrected for blank (50±20 pg Pb, $^{206}Pb/^{204}Pb$ 17.6±0.2, $^{207}Pb/^{204}Pb$ 15.3±0.1, $^{208}Pb/^{204}Pb$ 37.4±0.2, all errors 2sd) where such a correction was significant

***** internal precision (2 se %) for Pb isotope runs augmented (sometimes considerably) by the blank correction. All Pb-Pb isochron regressions were done with augmented internal 2se errors as listed (but never smaller than 0.06%) and rho=0.9.

▲ Denotes repeat analysis.

foliation that is also present in the Bonya Metamorphics and local meta-igneous rocks (eg Peters *et al* 1985, Weisheit *et al* in review; **Figures 5–10**).

A likely pre-D_2 timing for the formation of tourmalinites can be concluded from samples HU14MVM129 and HU14MVM132. In these samples, tourmaline and quartz are clearly separated into compositional layers (**Figures 5a, 5b, 5b**). This is interpreted to result from dynamic recrystallisation, during either D_n or D_2. In HU14MVM129, tourmaline appears to have grown in two generations.

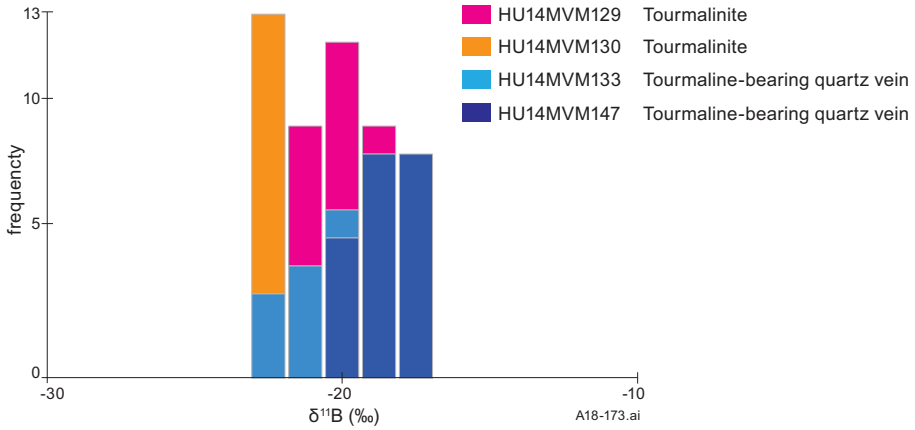

Figure 15. Histogram showing boron isotopic compositions ($\delta^{11}B = {}^{11}B/{}^{10}B$) of tourmaline from this study.

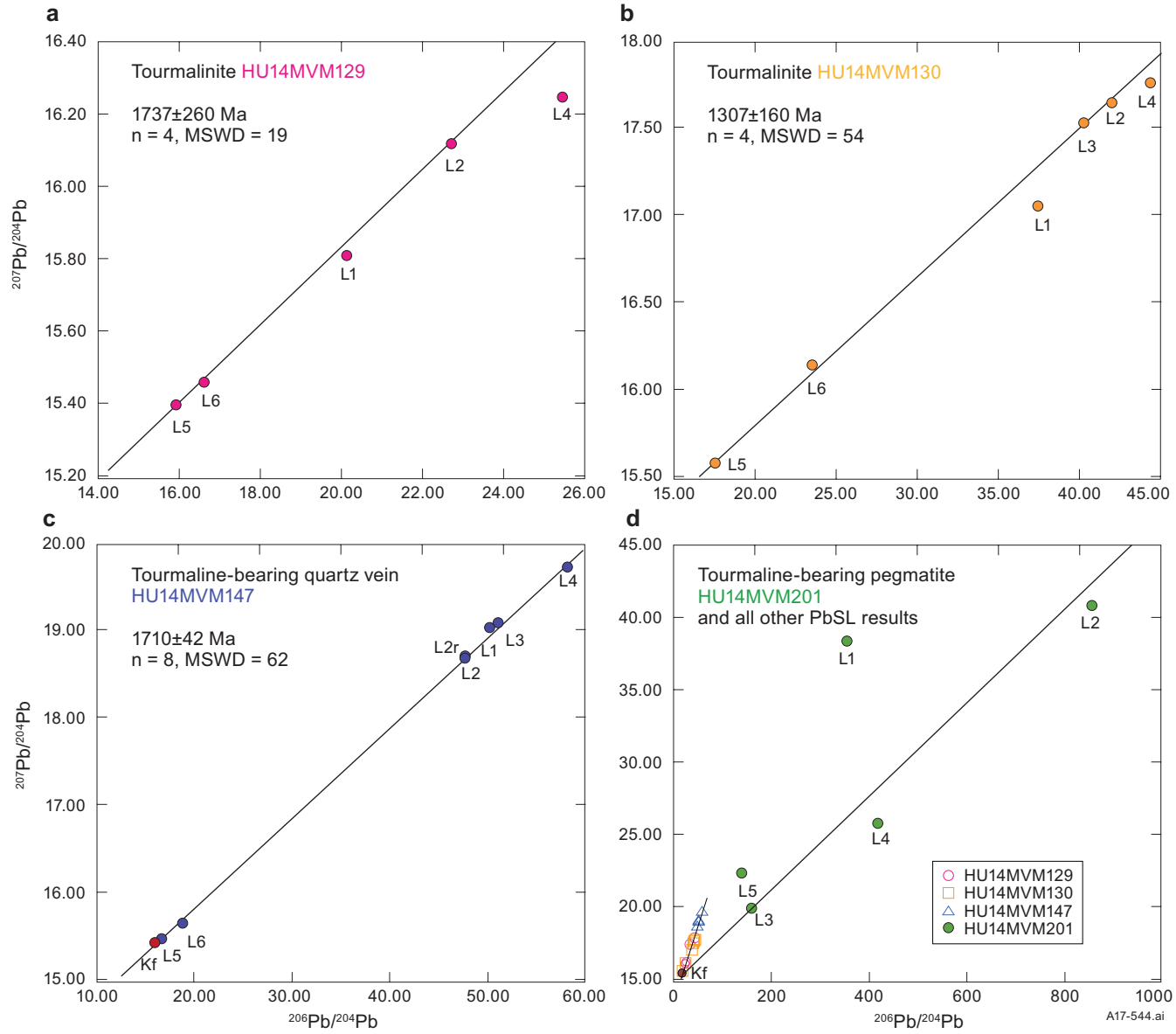

Figure 16. Selected $^{207}Pb/^{206}Pb$ isochron plots derived from tourmaline dating using the PbSL method; errors are not plotted due to the large uncertainties (see Table 4). (**a**) Normal isochron plot for HU14MVM129, with n = 4 (one outlier L4 omitted). (**b**) Normal isochron plot for HU14MVM130, with n = 4 (two outliers (L1 and L6) omitted). (**c**) Inverse isochron plot for HU14MVM147, with n = 8; Kf refers to a K-feldspar sample from the vein that yielded a ca 1.72 Ga Pb model age. (**d**) Normal isochron plot for HU15MVM201 (n = 5) showing no correlation; Kf refers to K-feldspar sampled from this pegmatite. An isochron including PbSL results of all samples except HU15MVM201 indicates a ca 1.70 Ga age.

Older tourmaline is aligned and has a lattice-preferred orientation parallel to the layering. Younger tourmaline overgrows the older fabric and contains inclusions of oriented muscovite, but is also aligned in places, indicating syn- to late-tectonic growth during D_2 (**Figure 5b**). The majority of the tourmaline in HU14MVM129 grew prior to the formation of the S_2 foliation. It is unknown whether the tourmaline formed pre-D_n because isoclinal folding necessary to confirm such timing (Weisheit *et al* in review) is not preserved. The relationship of tourmaline to D_2 is more obvious in sample HU14MVM132. The compositional layering of quartz and an early generation of tourmaline in that sample is folded in isoclinal F_2 folds, indicating pre-D_2 formation. A second generation of aligned tourmaline formed locally in the axial planes of the F_2 folds, and is interpreted as syn-D_2 tourmaline (**Figure 8b**).

Further indication for pre-D_2 tourmaline is found in a porphyroclast in sample HU14MVM129. Tourmaline in this porphyroclast is weakly oriented, forming a slightly oblique internal foliation (S_n or S_2) to the S_2 foliation in the sample's groundmass (**Figure 5c**). This sample is representative of several outcrops of m-thick tourmalinite with porphyroclasts found in the Jervois mineral field. There are two possible interpretations for the origin of these porphyroclasts: they formed from either (1) a concretion of coarser-grained tourmaline that reacted more competently during D_2 deformation; or (2) the pseudomorphic replacement of a former D_n- to D_2-aged porphyroblastic mineral like andalusite, typically found in the interlayered mica schists (Weisheit *et al* in review).

Both interpretations provide a crucial timing constraint for the formation of the tourmalinites. Reno *et al* (2016) demonstrated using petrochronological relationships that cordierite and andalusite porphyroblasts in the mica schists of the Bonya Metamorphics formed during low-*P*, high-*T* metamorphism between and during D_n and D_2. In this case, the metamorphic tourmaline may be pseudomorphic, replacing porphyroblasts with internal foliations that formed after D_n or during peak-*T* metamorphism and D_2. Alternatively, a tourmaline-bearing porphyroclast that formed from a concretion of tourmaline would indicate irregular distribution of B-bearing minerals in the original sedimentary rock prior to the metamorphic growth of tourmaline. In sample HU14MVM129, a similar distribution of accessory zircon, monazite and titanite was found within and outside of the porphyroclast. This may indicate that the porphyroclast originated from a concretion of B-bearing minerals that developed during the formation of the layered matrix. This would likely have occurred during the initial stages of the regional high-thermal gradient metamorphism during D_n.

Our interpretation of tourmalinite paragenesis is generally consistent with the observations outlined by Peters *et al* (1985), who proposed a pre-D_2 (possibly pre-D_n) timing. Our study is also consistent with their observations of some minor syn- to post-D_2 growth of tourmaline in the tourmalinites. Although the host Bonya Metamorphics are folded by F_n folds elsewhere in the area (Weisheit *et al* in review), it cannot be confirmed that layered tourmaline in the tourmalinites experienced D_n. Consequently, no direct evidence of a pre-D_n stratiform origin for the tourmalinites was observed (in contrast to Peters *et al* 1985). This is largely because no indicatory sedimentary structures (original S_0 bedding and structures parallel to bedding planes) are preserved due to pervasive isoclinal folding and transposition during D_2 deformation and upper amphibolite-grade metamorphism (Weisheit *et al* in review). Nonetheless, circumstantial evidence supports a synsedimentary timing (syngenetic to diagenetic) for tourmalinite formation: 1) the layering of bands of tourmaline, apatite and magnetite in the tourmalinites is parallel to the lithological layers in adjacent Bonya Metamorphics rocks, suggesting an original bedding control on the whole succession (ie stratabound); and 2) the spatial association of the tourmalinites in the Jervois mineral field with metaexhalites and stratabound base metal mineralisation implies a genetic link and supports a synsedimentary (possibly originally stratiform) origin for the tourmalinites. Although, a later, post-diagenetic, but pre-D_2 timing of formation of the tourmalinites cannot be completely precluded. Tourmaline-altered igneous rocks of the Baikal Supersuite have been observed in two areas around the Bonya Hills (Weisheit *et al* in review). These rocks are foliated by S_2 indicating that at least some tourmaline alteration was syn- to post-depositional and occurred prior to or during D_2. However, this tourmaline is not hosted in metasedimentary rocks nor does it share the spatial association with mineralisation and other exhalites like the tourmalinites in the Jervois mineral field.

Tourmaline-bearing pegmatites and quartz veins

Tourmaline-bearing pegmatites and tourmaline-bearing quartz veins are found throughout the study area. The majority of the pegmatites are undeformed (ie Samarkand Pegmatite in Shaw *et al* 1984 and Weisheit *et al* in review) and intrude S_2 foliated rocks. Many of these pegmatites and associated quartz veins are commonly located in the hinge zones of large F_3 folds (McGloin and Weisheit in review) and are associated with vein- or skarn-style copper and tungsten mineralisation (**Figure 3, Figure 4j–m**). The sampled tourmaline-bearing pegmatites and veins (HU14MVM147 and HU15MVM201) are undeformed and closely associated with disseminated and veined tungsten and copper mineralisation, typically at contacts with skarn metacarbonate rocks or altered schists of the Bonya Metamorphics (McGloin and Weisheit in review; eg **Figures 4j–m**). Some scheelite has also been reported within pegmatite and veins (Bowen *et al* 1978, Freeman 1986). These relationships have been interpreted to indicate a link between boron-rich felsic magmatism, associated hydrothermal fluids and the epigenetic tungsten-copper mineralisation across the study area (Bowen *et al* 1978, Raith *et al* 2004, McGloin and Weisheit 2015, McGloin and Weisheit *in review*).

Several tourmaline-bearing quartz veins cross-cut S_2-foliated tourmalinites in the Jervois mineral field (eg **Figure 9**); the post-S_2 timing of these veins clearly differentiates them from the tourmalinites. The vein-hosted tourmaline sample HU14MVM133 is associated with trace magnetite and very minor pyrite and chalcopyrite. The sulfides were likely remobilised locally from the host succession during vein formation and possibly may

be related to the regional tungsten-copper mineralising episode.

The relationships between the tourmaline-bearing pegmatites and tourmaline-bearing quartz veins, F_3 folding, and epigenetic mineralisation indicate these tourmaline-bearing rocks formed after D_3. This interpretation is consistent with Peters *et al* (1985) and Raith *et al* (2004) who concluded a post-D_3 timing for most of the vein-style tourmaline.

Absolute timing constraints on tourmaline formation

PbSL dating of tourmaline from tourmalinites and the tourmaline-bearing pegmatites and tourmaline-bearing quartz veins failed to produce readily interpretable and robust geochronological data (**Table 4; Figure 16**). However, assuming that linear and near-linear arrays in uranogenic Pb isochron diagrams represent simple two-component mixtures of common and radiogenic Pb (the basis of secondary Pb–Pb isochron dating; see Faure and Mensing 2005), the PbSL data for 3 of the 4 tourmaline samples yield apparent ages of 1737 ± 260 Ma, 1307 ± 160 Ma and 1710 ± 42 Ma (**Figure 16a–c**).

The fourth analysed sample of tourmaline-bearing pegmatite (HU15MVM201) yielded scattered results and appears to contain impurities or domains that, based on their very low $^{207}Pb/^{206}Pb$, represent addition of radiogenic Pb as young as 86 ± 5 Ma (**Figure 16d**). If such components are also present in the other samples, their effects are more subtle but may explain the observed scatter (and resultant large uncertainties) in all data sets and the unrealistically young apparent tourmaline isochron age (ca 1249 Ma) in one tourmalinite (HU14MVM130). The U–Th–Pb systems in the bulk tourmaline are more complicated than expected based on their lack of compositional zoning and homogeneous $\delta^{11}B$ isotope values. The PbSL method reveals this complexity through its ability to selectively dissolve and release Pb from different mineralogical components and sites within a robust mineral like tourmaline (van Hinsberg *et al* 2011a). It is likely that complex Pb isotope data reflect impurities within the tourmaline itself (eg Dahl and Frei 1998, Kim *et al* 2007, Bassano *et al* 2012).

Despite these limitations, some valid age information may be preserved in the least radiogenic fractions analysed. Leach step L5 (the first of two HF steps) from tourmaline in tourmalinite sample HU14MVM129 released a large amount of Pb (805 ng, equivalent to 49% of all Pb released from this tourmaline fraction); this is interpreted to represent Pb present in the tourmaline itself or in Pb-bearing inclusions (**Table 4**). The latter could be sulfides (minor sulfides were observed in thin section) although these should have been extracted during earlier leach steps. The Pb isotope ratios ($^{206}Pb/^{204}Pb$, $^{207}Pb/^{204}Pb$ and $^{208}Pb/^{204}Pb$) of leach step L5 (**Table 4**) are similar to 1.60 Ga model Pb from the Stacey-Kramers Pb growth curve (Stacey and Kramers 1975), or to ca 1.72 Ga using the Edwards Creek lead isotope model for the Aileron Province (Hussey *et al* 2005). This is consistent with the poorly constrained PbSL age of 1737 ± 260 Ma for this tourmaline (HU14MVM129). Likewise, acid-leached K-feldspar in a pegmatite-related quartz vein (HU14MVM147) has U/Pb and Th/Pb ratios of ~0 and Pb isotope ratios of 16.01, 15.42 and 35.64, which are consistent with a ca 1.72 Ga age using the Edwards Creek Pb model. This in turn is consistent with the tourmaline 1710 ± 42 Ma PbSL age for this sample. These common Pb model ages are interpreted to be minimum ages because both leach step L5 for HU14MVM129 and the Pb isotope values measured in K-feldspar from HU14MVM147 could still contain small amounts of radiogenic Pb.

Direct dating of tourmaline provides minimum, albeit poorly constrained ages; however, other age information helps constrain the relative timing of tourmaline formation. The metasedimentary host sequence for the tourmalinites has a maximum depositional age of 1787 ± 6 Ma, based on SHRIMP U–Pb dating of detrital zircons (Kositcin *et al* 2015). As discussed previously, the layered tourmalinites are interpreted to be stratabound, and possibly stratiform, and therefore part of the Bonya Metamorphics succession (Weisheit *et al* in review).

High-thermal gradient metamorphism, bimodal magmatism and base metal mineralisation are interpreted to have been contemporaneous with the deposition of the sedimentary precursors of the Bonya Metamorphics (Weisheit *et al* in review, McGloin *et al* in prep). Thus, the timing of these processes provides minimum age constraints on the timing of tourmaline formation.

The Attutra Metagabbro (which forms stocks, sills and dykes that intruded precursors to the Bonya Metamorphics as part of the bimodal Baikal Supersuite) yielded an igneous crystallisation U–Pb zircon age of 1786 ± 4 Ma (Claoué-Long and Hoatson 2005). This age is indistinguishable from the age of metamorphic monazite in the Bonya Metamorphics. Monazite included in cordierite porphyroblasts in mica schists yielded a $^{207}Pb/^{206}Pb$ age of 1789 ± 10 Ma and records the initiation of high-thermal gradient metamorphism related to emplacement of the bimodal rocks (Reno *et al* 2016). Furthermore, galena Pb model ages from base metal mineralisation at the Green Parrot and Marshall–Reward deposits are as old as ca 1.79 Ga (Warren *et al* 1995, Hussey *et al* 2005, McGloin *et al* in prep).

Together, these ages are interpreted to record the timing of extensive fluid flow in an interpreted active back-arc basin undergoing rapid evolution, with sediment and base metal deposition, bimodal magmatism, and high-heat flow occurring within a period of a few million years (Weisheit *et al* in review, McGloin *et al* in prep). Tourmalinite (and other exhalite) formation is interpreted to be contemporaneous with these events, pre-dating the main period of regional deformation, D_2.

Dating of monazite within the main regional foliation constrains D_2 to ca 1.76 Ga (Reno *et al* 2016), providing a maximum age for the intrusion of pegmatites and veins undeformed by D_2. LA–ICP–MS U–Pb columbite–tantalite dating of pegmatites (occasionally containing minor tourmaline; part of "undivided pegmatite" in Weisheit *et al* in review) that cross-cut S_2 at the Marshall–Reward deposit yielded inferred magmatic crystallisation ages of 1771 ± 17 Ma, 1744 ± 9 and 1740 ± 11 Ma (McGloin *et al* 2018). Raith *et al* (2004) hypothesised that the timing of tourmaline formation in the Bonya Hills was contemporaneous with epigenetic tungsten-copper

mineralisation related to felsic magmatism. Also, as noted above, in places where tourmaline-bearing pegmatites and quartz veins occur in proximity to F_3 folds, these rocks have been observed to intrude preferably into the hinge zone of the folds, or cross-cut F_3 folding (see McGloin and Weisheit in review). That indicates a post-D_3 timing for most of the tourmaline-bearing pegmatites and quartz veins.

Felsic magmatism observed in the northeastern Aileron Province that post-dates the timing of D_2 and D_3 deformation in the study area, and that is associated with epigenetic mineralisation includes the Marshall Granite and the Samarkand Pegmatite (Weisheit *et al* in review, Beyer *et al* in prep). The Marshall Granite, exposed ~50 km west of the study area, yields a magmatic crystallisation zircon age of 1723 ± 12 Ma (Beyer *et al* in prep). This granite hosts the Molyhil tungsten-molybdenum skarn deposit (**Figure 1**; Huston *et al* 2006c). Direct dating of this deposit using molybdenite produced a Re–Os model age that constrains the age of mineralisation to 1721 ± 8 Ma (Cross 2007, McGloin and Bradey 2017). Molybdenite from the Bonya copper deposit in the Bonya Hills yielded a Re–Os age of 1726 ± 8 Ma (McGloin and Weisheit in review). This molybdenite is hosted within a chalcopyrite-pyrite-bearing quartz vein (with tourmaline alteration) that intrudes the hinge zone of a km-scale F_3 fold (McGloin and Weisheit in review, Weisheit *et al* in review).

Intrusion of tourmaline-bearing granites and veins is interpreted to have ceased by ca 1.70 Ga, which represents the timing of the last felsic intrusions recorded in the study area (Weisheit *et al* in review). A sample of tourmaline-bearing pegmatite (Samarkand Pegmatite) taken from the Samarkand W-Cu prospect yielded a poorly constrained $^{207}Pb/^{206}Pb$ apatite crystallisation age of ca 1.70 Ga (McGloin *et al* 2018), providing an approximate minimum age for epigenetic tungsten mineralisation in the study area (McGloin and Weisheit in review). Earlier dating of pegmatites at both the Samarkand and Jericho prospects are also consistent with these ages: Rb–Sr whole rock ages of 1680 ± 60 Ma and 1680 ± 30 Ma, and Rb–Sr muscovite ages of 1708 Ma and 1695 Ma are reported (Dobos 1978).

THE ORIGIN OF TOURMALINITES, TOURMALINE-BEARING PEGMATITES AND QUARTZ VEINS

Tourmaline genesis

Based on the results presented, the timing and origin of the tourmaline-bearing pegmatites and tourmaline-bearing quartz veins from the Bonya Hills area is relatively straightforward to deduce. The chronologic, petrographic and field relationships indicate a clear association with felsic magmatism and a post-D_3 timing. For the Jervois mineral field, the tourmaline-bearing quartz vein analysed also shares a post-D_2, possibly post-D_3 timing and is likely to be associated with hydrothermal fluid flow related to the same felsic magmatism. The major element composition of the pegmatite- and vein-related tourmaline samples, and their association with epigenetic tungsten and copper mineralisation (McGloin and Weisheit in review), are consistent with a granite-related mineral system.

In general, the pegmatite and vein-related tourmaline trends towards schorl composition (Fe>Mg, Na>Ca), whereas the tourmaline in the tourmalinite plots closer to dravite composition (**Figures 13** and **14**). Tourmaline from pegmatite sample HU15MVM201 was not analysed for major element chemistry but is assumed to have a schorl–foitite composition similar to tourmaline from leucogranite in the Bonya Hills analysed in Raith *et al* (2004). The high iron concentrations in the granite-related tourmaline samples are consistent with magmatic-hydrothermal fluids linked to the pegmatites and veins.

The timing and origin of tourmaline associated with the tourmalinites in the Jervois mineral field is more difficult to determine. As discussed in the previous sections, the formation of tourmaline in the tourmalinites is constrained to before or during D_2, with circumstantial evidence possibly indicating a syn- to post-D_n timing. Therefore, tourmaline in the tourmalinites may have formed via epigenetic, synsedimentary or conversion processes, or through a combination of these processes:

- ***Epigenetic***: precipitation of tourmaline from boron-bearing magmatic-hydrothermal fluids exsolved from felsic intrusions, or metamorphic fluids generated during metamorphism.
- ***Synsedimentary***: precipitation of tourmaline from boron-bearing hydrothermal fluids (ie basin brines, formation fluids, evolved seawater, magmatic emanations) involved in hydrothermal chemical sediment formation on or near a basin floor.
- ***Conversion***: precursor boron-bearing assemblages in basin sediments converted to tourmaline during diagenesis and/or metamorphism.

The following discussion assesses these potential processes for tourmalinite formation, and more specifically, tourmaline formation in potential precursors of these unusual rocks.

Epigenetic tourmalinite formation

The formation of some tourmalinites can occur through epigenetic processes involving hydrothermal fluids. Slack (1996) reports several scenarios where tourmalinites form from hydrothermal fluids by replacement of aluminous rocks after diagenesis. Based on the petrographic and structural observations of the tourmalinites in our study, an epigenetic origin would require that the host rocks were selectively repaced by hydrothermal fluids after basin deposition and diagenesis but before peak-metamorphism and D_2 deformation.

Hydrothermal alteration is likely to have occurred in the study area after deposition of the protoliths to the Bonya Metamorphics and prior to D_2. Local occurrences of S_2-deformed K-feldspar–quartz-altered rocks demonstrate that minor epigenetic alteration took place prior to 1.76 Ga (Weisheit *et al* in review). In two instances, granitic rocks that are interpreted to intrude the Bonya Metamorphics were tourmalinised prior to D_2 (Weisheit *et al* in review). Boron transported in these hydrothermal fluids may have been sourced from felsic magmatism or from leaching of

boron-bearing minerals that survived diagenesis in the host succession.

One potential fluid source for direct precipitation of tourmaline within the tourmalinites are magmatic-hydrothermal fluids exsolved from felsic intrusions of the Baikal Supersuite emplaced between ca 1.79–1.77 Ga (Weisheit *et al* in review). However, the current understanding of regional magmatism appears to preclude a direct magmatic link to tourmalinite formation because primary magmatic tourmaline has only been identified in minor tourmaline-bearing pegmatites that are deformed by D_2 (Weisheit *et al* in review). Additionally, if magmatic-hydrothermal fluid flow did occur between diagenesis and peak-pressure metamorphism, veining and cross-cutting relationships, rather than stratabound layering, might be expected. Moreover, if replacement processes occurred, any potential ingress by magmatic-hydrothermal fluids might be expected to have a porosity or permeability control; this would lead to selective ingress into more permeable sandy sediments (as opposed to mud-rich layers), or at contacts between these different lithologies. Instead, the observed tourmalinisation of both former muds and sands likely indicates complexity in fluid flow patterns and fluid-rock interaction in the tourmalinites, which is commonly interpreted in basin environments (Chapman 1987, Bjorlykke 1997).

Another problem with the involvement of magmatic-hydrothermal fluids in the formation of the studied tourmalinites is the common observation that granite-related quartz-tourmaline rocks commonly share a close spatial association with granitic sills (Slack 1996). The nearest outcropping granite intrusions deformed by D_2 in the Jervois mineral field are located 6 km north of the tourmalinites. Columbite–tantalite-bearing pegmatites with a closer spatial association to the tourmalinites (eg at the Marshall–Reward and Green Parrot deposits) post-date the S_2 foliation fabric and are therefore not related to the formation of the older S_2-deformed tourmalinites (McGloin *et al* 2017; McGloin *et al* 2018, McGloin and Weisheit in review). Additionally, tourmalinites observed in the Jervois mineral field are spatially associated, and interpreted to be genetically linked, with lead and zinc mineralisation, whereas granite-related tourmalinites in other parts of the world are not typically associated with large concentrations of these metals (Slack 1996).

Fluids generated during metamorphism might also be involved in an epigenetic process that formed the tourmalinites. Metamorphic fluids are produced by the devolatilisation of hydrous minerals like mica, chlorite and amphibole (eg for chlorite: temperatures of 400–550°C and pressures of ~0.3 GPa; Phillips and Powell 2010). Tourmaline in the studied tourmalinites formed before or early during peak metamorphism when conditions reached upper amphibolite facies in the study area (eg Reno *et al* 2017, Weisheit *et al* in review). Typical metamorphic fluids are aqueous-carbonic in composition with low salinities and neutral pH (and thus very effective at mobilising gold; eg Tomkins 2013). Although tourmaline can form from metamorphic fluids (eg in orogenic gold deposits; Lambert-Smith *et al* 2016), these fluids typically lack the salinity and ligands (such as Cl^-; eg Liu and McPhail 2005, Hammerli *et al* 2015) required to mobilise large amounts of Cu, Pb and Zn. A metamorphogenic origin for the tourmalinites cannot be completely precluded; however, the spatial association of tourmalinites with other metaexhalites in the study area and with stratabound base metal mineralisation argues against tourmalinite formation from metamorphic fluids.

Synsedimentary tourmalinite formation

Many worldwide examples of tourmalinites are closely associated with metamorphosed exhalative deposits and chemical sediments (eg Spry *et al* 2000). The protoliths are generally considered to originate through syngenetic or diagenetic hydrothermal processes (exhalation or replacement) on subaqueous basin floors prior to regional metamorphism (Slack *et al* 1984, Plimer 1988, Slack *et al* 1989, Palmer and Slack 1989, Slack 1996, Spry *et al* 2000). These tourmalinites therefore represent fossil zones of basin floor hydrothermal activity where boron-rich fluids with moderate temperatures (200–400°C) and near-neutral pH (6–8) react with permeable aluminous sediments (Spry *et al* 2000). Support for these processes comes from textural evidence of stratabound and compositionally layered tourmaline interpreted as relict bedding. Further support derives from mineralogical and geochemical evidence indicating mixing of hydrothermal (eg B, Fe) and detrital clastic (Al, Ti) elements (Spry *et al* 2000). Subaqueous boron-rich mud volcanoes observed in present-day basins may represent a present day analogue to some ancient tourmalinites (Slack *et al* 1998). The boron found in tourmalinites is considered to be sourced from terrestrial evaporites and clastic sedimentary rocks and sediments in host basins. Boron is leached from the host stratigraphy by circulating hydrothermal fluids that then transport boron to the site of deposition where boron-bearing exhalites or replacement deposits are formed (Spry *et al* 2000).

Problematically, vent fluids do not transport aluminium efficiently (Feely *et al* 1994); aluminium has low solubility in hydrothermal fluids typically associated with exhalites and seafloor-hosted mineralisation (ie low to moderate temperature 200–400°C fluids with moderate pH; Slack 2002). These fluids have high Fe/Al ratios, whereas tourmalinites have low Fe/Al ratios (Spry *et al* 2000). Diagenetic or replacement models in this setting therefore favour the replacement of permeable aluminous sediments by boron-rich hydrothermal fluids beneath subaqueous basin floors because only boron (and not aluminium) is required to be introduced to unconsolidated aluminium-bearing sediments (Spry *et al* 2000, Slack 2002). Exhalative models account for this by inferring that boron is concentrated when hydrothermal fluids vent onto a basin floor (Spry 1990, Slack 2002). The boron-rich exhalative fluids require a bonding process to form hydrothermal chemical sediments (and concentrate boron-rich minerals). In a brine pool or anoxic water column, aluminous sediments could be transformed into tourmalinites so long as detrital clay, feldspar and chlorite can be replaced on or near the seafloor by mixing with boron-rich hydrothermal fluids (Slack 2002).

The petrology and geological setting of tourmalinites in the Jervois mineral field are consistent with formation through a synsedimentary process. Variations in the

texture and mineralogy of primary and accessory phases in the tourmalinites are consistent with interlayered sandy (quartz-rich) and muddy (mica- and chlorite-rich) protoliths (eg **Figures 5, 8**). Abundant zircon and titanite have been identified within the matrix of these rocks, suggesting they contain a detrital sedimentary component similar to the studied unaltered metasedimentary rocks in the succession (see Kositcin *et al* 2015, Weisheit *et al* in review).

Chronological evidence from rocks in the Jervois mineral field supports a setting suitable for basin floor hydrothermal activity and chemical sediment formation. The ca 1.79 Ga galena Pb model ages for base metal mineralisation (Warren *et al* 1995, Hussey *et al* 2005, McGloin *et al* in prep) are agreeable and contemporaneous with age constraints on the timing of high-temperature metamorphism (Reno *et al* 2016), the intrusion of the Attutra Metagabbro (Claoué-Long and Hoatson 2005), and active sedimentation (Kositcin *et al* 2015, Reno *et al* 2017, Weisheit *et al* in review). The consistent stratabound and shared stratigraphic geometry of the tourmalinites and other metaexhalites (eg garnetites, layered iron oxide rocks) in the Jervois mineral field and their spatial association with a ~500 m-wide base metal mineralised sequence enriched in Fe, Mn, B and P (eg Ypma *et al* 1984, Mackie 1984, Peters *et al* 1985, Whiting 1986, Spry *et al* 2009, Bennett *et al* 2017, McGloin *et al* in prep, this study) support a synsedimentary origin for all of these rocks. These constraints suggest a basin setting whereby active sedimentation occurred along with hydrothermal activity and base metal mineralisation, with heat from shallow intrusive magmatism allowing hot fluids to circulate into the basin pile (McGloin *et al* in prep).

The notable association between the tourmalinites and small, lenticular-layered quartz–magnetite (eg **Figure 4b**) and quartz–hematite rocks (interpreted as banded iron formations [BIF]; Ypma 1985) is also important. The term BIF can imply a very specific genesis; however, no genetic connotation was made for these rocks in the Jervois mineral field (Ypma 1985). Superior-type BIF form from iron-rich waters that precipitate iron oxides as they upwell from deep suboxic basins into shallow, oxidised shelf environments (Bekker *et al* 2010). In contrast, Algoma-type BIF form when hot hydrothermal fluids cool and vent onto subaqueous basin floors depositing chemical sediments (exhalites) as banded iron layers (Spry *et al* 2000, Stevens 2015). The iron-bearing rock assemblages in the Jervois mineral field (and the magnetite-bearing nature of the tourmalinites), combined with the overall interpreted geological setting of the palaeobasin, is more consistent with a hydrothermal exhalative origin for the banded iron layers (Algoma-type), which form in a similar process to most worldwide examples of tourmalinites (Spry *et al* 2000).

Abundant accessory magnetite and apatite in the tourmalinite samples indicate an iron- and phosphorous-rich protolith; this is uncommon in typical basin sediments. Similar enrichment in Fe and P in basin successions elsewhere have been linked to exhalative and replacement processes forming precursor B-Fe-P-rich chemical sediments (Slack *et al* 1993, Spry *et al* 2000, Raveggi *et al* 2015). Mn- and Zn-enrichment is also commonly observed in tourmalinites from those examples; however, these metals are not enriched in the tourmalinites in the Jervois mineral field. Notably, however, Mn- and Zn-rich minerals are commonplace in the spatially associated mineralisation (**Figure 4c–d**) and other alteration in the Jervois mineral field (Peters *et al* 1985, Bennett *et al* 2017, McGloin *et al* in prep). This suggests that similar hydrothermal processes operated in the Jervois mineral field at the time of tourmalinite formation.

A synsedimentary origin for the tourmalinites in the Jervois mineral field is also supported by the presence of spatially associated garnetites (**Figure 4a**). Stratabound garnetites are commonly considered the metamorphosed product of exhalative hydrothermal activity (Slack 2002, Heimann *et al* 2009). In the Jervois mineral field, massive garnet layers up to tens of metres in thickness and hundreds of metres in length commonly occur with minor quartz and magnetite (Ypma 1985, Peters *et al* 1985, Smith *et al* 2016). Garnet compositions are predominantly andradite (Ca-Fe-rich, Al-poor), although transitions to almandine (Fe-rich), spessartine (Mn-rich) and grossular (Ca-rich) varieties occur (Smith *et al* 2016, McGloin *et al* in prep). The Fe-rich and Al-poor nature of this andradite suggests an unusual protolith composition.

In order to form Fe-Mn-rich, Al-poor sediments in the Jervois mineral field, aluminous sediments were either replaced (and aluminium removed), or the original precipitates that formed these Fe–Mn hydrothermal chemical sediments lacked aluminium. As discussed for the tourmalinites, because aluminium is insoluble, ingress of hydrothermal fluids would likely prevent the leaching of aluminium from diagenetic sediments. Furthermore, detrital sediments commonly contain aluminous minerals such as clay, chlorite and feldspar; however, there is no mineralogical or chemical evidence for the prior existence of these minerals in these garnetites (eg abundant mica or sericite), likely precluding such a replacement origin. Unlike the tourmalinites, it can be inferred that the protoliths to the garnetites were probably Fe-rich chemical precipitates lacking detritus. This suggests some variation in the chemistry and composition of different hydrothermal chemical sediments generated in the study area.

The characteristics of the fluid and the fluid/rock ratios involved in tourmalinite formation in the Jervois mineral field can be inferred based on tourmaline chemistry. All analysed tourmalines form a solid solution between the Mg-rich (dravite) and more dominantly Fe-rich (schorl) endmembers. This indicates primary Fe>Mg-compositions in the hydrothermal fluids carrying boron and/or in the host rocks (eg Slack 2002). Because of the absence of chemical zonation in the tourmalines, we interpret their bulk chemistry to reflect primary conditions rather than metamorphic or hydrothermal overprints. Under high fluid/rock ratio conditions, tourmaline composition is controlled mainly by the chemistry of the hydrothermal fluids, whereas in low fluid/rock settings, the bulk composition of the host stratigraphy controls the tourmaline chemistry (Spry *et al* 2000 and references therein). In the proposed synsedimentary model, boron-bearing fluids probably migrated through considerable layers of sediments and underlying rocks and therefore had low initial fluid/rock ratios. Consequently, tourmaline chemistry would be controlled mainly by the bulk composition of the basin sediments (McGloin *et al* in prep).

Iron-rich tourmalinites such as those in the Jervois mineral field are unusual compared to magnesium-rich tourmalinites, which are more commonly associated with stratabound base metals deposits (Peters *et al* 1985). Nonetheless, some VMS and BHT deposits are associated with Fe-rich tourmaline (eg Kidd Creek, Broken Hill; Spry *et al* 2000, Slack 2002). Mg-rich tourmaline in tourmalinites associated with stratabound mineral deposits that are not greatly affected by metamorphism (Slack 1996), are thought to result from entrainment of seawater or marine evaporite brines in those hydrothermal systems (Slack *et al* 2000). The Fe-dominant composition of some tourmalinites probably indicates that hot hydrothermal fluids leached boron from an iron-rich substrate. These fluids then mixed with cold Mg-rich seawater that caused precipitation of boron-bearing minerals at or near the basin floor.

The presence of relatively Fe-rich tourmaline in the Jervois mineral field, together with garnetites (eg **Figure 4a**) including andradite-bearing varieties (Smith *et al* 2016), plus layered magnetite– and hematite–quartz rocks (eg **Figure 4b**), suggest an iron-rich palaeobasin. Circulating hydrothermal fluids likely leached iron from igneous and/or immature clastic sedimentary rocks (as discussed in Slack and Stevens 1994, Spry *et al* 2000, Huston *et al* 2006d, Stevens 2015). Possible Fe-bearing reservoirs include nearby mafic igneous intrusions (like the Attutra Metagabbro in the study area), or a predominantly Fe-rich host succession (ie volcanic rocks or iron-rich clastic detritus). Furthermore, sustained geothermal heat from shallow intrusions (ie the Baikal Supersuite in the study area) may limit the influx of entrained Mg-rich seawater, thus maintaining a relatively high iron content for hydrothermal fluids in the basin (Palmer and Slack 1989, Slack 2002, Stevens 2015).

Tourmaline formation by conversion

Under favourable conditions, boron-rich hydrothermal fluids can precipitate boron-bearing minerals at or below subaqueous basin floors (Palmer and Slack 1989, Slack 1996, Spry *et al* 2000). However, the paragenetic timing of tourmaline formation relative to other possible boron-bearing precursor minerals remains uncertain in tourmalinites (Slack *et al* 1984, Palmer and Slack 1989, Slack *et al* 1989, Spry *et al* 2000, Marschall and Jiang 2011). Besides tourmaline, other boron-bearing minerals (eg clay, carbonate, borate) remain plausible precipitates such that tourmaline may form by conversion of other boron-bearing minerals much later than the deposition of the host hydrothermal chemical sediment. Conversion mechanisms for tourmaline formation in the tourmalinites are considered below.

The boron budget and B-isotopic composition of basin sediments (from boron-bearing clays and other boron-bearing minerals) are susceptible to changes due to secondary hydrothermal processes (such as diagenesis, alteration and metamorphism) until boron becomes fixed in robust minerals like tourmaline.

Evidence from experimental work and from observation of modern-day hydrothermal systems on basin floors helps to constrain the genesis of tourmaline in the tourmalinites from the Jervois mineral field. Experimental evidence from mixing of hot, boron-rich hydrothermal fluids with hornblende and feldspar supports primary tourmaline precipitation (Morgan and London 1989), whereas interaction of these fluids with other minerals like chlorite can also form tourmaline by conversion (Fuchs and Lagache 1994). However, the relevance of these experiments to hydrothermal processes operating in natural basins is poorly constrained because these experiments were undertaken at much higher temperatures (400–700°C) than those considered relevant for the formation of boron-rich minerals in active seafloor systems (200–400°C; Spry *et al* 2000).

Evidence from modern-day seafloor hydrothermal systems suggests that, in some cases, tourmaline does not precipitate directly at vent sites. Palmer (1991) reports tourmaline at hydrothermal vent sites associated with clastic sediments and marine evaporites. However, no tourmaline was reported in non-marine evaporite or sediment-starved ocean ridge settings, and only rarely has tourmaline been reported in back-arc, sediment-starved settings (Palmer 1991). Assuming that fine-grained tourmaline precipitates have not gone unrecognised in these vent sites (eg Slack 1982, Palmer 1991), the absence of tourmaline appears in most cases to be linked to low concentrations of boron in vent fluids, largely because of a lack of available boron in seawater or in the host succession. One exception are terrestrial evaporite settings where high boron concentrations were measured in vent fluids although no tourmaline precipitates were reported (Palmer 1991). The lack of tourmaline in this case was attributed to relatively high pH conditions in the hydrothermal fluids that may have limited tourmaline precipitation (Slack *et al* 1988, Palmer 1991). In such cases, a non-crystalline boron-rich precursor phase may form instead of tourmaline (Slack *et al* 1984, Palmer 1991).

In a study of boron-rich mud volcanoes in the Black Sea, Slack *et al* (1998) report that borate minerals, rather than tourmaline, are the major boron-bearing precipitate from boron-rich hydrothermal fluids that vent near the basin floor. Tourmaline is not abundant and is reported to occur only as minor relict grains in erupted muds (Shnyukov *et al* 1971). Slack *et al* (1998) suggested that tourmaline precipitation was limited because of the low temperature <100°C, alkaline pH, and oxidising nature of the hydrothermal fluids involved. They suggested that, in theory, if hotter, acidic boron-rich hydrothermal fluids were exhaled into chemically reducing bottom waters then tourmaline would also precipitate.

The uncertainty about tourmaline precipitation and paragenesis relative to other boron-rich minerals in modern-day hydrothermal basin systems highlights the need to consider several possible scenarios when interpreting the boron isotope and major element geochemistry of tourmaline from tourmalinites in this study. Although we strongly favour a synsedimentary process for tourmalinite formation overall whereby boron-rich sediments formed on a basin floor by hydrothermal fluids, we cannot constrain the precise timing of tourmaline formation prior to D_2. Tourmaline may have been directly precipitated from hydrothermal fluids at the basin floor; alternatively, it may

have formed later by replacement of boron-bearing clay or other silicate minerals during diagenesis or metamorphism. An upper limit for tourmaline formation in the tourmalinites is likely constrained by higher temperature (>300°C) metamorphism when any remaining B-rich precursor mineral assemblages would likely have converted to stable tourmaline-bearing assemblages.

Boron sources

The boron isotope variations in tourmaline from the Jervois mineral field and the Bonya Hills area (**Table 3** and **Figure 15**) may be explained by different primary boron reservoirs or combinations of primary reservoirs and fractionation effects related to secondary processes. All the tourmaline samples collected in this study are characterised by isotopically low boron values compared to most boron reservoirs (**Figure 17**). Many of the primary boron sources can be precluded by the low $\delta^{11}B$ values: eg mantle, mafic crust, marine water and marine-influenced sediments, as well as most typical continental metasedimentary rocks and granites. Only two primary boron reservoirs are consistent with the range of data in **Table 3** and **Figure 15**: (i) borate leached from non-marine (terrestrial) evaporites, and (ii) boron sourced from highly-evolved felsic magmas (**Figure 17**).

Any geological process involving hydrothermal fluids can potentially remove or add boron from one boron reservoir to another thereby mixing and potentially also fractionating boron isotopes. For this reason, secondary processes involving interactions between solid and fluid boron reservoirs need to be considered to explain lower $\delta^{11}B$ values other than that of the primary boron reservoirs. These processes include hydrothermal fluid flow, the entrainment of seawater, diagenesis, and metamorphism. These secondary processes affect boron isotope fractionation differently depending on a number of factors: the amount of boron concentrated in a reservoir or in the host mineral (eg tourmaline, boron-bearing silicate, borate); the host mineral's textural relationship with other minerals; and both temperature and equilibration reactions between precipitating minerals and hydrothermal fluids. As such, provided that the initial sources of boron contained relatively low $\delta^{11}B$ values (eg $\leq$ -10‰), it is plausible that secondary processes might further lower $\delta^{11}B$ values to the low levels observed in tourmaline in **Table 3** and **Figures 15** and **17.**

The following discussion assesses the different potential primary sources and/or secondary processes that may explain the tourmaline boron isotope data collected for tourmalinites and tourmaline-bearing veins/pegmatites from the study area.

Potential primary boron sources

Granites and related magmatic-hydrothermal fluids

The tourmaline $\delta^{11}B$ data for tourmaline-bearing veins from our study (**Table 3** and **Figure 15**) plot towards the lower end of the range for worldwide boron isotope data. It overlaps the ranges for granite-related veins and is slightly lower than the average $\delta^{11}B$ value for S-type granites (**Figure 17**). The majority of boron isotope data from granites, pegmatites and related hydrothermal veins lie between -22 and -5‰ (Jiang and Palmer 1998, Slack and Trumbull 2011, Trumbull and Slack 2018). Exceptionally low $\delta^{11}B$ values for granite-related tourmaline (as low as -29.9‰) have been reported (Jiang and Palmer 1998), but these rare cases are interpreted to result from contamination of felsic melts by low $\delta^{11}B$-bearing country rocks (eg tourmalinites, terrestrial borate; Slack *et al* 1993, Jiang and Palmer 1998).

Felsic igneous activity was widespread in the study area before, during, and after D_2 (Weisheit *et al* in review). Secondary tourmaline in the tourmalinite samples indicate that epigenetic fluid flow occurred from at least ca 1.76 Ga with some tourmaline growing syn- to late-D_2 (**Figure 5**) and during D_3 (**Figure 6**). Given that the tourmaline-bearing Samarkand Pegmatite formed post-D_3, and that other unnamed tourmaline-bearing dykes and veins in the study area are deformed by D_2, there were clearly prolonged episodes of magmatic-hydrothermal activity that could have provided boron.

A compilation of boron isotope data from magmatic tourmaline and volcanic glass indicates that S-type granites and their volcanic equivalents have considerably lower $\delta^{11}B$ values than those with I-type compositions (Trumbull and Slack 2018, **Figure 17**). S-type granites and related volcanics show an average $\delta^{11}B$ value of -11‰ (1σ = 4‰) whereas the I-type association has an average $\delta^{11}B$ value of -2‰ (1σ = 5‰; Trumbull and Slack 2018). The comparatively low $\delta^{11}B$ values for S-type granites was attributed in that study to clays and micas in the magma source that naturally sequester ^{10}B preferentially to ^{11}B. Furthermore, ^{11}B is concentrated in fluids derived from prograde metamorphism of micaceous metasedimentary rocks prior to partial melting, which can further lower the $\delta^{11}B$ values of a micaceous source rock.

The low tourmaline $\delta^{11}B$ values in our samples (**Figure 17**) may indicate a source from S-type magmatism; especially favourable would be highly fractionated magmas that underwent fluid exsolution (Trumbull and Slack 2018). The effect of fluid loss is to deplete the residual melt in ^{11}B preferentially, thus lowering its $\delta^{11}B$ value (Smith and Yardley 1996, Jiang and Palmer 1998). Because of the high temperatures relevant to felsic magmatism (eg >450°C), this process is unlikely to alter the $\delta^{11}B$ values by greater than 4–5‰ (Palmer and Slack 1989). The magmatic scenario is plausible for the low $\delta^{11}B$ values of tourmaline from pegmatites and quartz veins in the study area where highly-fractionated granites may have undergone an episode of fluid exsolution to produce these pegmatites and veins. Tourmaline sample HU14MVM147 is associated with strongly peraluminous leucogranite and pegmatite phases of the Samarkand Pegmatite. This supports a felsic magmatic source for the analysed boron isotopes in that tourmaline sample. The association with the post-D_3 Samarkand Pegmatite is consistent with the evolved waning stages of felsic magmatism.

Therefore, from the boron isotope data and the field evidence for tourmaline-bearing pegmatites and quartz veins intimately associated with granite intrusions, an S-type granite origin is proposed both for the tourmaline hosted in pegmatites and veins associated with epigenetic copper and tungsten mineralisation in the Bonya Hills area

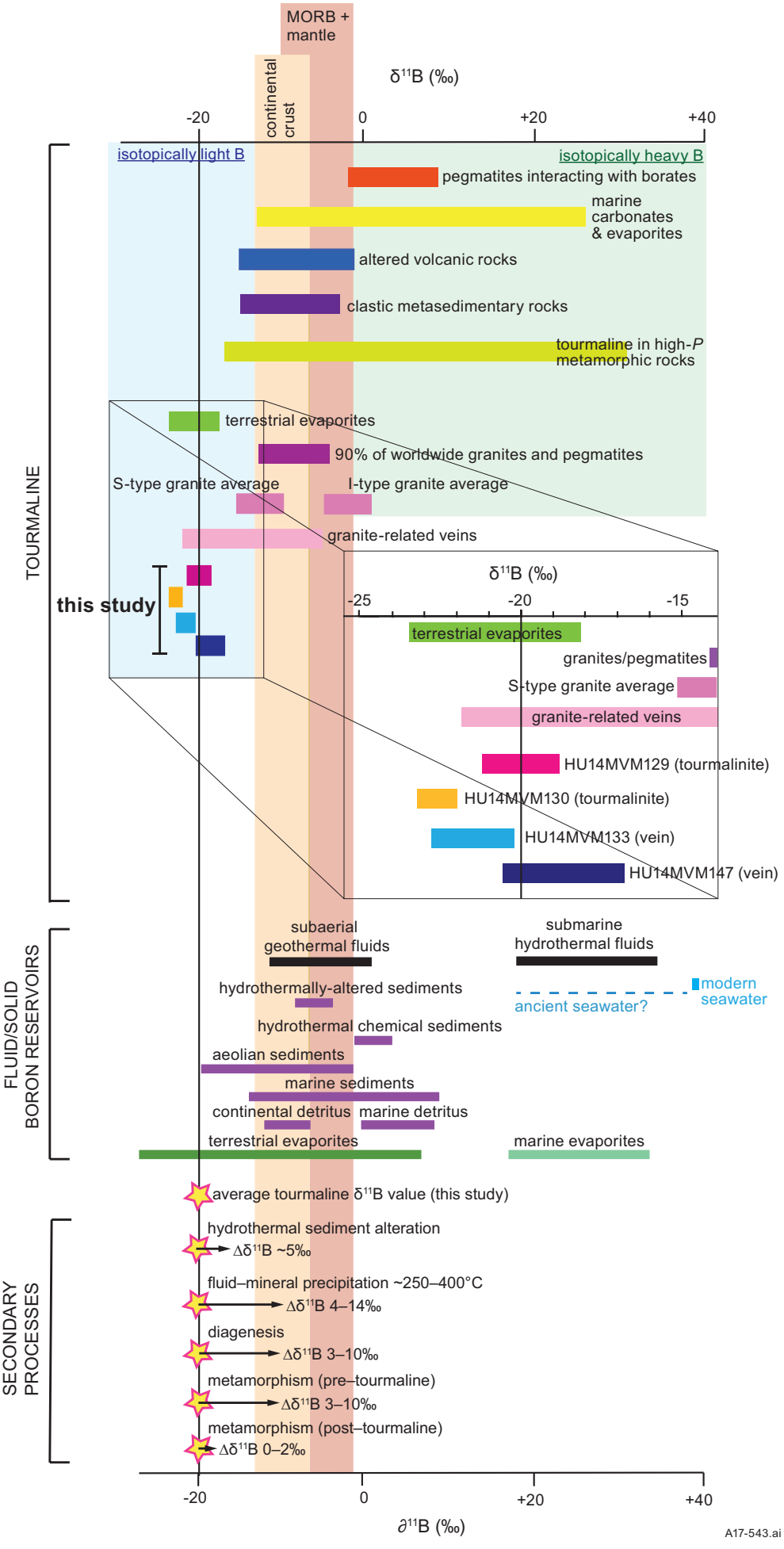

Figure 17. $\delta^{11}B$ values from this study together with $\delta^{11}B$ values from geological reservoirs of tourmaline, along with various solid rock and fluid $\delta^{11}B$ values compiled from worldwide boron isotope data. Maximum internal precision errors on samples from this study = 0.15‰. MORB = mid-ocean ridge basalt. Diagram adapted from Marschall and Jiang (2011) including data and references within Spivack *et al* (1987), Slack *et al* (1989), Palmer and Slack (1989), Palmer (1991), Ishikawa and Nakamura (1993), Jiang and Palmer (1998), Simon *et al* (2006), Trumbull and Slack (2011), Xiao *et al* (2013), Romer and Meixner (2014) and Trumbull and Slack (2018).

and for the tourmaline-bearing quartz veins in the Jervois mineral field. This proposal is consistent with a granite-related model suggested by Raith *et al* (2004) for the Bonya Hills area.

However, it is unlikely that a magmatic source can explain the $\delta^{11}B$ values from the tourmalinite samples. The only known occurrences of S-type granites in the Bonya Hills area and the Jervois mineral field are restricted regionally to minor phases of the post-D_3, strongly peraluminous Samarkand Pegmatite. The Samarkand Pegmatite post-dates the formation of the tourmalinites (as discussed above); therefore, S-type magmas and their late-phase fluids are excluded as a primary boron source for the tourmalinites in the study area.

Terrestrial evaporites

The tourmaline $\delta^{11}B$ data for tourmalinites from our study (**Table 3** and **Figure 15**) plots towards the lower end of the range for worldwide boron isotope data and overlaps the range for terrestrial evaporites (**Figure 17**). Borate in modern-day terrestrial evaporites typically has extremely low $\delta^{11}B$ values (as low as -32‰); these values are distinct from that of marine evaporites ($\delta^{11}B$ values of +18 to +32‰; Xiao *et al* 2013) and modern seawater (+39.6‰; Swihart *et al* 1986, Vengosh *et al* 1992, Vengosh *et al* 1995, Foster *et al* 2010; **Figure 17**). In terrestrial settings, meteoric waters that interact with detrital clay and mica derived from continental sources are enriched in isotopically low boron. When these meteoric waters evaporate in salt pans, the precipitating borate minerals preferentially incorporate ^{10}B relative to the fluid. Because of the low temperature of the surficial evaporation process, the fractionation effect is substantial (Xiao *et al* 2013). The tourmaline $\delta^{11}B$ values in our tourmalinite samples (**Figure 17**) are consistent with a terrestrial evaporite source for boron; this is therefore interpreted as a possible primary source for the boron in the tourmalinites of the Jervois mineral field. Similarly low tourmaline $\delta^{11}B$ values (-23.1 to -17.2‰) at the Broken Hill deposit have also been interpreted as being sourced from terrestrial evaporites (Slack *et al* 1989).

This interpretation of a possible terrestrial evaporite boron source in the Jervois mineral field is consistent with Ypma (1985) who inferred a continental evaporite source derived initially from volcanogenic boron based on the interpreted local geological setting. However, there is no independent evidence for the former presence of terrestrial evaporites in the Jervois mineral field. Undiscovered evaporites may be present at depth in basal zones of the Bonya Metamorphics, but their absence (if they existed) is more likely explained by their lack of preservation in ancient rocks. Evaporites are rarely preserved in Proterozoic rocks because their primary constituents are generally leached and altered by the effects of subsequent burial, deformation, metamorphism and fluid flow (eg Warren 1997, Warren 2016). Pseudomorphs of former evaporite minerals (eg anhydrite, halite, albite, scapolite) are generally considered the most reliable mineralogical and textural evidence for precursor evaporites (eg Warren 1996, Warren 1997). To date, no evidence supporting the former existence of evaporites has been identified in the Bonya Metamorphics succession (Weisheit *et al* in review). Minor scapolite occurrences have been reported in the Jervois mineral field and the Bonya Hills area and at the Molyhil W–Mo skarn deposit west of the study area (see **Figure 1**; Ransom 1978, Bowen *et al* 1978, Shaw *et al* 1984). However, this scapolite is interpreted to be associated with skarn alteration and epigenetic mineralisation rather than evaporite sequences.

Considering that the low $\delta^{11}B$ values of tourmalinite are the only evidence for terrestrial evaporites in this setting, alternative explanations have been investigated (see below).

Potential effects of secondary processes

Circulating basin hydrothermal fluids

Evidence for large-scale boron exchange between basin water and basin rocks exists in many present-day basin hydrothermal systems (eg hydrothermal vents on ocean floors, continental hot springs; Palmer 1991, van Hinsberg *et al* 2011, Marschall and Jiang 2011, Dutrow and Henry 2011, Xiao *et al* 2013). This hydrothermal activity occurs in areas near volcanic, shallow magmatic, or geothermal systems. The boron concentration and boron isotope composition of hydrothermal fluids in basin settings are mainly controlled by the primary source of boron in host rocks or sediments that are leached by infiltrating hydrothermal fluids. Hydrothermal fluids easily leach boron from clastic sediments thereby increasing fluid boron concentrations (Spivack and Edmond 1987, Campbell *et al* 1988). Given that clastic sediments and sedimentary rocks typically have higher boron concentrations relative to seawater and freshwater (eg Xiao *et al* 2013), hydrothermal fluids can easily leach boron from these sources to produce boron-rich hydrothermal fluids (Spivack *et al* 1987, Spivack and Edmond 1987, Campbell *et al* 1988, Slack *et al* 1989); the $\delta^{11}B$ values of these boron-rich hydrothermal fluids, and any precipitated boron-bearing minerals, are therefore dominated by the $\delta^{11}B$ value of the sediment or host rock (Slack *et al* 1989). These authors suggested that hydrothermal leaching of boron from solid reservoirs produces minimal isotope fractionation (although more recent evidence suggests that this may not be true; see below).

Potential variation in boron concentrations and $\delta^{11}B$ values between precipitating boron-bearing minerals and the fluid in hydrothermal systems can occur depending on the degree of interaction between circulating fluids with wall rocks, the involvement of seawater, and fluid temperature variations (Palmer and Slack 1989). Therefore, the precise $\delta^{11}B$ value in the fluids of any such hydrothermal system will vary depending on fluid-rock ratios as fluids infiltrate crustal rocks. For example, in the Escanaba Trough of the Pacific Ocean, James *et al* (1999) report $\delta^{11}B$ values in pore fluids from a sediment-hosted hydrothermal system that range between -2.2 and +22.6‰ (significantly lower than modern seawater). The lowest end of this range is close to values of local unaltered sediment (-5‰), indicating a very low fluid-rock ratio in that system. Other examples are hydrothermal vent fluids at mid-ocean ridges that are enriched in boron compared to seawater (10–35%) that, in most cases, have lower $\delta^{11}B$ values (+26 to +37‰, Palmer and Slack 1989).

In the same study, vent fluids in the Marianas back-arc rift are reported to have boron concentrations that are double that of seawater, with $\delta^{11}B$ values of +20‰. Palmer and Slack (1989) concluded that such $\delta^{11}B$ values lower than seawater are generated by increasing the concentration of basalt-derived $\delta^{11}B$ in the circulating hydrothermal fluids (ie decreasing the fluid-rock ratio).

Hydrothermal fluids circulating in continental settings associated with volcanism or shallow magmatism have greater capacity to concentrate boron compared to those in mid-ocean ridge settings and in sedimentary terranes that lack significant local magmatism (Slack 2002). Present-day freshwater contains low boron concentrations (≤0.2 ppm) compared to seawater (~4.6 ppm); both reservoirs generally contain low concentrations of boron compared to hydrothermal fluids in crustal rocks (up to 0.2 wt%, average of ~10–50 ppm; Ellis and Mahon 1977, Swihart *et al* 1986, Spivack and Edmond 1987, Warren 2010, Xiao *et al* 2013 and references therein). The boron isotope compositions in these hydrothermal fluids span a large range of values (-9.3 to +54‰, Xiao *et al* 2013) and are primarily controlled by marine or terrestrial influences on the host basin. Subaerial geothermal fluids typically have lower $\delta^{11}B$ values than seawater and submarine hydrothermal fluids (**Figure 17**) because boron is ultimately derived from continental crust rather than seawater (Slack 2002). One exception are high $\delta^{11}B$ values between +51 and +54‰ from the Dead Sea where hydrothermal fluids are influenced by marine brines and marine evaporites (Xiao *et al* 2013).

Boron-rich hydrothermal fluids that precipitate boron-bearing minerals on or near the basin floor are likely to fractionate boron between the fluid and the precipitated mineral (Slack *et al* 1987, Palmer and Slack 1989). Values of $\delta^{11}B$ are systematically lower in boron-bearing hydrothermal precipitates than in the fluid from which they precipitated because ^{10}B preferentially partitions into the solid phase (Slack *et al* 1987). Experimental data indicates that boron isotope fractionation between tourmaline and hydrothermal fluids is temperature dependent (Palmer and Slack 1989). Suggested tourmaline–fluid fractionation factors vary between 2–3‰ at 750°C and 20–30‰ at 25°C. Meyer *et al* (2008) confirmed experimentally that this fractionation is temperature dependent; they reported a tourmaline $\Delta\delta^{11}B_{solid-fluid}$ of 4.2‰ at 400°C. Under temperature conditions considered relevant to tourmalinite and massive sulfide formation, ie 200–400°C (Spry *et al* 2000), precipitated tourmaline has $\delta^{11}B$ values 5–12‰ lower than the boron-bearing fluid from which it originated. For example, the Guaymas basin submarine hydrothermal system in the Gulf of California operates at fluid temperatures similar to those suggested for tourmalinite formation (ie at 250–300°C). Fractionation between the hydrothermal fluids and boron-bearing precipitates in this system are inferred to be $\Delta\delta^{11}B_{fluid-mineral}$ = 10–14‰ (Spivack *et al* 1987, Palmer and Slack 1989). Although significant fractionation of boron is evident in that system, $\delta^{11}B$ values are higher compared to the tourmaline $\delta^{11}B$ values from our study (**Figure 17**).

Therefore, in order to produce the low tourmaline $\delta^{11}B$ values from our study solely through temperature dependent fractionation during mineral precipitation, fluid temperatures of <<200°C would likely be required (based on a very conservative starting fluid $\delta^{11}B$ composition of +10‰ much lower than present day seawater). These lower temperatures appear to be unrealistic for boron-bearing fluids associated with massive sulfide mineralisation in most basin settings (Palmer and Slack 1989). Indeed, the synsedimentary mineralisation in the Jervois mineral field contains appreciable copper mineralisation (Bennett *et al* 2017) with copper transport typically requiring higher temperature fluids (ie >300°C, Liu and McPhail 2005). The assessment of worldwide tourmaline data from a range of massive sulfide deposits forming via different temperature hydrothermal fluids also shows that lower temperature systems still yield higher $\delta^{11}B$ values (eg >-10‰, Palmer and Slack 1989, Slack *et al* 1989) than the values in our study. There is no evidence for large variations in tourmaline $\delta^{11}B$ values at different fluid temperatures; instead, the primary boron source appears to be a more important control (Palmer and Slack 1989, Slack *et al* 1989).

There are few boron isotope data available from boron-bearing hydrothermal chemical sediments precipitating in present-day subaqueous hydrothermal basin systems. In the Bauer basin, east of the East Pacific Rise in the Pacific Ocean, high boron concentrations have been measured in hydrothermal metalliferous sediments composed mainly of authigenic Fe–smectite and minor detrital aluminosilicates (Spivack *et al* 1987). The smectite likely formed *in situ* during diagenesis of the hydrothermal chemical sediments. $\delta^{11}B$ values of -1 to +5‰ are reported in the authigenic minerals. These $\delta^{11}B$ values are significantly lower than seawater but much higher than the tourmaline $\delta^{11}B$ values from our study (**Figure 17**); this suggests that our data require a lower $\delta^{11}B$ source.

Data from ancient deposits have been compared with $\delta^{11}B$ values from fluids at modern-day vent sites with inferred similar depositional settings (Palmer and Slack 1989, Palmer 1991). Unlike modern-day examples, tourmaline data from a variety of ancient depositional settings show a wide range of $\delta^{11}B$ values, spanning -25 to +20‰ (Palmer 1991). These data indicate that $\delta^{11}B$ values in hydrothermal precipitates (tourmaline or another precursor B-bearing mineral) are largely controlled by the dominant source of boron. As measured in modern-day hydrothermal fluids in basin settings, non-marine boron sources have lower $\delta^{11}B$ values relative to marine boron (eg Palmer 1991, Xiao *et al* 2013).

Boron-bearing basin sediment $\delta^{11}B$ values may be lowered by alteration caused by hydrothermal fluids. For example, Spivack *et al* (1987) report hydrothermally-altered sediments in drillholes from the Guaymas basin in the Gulf of California that are depleted in boron (1.2 ppm versus 33 ppm in unaltered sediments). The boron loss is accompanied by fractionation resulting in $\delta^{11}B$ values between -9.0 and -7.4‰, lower than unaltered material (-4.5 to +2.8‰). Hot springs in vents near the drillhole site, which presumably leached this boron, had boron concentrations 3–4 times that of seawater and $\delta^{11}B$ values between +16.5 and +23.2‰; this indicates that the hydrothermal fluid is preferentially enriched in ^{11}B as expected from experiments described above. Hydrothermal fluids may therefore scavenge boron from basin sediments and lower $\delta^{11}B$ values in the remaining sediments. If this process is repeated, it

would be possible to precipitate boron-bearing minerals from these fluids with even lower $\delta^{11}B$ values. Because fluid-assisted alteration would progressively remove boron, there must be a sufficiently large mass of sediment to retain enough boron in order to precipitate boron-rich minerals with a low $\delta^{11}B$ signature. It is plausible, therefore, that a boron-rich depositional setting with primary low $\delta^{11}B$ values (eg continentally-influenced rather than open marine basin) that underwent secondary hydrothermal alteration, could produce the low $\delta^{11}B$ values in the studied tourmalinites.

Secular variation in seawater

The tourmaline $\delta^{11}B$ values for tourmalinites from this study as shown in **Figure 17** are too low to be explained by present-day seawater $\delta^{11}B$ compositions (see Spivack *et al* 1987, Palmer and Slack 1989). However, seawater $\delta^{11}B$ values are not well constrained for the Palaeoproterozoic nor for possible long-term variations in boron isotope composition over geological time (eg Marschall and Jiang 2011, Greenop *et al* 2016, Marschall 2018). As secular variation in the isotopic composition of sulfur and oxygen in ancient seawater is well documented (eg Huston 1999, Farquhar *et al* 2010, Bekker *et al* 2010), it is reasonable to question whether the boron isotope composition of seawater has also fluctuated over time (Palmer and Slack 1989, Slack *et al* 1989). Although there has been some discussion about the potential for secular variation in seawater $\delta^{11}B$ over timescales of millions of years, only data corresponding to the Palaeozoic is available; this shows shifts of only ~20 $\delta^{11}B$ units (Simon *et al* 2006). Assuming similar variation in seawater $\delta^{11}B$ in the Palaeoproterozoic was possible, a negative shift of ~20 $\delta^{11}B$ units from modern day seawater is too small to explain the low tourmaline $\delta^{11}B$ values in our study (**Figure 17**). Indeed, tourmaline from Precambrian mineral deposits that formed through marine-influenced geological processes yield $\delta^{11}B$ values >+20‰ (eg Xavier *et al* 2008, Mercadier *et al* 2012). These positive marine boron isotope signatures are similar to modern-day seawater and inconsistent with possible large secular variation in seawater boron. Tourmaline $\delta^{11}B$ values from a range of global massive sulfide deposits and tourmalinites do not appear to show secular variation over geological time (Palmer and Slack 1989, Slack *et al* 1989). This contrasts markedly with sulfide and sulfate $\delta^{34}S$ values from hydrothermal VMS systems that fluctuate over geological time and appear to correlate directly with $\delta^{34}S$ values in coeval seawater, suggesting a clear influence from seawater on the sulfur source in these mineral systems (eg Huston 1999).

This suggests that even if seawater $\delta^{11}B$ values have varied with time, there was no apparent control on tourmaline $\delta^{11}B$ values in tourmaline in these deposits (Palmer and Slack 1989, Slack *et al* 1989). Consequently, the extremely low $\delta^{11}B$ signature of tourmaline in the study area likely precludes seawater as a major influence, regardless of any secular change in boron isotope composition.

Diagenesis

Most fluids residing in basin sediments are removed during diagenesis and low-grade metamorphism (Fyfe *et al* 1978), so it is likely that most boron mobility, assisted by fluid transfer, occurs during this low temperature stage of dewatering and rock formation (Romer and Meixner 2014). The texture and mineralogy of the tourmalinites, and the metasedimentary succession in the Jervois mineral field, are consistent with sandy and muddy protoliths (see **Results** and **Discussion**). These clay-bearing siliciclastic sediments would therefore provide an excellent potential source for low $\delta^{11}B$ values in the tourmalinites. Clay-bearing siliciclastic sediments are an important global reservoir for boron (Spivack *et al* 1987). Typical boron concentrations in deep sea sediments (≤17.5 ppm; Spivack *et al* 1987; Xiao *et al 2013*) are similar to average upper continental crustal abundances for boron (17 ppm; Rudnick and Gao 2014).

Maximum limits on boron mobility in basin sediments are constrained when boron is fixed in phyllosilicate minerals during metamorphism at temperatures of ≤300°C (Perry 1972). Studies of hydrothermally-altered basin sediments in the Nankai Trough, Japan, indicate that temperature-induced mobility of boron in sediments probably occurs at even lower temperatures (down to 100°C); above this temperature, no boron remains in secondary minerals (You *et al* 1995, James *et al* 1999).

Diagenesis of basin sediments can redistribute boron between exchangeable positions in precursor minerals, diagenetic pore fluids, and product minerals (Palmer and Slack 1989). Because basin sediments can contain high clay and zeolite mineral contents (eg smectite, kaolinite, illite, chlorite), large amounts of boron hosted in sheet silicate sites may be exchanged during diagenesis rather than remaining in the crystal lattice, bound to structural sites in these minerals (Palmer *et al* 1987, Romer and Meixner 2014). Boron isotopes can fractionate when boron is absorbed and desorbed between seawater, diagenetic fluids and clay minerals during diagenesis, and when clay minerals are progressively converted to low temperature metamorphic minerals with higher thermal stability (Spivack *et al* 1987, Palmer *et al* 1987, Palmer and Slack 1989). Whether boron is released during diagenesis from unstable phases in the rock depends on the formation and availability of boron sequestering phases at the time of fluid generation, which are most prevalent early during diagenesis. The mineralogy, porosity, and fluid composition of the sediments undergoing diagenesis are influenced by the basin depositional environment (Deyhle *et al* 2003, Romer and Meixner 2014).

Several diagenetic processes in basin sediments can fractionate boron by preferentially removing high-$\delta^{11}B$ boron from boron-bearing minerals and thereby lowering $\delta^{11}B$ values in the remaining sediments. Palmer *et al* (1987) report that repeated absorption and leaching of boron from seawater onto clay minerals at low temperatures (≤40°C) can fractionate $\delta^{11}B$ values by ≤10‰, mainly with changing pH. Similarly Spivack *et al* (1987) note that in low temperature (≤60°C) marine sediments, non-desorbable boron locked on the surface of mineral grains had lower $\delta^{11}B$ values (-4.3 to +2.8‰) compared to desorbable boron in pore waters (+13.9 to 15.8‰). Changes in $\delta^{11}B$ values during early diagenesis can also be caused by recrystallisation of carbonate and silica minerals, or through chemical transition between different clay minerals (ie smectite to illite; Ishikawa and Nakamura 1993). These studies indicate that boron

is highly mobile during diagenesis and can fractionate at low temperatures before being fixed in minerals, or removed from the sediment pile, during higher temperature diagenesis and metamorphism (eg Spivack *et al* 1987*)*.

Ishikawa and Nakamura (1993) attributed considerably lower $\delta^{11}B$ values measured in Permian- and Miocene-aged marine sediments compared to modern-day marine sediments (-17.5 to -5.6‰ versus -6.6 to +4.8‰) to diagenesis, suggesting that this process may change $\delta^{11}B$ by -3 to -10‰. In the same study, diagenetic illite with $\delta^{11}B$ values ranging between -23 to -4‰ were reported, considerably lower than the $\delta^{11}B$ value of the equilibrating diagenetic fluid. It is apparent therefore that diagenesis can produce negative shifts of ≤10 $\delta^{11}B$ units in basin sediments (Deyhle *et al* 2003, Romer and Meixner 2014).

The boron isotopic composition of modern-day ocean sediments ($\delta^{11}B$ values of -13 to +5‰; Xiao *et al* 2013) is controlled by the mixing of four different boron sources: continental detritus, marine clays, biogenic carbonate and biogenic silica (Ishikawa and Nakamura 1993). According to their study, these four sources have variable $\delta^{11}B$ values, the lowest being continental detritus (continental-derived illite from wind or fluvial transport) with average $\delta^{11}B$ values of -13 to -8‰. The tourmaline $\delta^{11}B$ values in the tourmalinites in the Jervois mineral field (**Figure 17**) are 6–15‰ lower than $\delta^{11}B$ values in modern-day continental detritus from basin sediments (Ishikawa and Nakamura 1993), so similar materials might provide a primary boron source for the studied tourmalinites, provided that another process like diagenesis further lowered the $\delta^{11}B$ values.

Metamorphism

The mobility of boron during metamorphism (and resulting boron isotope fractionation) is aided by the release of metamorphic fluids. It is largely controlled by the stability or breakdown of precursor boron-bearing minerals in the host rock and whether newly formed metamorphic minerals sequester or release boron under increasing metamorphic grade (Palmer and Slack 1989, Romer and Meixner 2014). Boron mobility and related isotope fractionation is also strongly dependent on the chemistry of the protolith and the pre-metamorphic and metamorphic mineral assemblages of the host rocks (Romer and Meixner 2014, Romer *et al* 2014).

When boron is sequestered *in tourmaline*, the effects of metamorphism on boron isotope fractionation are considered negligible (eg Spivack and Edmond 1987, Spivack *et al* 1987, Slack *et al* 1989, Palmer and Slack 1989). The mechanical and chemical stability of tourmaline appears to limit major changes in tourmaline $\delta^{11}B$ values during metamorphism (Palmer and Slack 1989, Slack *et al* 1989, van Hinsberg *et al* 2011a, van Hinsberg *et al* 2011b). The lack of chemical or isotopic zonation in the analysed tourmaline within the tourmalinites in our study (**Tables 2** and **3**) is consistent with tourmaline bulk chemistry reflecting pre-metamorphic compositions, without significant disturbance during metamorphism.

The interpretation that metamorphism had a negligible effect on $\delta^{11}B$ values *in tourmaline* is supported by worldwide tourmaline studies from tourmalinites and massive sulfide deposits. A wide range of tourmaline $\delta^{11}B$ values (-23 to +22‰) reported from tourmaline in several high-grade granulite facies terranes (Palmer and Slack 1989) show no correlation between increasing metamorphic grade and changing $\delta^{11}B$ values. It was inferred that tourmaline is not greatly affected by metamorphism, and that the pre-metamorphic host rock composition is the most significant control on boron isotope compositions in metamorphosed tourmaline. Similarly at Broken Hill, Slack *et al* (1989) reported no link between changing tourmaline $\delta^{11}B$ values and increasing metamorphic grade of country rocks. Only small shifts in tourmaline $\delta^{11}B$ values (decreases of ≤1.3 $\delta^{11}B$ units) were measured. These shifts were explained by fluid phase alteration during both prograde and retrograde metamorphism under amphibolite–greenschist facies conditions at ~500–300°C. However, this interpretation did not take into account how pre-metamorphic $\delta^{11}B$ values in host rocks, influenced by the original depositional environment, might affect tourmaline $\delta^{11}B$ values.

On the contrary, boron that resides in minerals less robust than tourmaline (eg clays, micas) can be mobilised and undergo significant changes in isotopic composition during metamorphism. Metamorphic fluids present after diagenesis (from breakdown of hydrous minerals) would continue to remove ^{11}B from country rocks (eg Palmer and Slack 1989, Slack *et al* 1989, Romer and Meixner 2014, Romer *et al* 2014). Comparison of the boron contents and bulk rock boron isotope ratios of medium- and high-grade metasedimentary rocks and their unmetamorphosed protoliths indicate boron loss up to 30–60% and lowering of $\delta^{11}B$ values (decrease of up to 8 $\delta^{11}B$ units; Romer and Meixner 2014).

As well as fluid-assisted ^{11}B loss, $\delta^{11}B$ values of metamorphosed rocks are also influenced by protolith chemistry. The isotopic composition of boron in precursor sedimentary rocks, even within the same stratigraphic unit, may vary by ≤20 $\delta^{11}B$ units as controlled by the source of the sediments, the environment of deposition (terrestrial, lacustrine, marine), and localised post-depositional alteration (Romer *et al* 2014). Non-metamorphosed rocks with originally low protolith $\delta^{11}B$ values (ranging from -4 to -24‰) can therefore produce even lower $\delta^{11}B$ values (decrease of 3–10 $\delta^{11}B$ units) in metamorphosed equivalents (Romer and Meixner 2014). Furthermore, variations in protolith composition directly control metamorphic assemblages and affect the stability of different minerals that might act as exchangeable boron reservoirs during metamorphism (Romer and Meixner 2014, Romer *et al* 2014). As metamorphic grade increases, the presence and stability of different boron sequestering minerals vary (eg muscovite, phengite, chlorite and paragonite); this potentially effects boron fractionation (Romer and Meixner 2014). Readers are referred to Romer and Meixner (2014) and Romer *et al* (2014) for further details on $\delta^{11}B$ exchange during metamorphism.

High-thermal gradient amphibolite facies metamorphism in the Jervois mineral field (>500°C and 0.1–0.2 GPa at ca 1.79 Ga; Weisheit *et al* in review) was initiated by the intrusion of bimodal magmas into an active sedimentary basin (Weisheit *et al* in review). The high temperatures attained early during basin evolution would have provided a good mechanism for boron mobility (eg effective circulation

of hot evolved seawater) through the host succession during and shortly after sedimentation. The original mineralogy of the metamudstone protolith, now observed as abundant magnetite-bearing micaceous schists of the Bonya Metamorphics, cannot be determined; however, it is reasonable to assume that early clay minerals deposited as basin muds were probably amorphous ferric-oxyhydroxide and aluminosilicate minerals (eg chamosite, illite, chlorite). Sub-greenschist facies metamorphism at ~300°C changes the crystal structure of clay minerals (Frey 1987) into stable crystalline minerals (eg white mica, chlorite, biotite, tourmaline). It is therefore likely that the majority of boron in the host succession would have been sequestered into stable minerals by this time, effectively limiting large-scale fractionation of boron to diagenesis and metamorphism early on in the basin history.

Overall, it appears unlikely that metamorphism alone can explain the low tourmaline $\delta^{11}B$ values from our study as shown in **Figure 17**. Once boron is sequestered in tourmaline, the tourmaline $\delta^{11}B$ values are unlikely to have been significantly affected by regional metamorphism (shift of ~1 $\delta^{11}B$ unit as per Slack *et al* 1989), and the bulk of any pre-metamorphic $\delta^{11}B$ values would be preserved. Based on the results of these studies, we interpret that peak-pressure metamorphic conditions in the Jervois mineral field at ca 1.76 Ga (550–620°C and 0.3–0.4 GPa; Weisheit *et al* in review) are likely to have caused only minor fluxes in boron (and minor shifts in $\delta^{11}B$) in pre-existing tourmaline related to the analysed tourmalinites. Nonetheless, providing that $\delta^{11}B$ values in the host succession were already relatively low before metamorphism (ie -5 to -15‰, as found in some terrestrially-influenced rocks), it remains entirely plausible that metamorphism during early basin evolution may have further lowered $\delta^{11}B$ values by 3–10‰ (as per Romer and Meixner 2014). Providing this fractionation occurred before tourmaline formed, this process could plausibly produce the tourmaline $\delta^{11}B$ values measured in the tourmalinites from the Jervois mineral field (**Figure 17**).

Summary model for tourmaline formation and boron sources

Figure 18 summarises proposed models of boron sources and hydrothermal processes involved in tourmaline formation for the synsedimentary tourmalinites in the Bonya Metamorphics and for the epigenetic tourmaline-bearing pegmatites and quartz veins of the Jervois mineral field and Bonya Hills. The isotopically low tourmaline boron data can be explained by three mechanisms:

- boron leached from terrestrial evaporitic borate by hydrothermal fluids to form tourmalinites
- boron leached from clay minerals (in a continentally-influenced basin that had undergone diagenesis/low temperature metamorphism) by hydrothermal fluids to form tourmalinites
- boron-bearing magmatic-hydrothermal fluids exsolved from S-type granites to form tourmaline-bearing pegmatites and quartz veins

S-type felsic magmatism is precluded as a source for boron in the tourmalinites because there is no evidence for S-type magmatism prior to D_2 in the study area. The leaching of borate from terrestrial evaporites may provide a primary low $\delta^{11}B$ source for boron in the tourmalinites (**Figure 18a**), but rocks of this type have not been recognised in the region. Instead we propose that boron was derived from continentally-influenced basin sediments. These sediments underwent secondary processes related to diagenesis and low-grade metamorphism that lowered $\delta^{11}B$ values in basin sediments before boron was fixed in tourmaline (**Figure 18b**). The former presence of terrestrial evaporitic borate as a primary boron source for the tourmalinites cannot be confirmed independently, whereas mica-schists in the Bonya Metamorphics confirm the presence of mudstones and clay-rich sediments in the palaeobasin.

Based on the available data, we propose that the tourmalinites formed in a mud-rich palaeobasin undergoing active hydrothermal chemical sedimentation and mineralisation as part of a synsedimentary hydrothermal system at ca 1.79 Ga (**Figure 18c**). This hydrothermal activity was likely driven by the high thermal gradient caused by abundant, shallow bimodal magmatism of the Baikal Supersuite. Under these conditions, progressive B-isotope fractionation during dewatering by diagenesis and low-grade metamorphism would act to enrich basin sediments in ^{10}B, thus ultimately yielding the low $\delta^{11}B$ tourmaline values in the tourmalinites. A continentally-influenced basin would contain high boron concentrations necessary to produce boron-rich hydrothermal precipitates. Boron derived from continentally-influenced clay minerals in the basin sediments would have been transported in hydrothermal fluids circulating below the basin floor. These hydrothermal fluids are interpreted to have been driven by heat from shallow magmatism, and to have deposited boron-rich precursor sediments or tourmaline, along with other exhalites and metalliferous sediments, on or near the subaqueous basin floor. The boron-rich sediments, other exhalites and base metal mineralisation in the Jervois mineral field were subsequently metamorphosed and deformed to produce the observed tourmalinites, metaexhalites and metamorphosed base metal mineralisation. After the tourmaline in the tourmalinites formed (before or early during D_2), the effects of regional metamorphism or hydrothermal alteration are unlikely to have caused more than a negligible change in tourmaline $\delta^{11}B$ compositions.

Based on isotopic evidence and field relationships, an S-type granite-related model is proposed for the post-D_3 tourmaline-bearing pegmatites and quartz veins that are associated with epigenetic copper and tungsten mineralisation at ca 1.73–1.70 Ga in the Bonya Hills area (**Figure 18d**). There appears to be little reason to seek an alternative explanation for the origin of this tourmaline considering the consistent field relationships between these tourmaline samples, mineralisation and felsic intrusions.

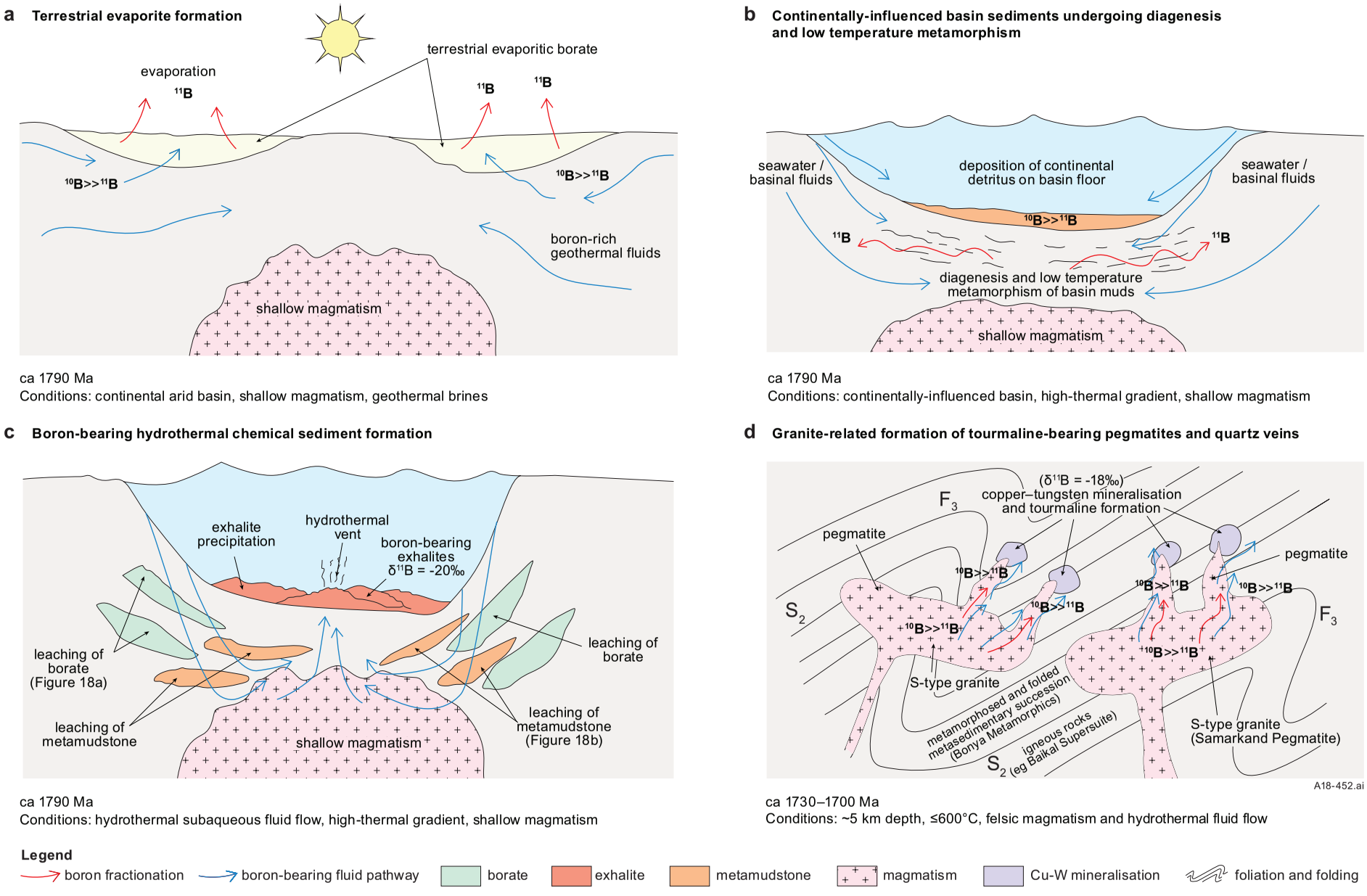

Figure 18. Schematic sketches showing proposed sources of boron and mechanisms for tourmaline formation in the study area.

IMPLICATIONS OF THIS STUDY

Depositional environment and tectonic setting

The Aileron Province is considered a fundamental region for understanding the Proterozoic evolution of the Australian continent (eg Giles *et al* 2002*,* Betts and Giles 2006, Betts *et al* 2016). The province is interpreted to have been influenced by back-arc basin formation in the Palaeoproterozoic during protracted, north-directed plate subduction along or near the southern North Australian Craton margin (eg Shaw *et al* 1984, Maidment *et al* 2005, Betts and Giles 2006, Betts *et al* 2011, Scrimgeour 2013, Howlett *et al* 2015, Huston *et al* 2016, Betts *et al* 2016).

The proposed mechanisms for forming tourmaline in the study area have potential implications for the depositional environment and tectonic setting of Palaeoproterozoic rocks in the northeastern Aileron Province. We propose that the abundant tourmaline in the study area, and the low tourmaline $\delta^{11}B$ values from the granite-related tourmaline and the tourmalinites, are all ultimately the product of a terrestrial or continentally-influenced basin setting enriched in boron. This setting is consistent with a proposed continental back-arc palaeobasin for the study area (Weisheit *et al* in review*).* This interpretation also provides new evidence for plate margin processes and tectonic conditions at the southern margin of the North Australian Craton.

The very low tourmaline $\delta^{11}B$ values from the tourmalinites (**Table 3** and **Figure 17)** are distinctly non-marine. If the boron isotope data are interpreted as evidence for terrestrial evaporitic borate, the former presence of terrestrial evaporitic borate would point to a specific terrestrial depositional environment. Terrestrial borate forms as terrestrial waters evaporate in closed or restricted basins isolated from oceans (Warren 2010, Steinmetz 2017). Terrestrial evaporites are a product of an arid climate and high topographic relief in basins located in active or former active volcanic terrains (Condie *et al* 2001, Evans 2006, Warren 2010, Warren 2016). These extensional basins are considered the far-field product of collisional tectonics at volcanogenically-influenced plate margins (Warren 2010, Helvaci and Palmer 2017). This setting is consistent with the proposed continental back-arc basin for the study area in the Paleoproterozoic.

Instead of a terrestrial evaporite source, we interpret the low $\delta^{11}B$ values from the tourmalinites as evidence for siliciclastic input from terrestrial rather than marine sources. The presence of continentally-derived muds in precursors to the Bonya Metamorphics in the Jervois mineral field implies a continentally-influenced depocentre. The abundance of tourmaline-rich rocks in the study area supports a palaeoenvironment where boron was available in high concentrations. Hydrothermal fluids circulating in boron-rich continental crust, associated with magmatism have greater capacity to concentrate boron by leaching primary minerals from these rocks, particularly compared to fluids in mid-ocean ridge or more passive sedimentary terranes (Slack 2002, Arnorsson 2004).

In order to generate an abundance of continentally-derived muds in a basin setting, several scenarios are plausible: either a marine basin with high input from continental detritus (and relative lack of marine detritus); or alternatively, a hydrologically-closed or restricted basin. Both could generate the required terrestrial-influenced setting (eg Ishikawa and Nakamura 1993, Romer *et al* 2014). With the former scenario, continental detritus would likely be derived from erosion and transport of continental rocks with a strongly felsic composition. This terrestrial detritus is required in order to generate a basin succession with high boron contents and low $\delta^{11}B$ values. Hydrothermal settings in marine basin environments, such as black smoker systems at mid-ocean ridges, are unlikely to host the required sediments. Despite a volcanogenic association, sediments and rocks in these settings generally have a strong influence from seawater and form from marine rather than continental detritus.

Boron isotope evidence suggests that the post-D_3 granite-related tourmaline in our study area is derived from local S-type magmatism at ca 1.73–1.70 Ga. This late stage magmatism is characterised by volatile-rich, highly fractionated pegmatites ie the Samarkand Pegmatite. The origin of these rocks is unclear, but a (meta)sedimentary (ie S-type) source is indicated by the presence of locally-developed garnet and high normative corundum in the whole rock geochemistry (Weisheit *et al* in review). Continentally-derived sedimentary rocks provide an abundant reservoir of boron. If such rocks also contained continentally-derived boron, initially low $\delta^{11}B$ values could have been inherited, and then fractionated further, in the tourmaline-bearing Samarkand Pegmatite and associated quartz veins.

Ore-forming processes and exploration

Metaexhalites

The occurrence of tourmalinites and other metaexhalites in any geological terrain are significant for mineral exploration because such rocks are often spatially associated with metamorphosed massive sulfide deposits (Stanton 1972, Plimer 1988, Hoffman 1993, Huston *et al* 2006d, Slack *et al* 2000, Spry *et al* 2000); therefore, the identification of metaexhalites can lead to new exploration targets. Exhalite packages (and their metamorphosed equivalents) indicate fossil hydrothermal fluid sites (Spry *et al* 2000). In many cases, if exhalites can be mapped spatially, they can potentially provide useful vectors towards hydrothermal fluid sites, and by inference, potential base metal mineralisation targets.

Although many types of exhalite in a variety of geological settings are unrelated to economic mineralisation, tourmalinites are an exception as they are most commonly associated with stratabound massive sulfide deposits (Slack 2002). Tourmalinites are linked to vent sites at a number of VMS or clastic-dominated sediment-hosted deposits (eg Broken Hill-, Sullivan- or Selwyn-type deposits; Spry *et al* 2000, Leach *et al* 2010).

The recognition of tourmalinites in the Jervois mineral field is particularly pertinent since these rocks have previously been considered absent by some authors in the Arunta Region (Shaw 1990). Where (meta)exhalites occur in lower metamorphic facies and/or less deformed terranes,

the links between any exhalites and mineralisation are usually clearer. However, as shown in the study area, it can be difficult to identify these assemblages when they are metamorphosed to higher grades. Outcropping metaexhalites are typically discrete, thin, linear features interlayered within more voluminous lithologies. Consequently, identifying their unusual mineralogy, particularly in weathered outcrops may be difficult. Subtle outcrops can be easily overlooked or mistaken for other rock types (eg amphibolite, chert, graphitic sedimentary protoliths, banded iron formation; Ypma 1986, Slack 2002).

As well as being associated with synsedimentary massive sulfide mineralisation, metaexhalites can also provide structural or chemical traps for later mineralising fluids. For example, garnetites and associated garnet-biotite-magnetite schist in the Jervois mineral field, interpreted as metaexhalites, host epigenetic vein and breccia styles of base metal mineralisation (Ypma 1986, this study). The coarse-grained nature of garnet porphyroblasts in these rocks, and the competency contrasts between different compositional layers in the interlayered schists, allows preferential infiltration of mineralising fluids and potential structural traps for mineralisation. In addition, as seen at the Rockface deposit, the high Fe and Mn concentrations of garnet-bearing rocks may also provide chemically-reactive layers that act as reductants for epigenetic copper- and tungsten-bearing mineralising fluids (see McGloin 2017, McGloin et al 2018, McGloin *et al* in prep).

Evaporites

The tourmaline boron isotope data hint at the possibility of terrestrial evaporites in the Jervois mineral field. Although there is no other available evidence for these rocks and we favour an alternative explanation, we cannot refute this possibility entirely. If the primary boron reservoir for tourmaline in the analysed tourmalinites from the Jervois mineral field was terrestrial evaporites, these evaporites would provide a locally accessible source of chloride for generating highly saline brines with increased capacity for metal transport in an active synsedimentary mineral system (as discussed for evaporite-bearing settings in Warren 1997). Evidence from several styles of mineralisation worldwide suggests that the presence of evaporites can be critical for mineral deposit formation (eg Barton and Johnson 1996, Warren 1997, Wilkinson 2014). Leaching of evaporites (commonly containing abundant chloride) would increase fluid salinity. Increased salinity in these hydrothermal fluids would enhance the scavenging and transport of copper, lead and zinc because these metals are transported effectively by chloride complexes (eg Huston *et al* 2006d, Liu and McPhail 2005, Yardley 2005). The possible former presence of evaporites in the Jervois mineral field would therefore enhance its exploration potential for base metal mineralisation. Evaporite occurrences found in other similar metasedimentary successions in the rest of the northeastern Aileron Province would also likely enhance their exploration potential for a wide range of hydrothermal mineral deposits, including sediment-hosted, BHT, iron-oxide–copper–gold (IOCG), and skarn deposits.

Indications of a Broken-Hill type mineral system

The metaexhalites, alteration, and synsedimentary mineralisation found in the Jervois mineral field are consistent with other terranes known to host stratabound base metal mineralisation. Examples include:

- BHT deposits in Australia: eg Broken Hill and Pinnacles in the Curnamona Province (Stanton 1972; Plimer 1988, Parr and Plimer 1993); Cannington and Pegmont in the Eastern Succession of the Mount Isa Inlier (Spry *et al* 2000)
- VMS deposits: eg Boliden, Finland (Mercier-Langevin *et al* 2013); Montauban, Grenville (Tomkins 2007) and Lemarchant, Newfoundland, Canada (Lode *et al* 2015)
- Other loosely- or non-classified deposits with similar geological affinities to VMS and BHT deposits: eg Sullivan, Canada (Slack *et al* 2000); Falun and Zinkgruvan, Bergslagen district, Sweden (Hedstroem *et al* 1989; Kampmann *et al* 2017); Gamsberg and Swartberg, Aggeneys District, South Africa (Ryan *et al* 1986, Hoffman, 1993).

Although some aspects of models for BHT mineralisation are somewhat controversial, herein we propose a synsedimentary BHT mineralisation model for the Jervois mineral field. This is achieved by comparing the available evidence with characteristics of other basin-hosted mineralisation styles (eg sediment-hosted and VMS mineralisation), whilst recognising that there is likely to be a continuum between some of these basin-hosted mineral systems (eg Gilmour 1976, Huston *et al* 2006d, Leach *et al* 2010). BHT-style mineralisation in the Jervois mineral field is preferred to other basin-hosted mineral systems for a number of reasons as outlined below.

Exhalites (and metamorphosed equivalents) are rarely reported in clastic-dominated (SEDEX) and Mississippi Valley-type (MVT) sediment-hosted deposits (eg McArthur River, Mount Isa, Century in Australia; Plimer 1994, Huston *et al* 2006d, Leach *et al* 2005, Leach *et al* 2010); this fact likely precludes this style of mineralisation for the Jervois mineral field. In contrast, BHT and VMS deposits are interpreted to form in active, volcanic- and magmatic-associated basin settings with high-thermal gradients (eg Huston *et al* 2006d). Mineralising fluids in BHT and VMS systems require a high temperature heat source to circulate brines through the basin succession. This heat source is generally provided by shallow level magmatism that generates elevated thermal gradients (eg Huston *et al* 2006d, Leach *et al* 2010). By comparison, McArthur- or Mount Isa-type mineralisation generally forms from lower temperature brines in passive extensional settings (continental sag basins) that lack active volcanism and magmatism contemporaneous with sedimentation (eg Leach *et al* 2005, Leach *et al* 2010). Such a passive environment allows the deposition of anoxic shales and tends to have stronger marine influences; mineralisation is associated with both organic-rich and abundant carbonate-bearing sedimentary rocks. These combinations of rocks are not observed in the Jervois mineral field and the Bonya Hills area.

There is no strong evidence for volcanic rocks hosting the mineralisation in the Jervois mineral field; this fact indicates that a VMS-style origin of the mineralisation is unlikely. Although there is strong evidence for contemporaneous shallow intrusive magmatism occurring during mineralisation (Reno *et al* 2016, Weisheit *et al* in review), irrefutable evidence for volcanic rocks have not been identified in the host succession; only circumstantial evidence for volcanic rocks has been suggested in previous studies [ie Ypma *et al* (1984) and Peters *et al* (1985)].

A number of authors have previously interpreted BHT mineralisation in the Jervois mineral field based on geological observations (Dobos 1978, Teale 1982, Ypma *et al* 1984, Mackie 1984, Ypma 1991, Walters 1996, Spry *et al* 2009). This Record provides the first direct isotopic evidence that supports a link with BHT mineralisation. The tourmaline $\delta^{11}B$ values reported for the Jervois mineral field (**Figure 17**) are among the lowest values recorded to date in any geological environment. The $\delta^{11}B$ values are similar to those reported for tourmaline associated with Pb-Zn-Ag mineralisation at Broken Hill, previously considered unique to that deposit (eg -23.1 to -17.2 ‰; Slack *et al* 1989). $\delta^{11}B$ values in tourmalines or tourmalinites from other massive sulfide deposits are higher, eg -13.8 ‰ or more (Xiao *et al* 2013).

Our study follows the interpretation presented for Broken Hill (Slack *et al* 1989) whereby unusually low boron isotope values in the tourmalinites are sourced primarily by hydrothermal leaching of a boron reservoir with low $\delta^{11}B$ values [Slack *et al* (1989) favoured terrestrial evaporites]. As an alternative to terrestrial evaporites, we propose that the low $\delta^{11}B$ values in our study are more likely derived from continentally-influenced basin muds that underwent diagenesis and metamorphism early during basin evolution. The evidence suggests that high thermal gradient conditions and synsedimentary hydrothermal activity in the Jervois mineral field are suitable for generating the required boron isotope fractionation during syngenetic and diagenetic processes; this is consistent with BHT ore formation.

Complementary to the boron isotope evidence from the tourmalinites, other more general geological characteristics from the Jervois mineral field support a BHT mineral system. Commonly, tourmalinites have been linked to reduced fluids in hydrothermal vent systems associated with VMS or clastic-dominated sediment-hosted deposits (eg Broken Hill-, Sullivan- or Selwyn-type deposits; Spry *et al* 2000, Leach *et al* 2010). More generally, metaexhalites are also usually found spatially and temporally associated with mineralisation at Broken Hill (Stevens *et al* 1988, Plimer 1994, Huston *et al* 2006d, Heimann *et al* 2009, Stevens 2015) and other global examples of BHT and metamorphosed massive sulfide deposits (eg Cannington, Pinnacles and Pegmont in Australia; several deposits in Bergslagen, Sweden; Stanton 1972, Plimer 1988, Hoffman 1993, Slack *et al* 2000, Spry *et al* 2000). The observation that metaexhalites (tourmalinites, garnetites, banded iron formation) outcrop in the Jervois mineral field supports the interpretation that metamorphosed base metal sulfide mineralisation in the Jervois mineral field has affinities to BHT mineralisation.

A link with Broken Hill is also supported by gross similarities in host lithological packages, which includes predominantly metasedimentary successions with significant components of syn- to post-depositional mafic and felsic magmatism. Furthermore, there are metallogenic similarities between the northeastern Aileron Province and the Curnamona Province (host of Broken Hill). Like the epigenetic copper and tungsten mineralisation evident in the study area (eg McGloin and Weisheit in review), the Curnamona Province is also host to epigenetic copper and tungsten mineralisation. Examples of copper-(gold-molybdenum) mineralisation in the Curnamona Province include the Kalkaroo and Portia deposits, which are related to the Olarian orogeny (Skirrow and Ashley 2000, Fitzherbert and Downes 2017, Giles and Just 2017). Syn- and post-tectonic tourmaline-bearing pegmatites that are associated with tungsten and tin mineralisation also occur at the Freyers and Hual Byjerkenrno mines (Fitzherbert and Downes 2017). These deposits and prospects in the Curnamona Province formed significantly later than interpreted synsedimentary lead-zinc-silver mineralisation (typified by the main ore bodies at the Broken Hill deposit, Groves and Plimer 2017). This pattern of younger epigenetic and granite-related mineralisation spatially overlapping older synsedimentary and basin-related mineralisation, usually punctuated by metamorphism, appears to be a common occurrence in Proterozoic Australia. Similar relationships where epigenetic copper mineralisation forms after basin evolution, deformation and inversion are also apparent for the Mount Isa Inlier (eg Large *et al* 2005, Oliver *et al* 2008).

The interpreted BHT classification for the synsedimentary mineralisation at the Jervois mineral field (Dobos 1978, Teale 1982, Ypma *et al* 1984, Mackie 1984, Ypma 1991, Walters 1996, Spry *et al* 2009, this study) is significant because BHT deposits are not generally thought to occur specifically in back-arc settings but rather in epicontinental basin or intracontinental rift environments (eg Stevens *et al* 1988, Laing 1996, Walters 1998, Parr and Plimer 1993, Huston *et al* 2006). A BHT deposit is therefore unexpected in this part of the NAC. The available evidence from local and regional studies indicates that BHT mineralisation in the Jervois mineral field formed early during palaeobasin evolution in a continental back-arc basin without rifting (eg Weisheit *et al* in review); this is consistent with the distinct non-marine boron isotopic signature reported in this study.

This interpretation challenges the paradigm of exploration models for BHT deposits on the Australian continent. With the exception of the Jervois mineral field, Australian examples of Proterozoic BHT deposits are hosted within a Paleo–Mesoproterozoic north-south linear belt known by several names (eg Carpentaria or North Australian Zinc or Diamantina Belt; eg Laing 1996, Cooke *et al* 2000, Leach *et al* 2010). This belt of sedimentary and metasedimentary basins incorporates parts of the McArthur Basin, Mount Isa Inlier and Curnamona Province (**Figure 19**) and represents the world's largest mineral endowment of zinc and lead (Laing 1996, McGoldrick and Large 1998, Cooke *et al* 2000, Leach *et al* 2010). The belt is famous for hosting large ca 1.69–1.57 Ga, clastic dominated, sediment-hosted Zn(Pb-Ag) deposits such as the supergiant Broken Hill deposit and other world-class

Figure 19. Map of Australia showing Proterozoic provinces containing major Zn-Pb deposits (red), including those associated with the Australian Carpentaria/Diamantina Zn-Pb belt, relative to the location of the study area (green star) in the Aileron Province (brown). Map modified from Walters (1996) and Leach *et al* (2010).

examples of stratabound sulfide mineralisation (eg McArthur River mine in the McArthur Basin, Cannington, Mount Isa and Century mines in the Mount Isa Inlier). BHT mineralisation in the Jervois mineral field occurs outside that currently defined mineral belt; however, it shares many similarities with the deposits and geology found therein. The interpretation of BHT mineralisation in the Jervois mineral field opens up the Aileron Province and other underexplored areas of Proterozoic Australia for discovery of new BHT and related mineral systems.

Use of tourmaline as an indicator mineral

With the appropriate geological context, this study has effectively constrained sources of boron and determined the genesis of tourmaline in the study area. The results of the study indicate two different styles of tourmaline associated with different styles of mineralisation punctuated by high-temperature and pressure metamorphism and deformation: 1) synsedimentary boron deposited in a subaqueous basin setting as part of an exhalative or replacement hydrothermal process associated with base metal sulfide mineralisation in a BHT setting; and (2) granite-related boron associated with magmatic-hydrothermal fluids that formed epigenetic copper- and tungsten-mineralised veins. These results demonstrate that tourmaline isotope and major element geochemistry has great potential for use by explorers as an indicator for mineralising and geological processes in the Aileron Province.

ACKNOWLEDGEMENTS

The NTGS basement mapping team contributed much of the regional geologic interpretation covered in this Record. We particularly thank Eloise Beyer, Barry Reno, Jo Whelan and Stefan Kraus for their input. We also acknowledge past mapping and sample collection by Max Frater. We would like to thank Graham Hutchinson at Hutchinson Geoscience for assistance with tourmaline microprobe analyses at Melbourne University. Karsten Goemann and Sandrin Feng are thanked for MLA and SEM analyses at CODES, Tasmania. Jay Carter and Max Heckenberg (NTGS Core Facility Alice Springs) and Nigel Saunders (NTGS Darwin) are thanked for providing field and sample assistance. We thank Michael and Denise Broad at Jervois Station for land access and KGL Resources Limited (particularly Martin Bennett) for field assistance and an introduction to some of the tourmalinites. David Huston (Geoscience Australia), John Slack (USGS), and Jo Whelan, Eloise Beyer and Greg MacDonald (NTGS) are thanked for their constructive reviews of this work. Thanks to Kathy Johnston, Marianne Fuller and Ian Burgan (NTGS) for figure preparation and formatting.

REFERENCES

Andriessen PAM, Hebeda EH, Simon OJ and Vershure RH, 1991. Tourmaline K–Ar ages compared to other radiometric dating systems in Alpine anatectic leucosomes and metamorphic rocks (Cyclades and southern Spain). *Chemical Geology* 91, 33–48.

Arnorsson S, 2004. Environmental impact of geothermal energy utilization, *Geological Society London Special Publication* 236, 297–336.

Barton MD and Johnson DA, 1996. Evaporitic-source model for igneous-related Fe oxide–(REE–Cu–Au–U) mineralisation. *Geology* 24, 259–262.

Bassano KA, Hergt JM, Maas R, Woodhead JD and Kamenetsky MB, 2012. Neoproterozoic uranium in Australia's giant 1.5–1.7 Ga base metal deposits: a

record of hydrological change related to the break-up of Rodinia? *34th International Geological Congress (IGC), 5–10 August 2012, Brisbane*.

Bennett MR, McGloin MV, Schmidt S and Schaubs P, 2017. The Jervois Cu-Ag (Pb-Zn-Au) Mineral Field: in Phillips N (editor). '*Australian Ore deposits*. *AusIMM Monograph* 32'. Australasian Institute of Mining and Metallurgy, Melbourne 557–560.

Bekker A, Slack JF, Planavsky N, Krapež B, Hofmann A, Konhauser KO and Rouxel OJ, 2010. Iron formation: the sedimentary product of a complex interplay among mantle, tectonic, oceanic, and biospheric processes. *Economic Geology* 105, 467–508.

Betts PG and Giles D, 2006. The 1800–1100 Ma tectonic evolution of Australia. *Precambrian Research* 144, 92–125.

Betts PG, Giles D and Aitken A, 2011. Palaeoproterozoic accretion processes of Australia and comparisons with Laurentia. *International Geology Review* 53, 1357–1376.

Betts PG, Armit RJ, Stewart J, Aitken ARA, Ailleres L, Donchak P, Hutton L, Withnall I and Giles D, 2016. Australia and Nuna: in Murphy JB, Keppie JD and Hynes AJ (editors). '*Ancient orogens and modern analogues'. Geological Society of London Special Publication* 327, 371–405.

Beyer EE, Reno BL, Whelan JA and Weisheit A, 2016. Geochemical evidence for an evolving tectonic setting in the northeastern Aileron Province, central Australia. *Record of Abstracts. Australian Earth Sciences Convention, 26–30 June, Adelaide, Australia.*

Beyer EE, Reno BL, Weisheit A, Meffre S, Thompson J and Woodhead JD, in prep. Summary of results. NTGS laser ablation ICP-MS U–Pb-Hf geochronology project: selected samples from JINKA 1:100 000 mapsheet area, Aileron and Irindina provinces, Arunta Region, January 2015–December 2017. *Northern Territory Geological Survey, Record*.

Beyer EE, Reno BL, Weisheit A, Whelan JA, Thompson JM, Meffre S, and Woodhead JD, 2018. Summary of results. NTGS laser ablation ICP–MS U–Pb–Hf geochronology project: selected samples from JERVOIS RANGE 1:100 000 and TOBERMOREY 1:250 000 mapsheets, Aileron and Irindina provinces, January 2014 – December 2016. *Northern Territory Geological Survey, Record 2018–001*.

Bjorlykke K, 1997. Lithological control on fluid flow in sedimentary basins: in Jamtveit B (editor). '*Fluid Flow and Transport in Rocks*'. Chapman and Hall.

Bowen BK, Henstridge DA and Paine GG, 1978. A note on the geology of scheelite mineralisation, Bonya Bore Area, NT, Central Pacific Minerals. *Northern Territory Geological Survey, Open File Company Report* CR1978−0104.

Buick IS, Frei R and Cartwright I, 1999. The timing of high-temperature retrogression in the Reynolds range, central Australia: constraints for garnet and epidote Pb−Pb dating. *Contributions to Mineralogy and Petrology* 135, 244–254.

Campbell AC, Palmer MR, Klinkhammer GP, Bowers TS, Edmond JM, Lawrence JR, Casey JF, Thompson G, Humphris S, Rona P and Karson JA, 1988. Chemistry of hot springs on the Mid Atlantic Ridge: TAG and MARK Sites. *Nature* 335, 514-519.

Catanzaro EJ, Champion CE, Garner EL, Maienko G, Sappenfield KM and Shields WR, 1970. Boric acid: isotopic and assay standard reference materials. *National Bureau Standards (US). Special Publication* 260, 17–70.

Chapman RE, 1987. Fluid flow in sedimentary basins: a geologist's perspective: in Goff JC and Williams BPJ (editors). '*Fluid flow in sedimentary basins and aquifers', Geological Society Special Publication* 34, 3–18.

Chen C, Depaolo DJ and Lan C, 1996. Rb–Sr microchrons in the Manaslu granite: implications for Himalayan thermochronology. *Earth and Planetary Science Letters* 143, 125–135.

Claoué-Long JC and Hoatson DM, 2005. Proterozoic mafic-ultramafic intrusions in the Arunta Region, central Australia. Part 2: Event chronology and regional correlations. *Precambrian Research* 142, 134–158.

Collins WJ and Teyssier C, 1989. Crustal scale ductile fault systems in the Arunta Inlier, central Australia. *Tectonophysics* 158, 49–66.

Condie KC, Des Marais DJ and Abbot D, 2001. Precambrian superplumes and supercontinents: a record in black shales, carbon isotopes, and paleoclimates? *Precambrian Research* 106, 239–260.

Cooke DR, Bull SW, Large RR and McGoldrick PJ, 2000. The importance of oxidized brines for the formation of Australian Proterozoic stratiform sediment-hosted Pb−Zn (Sedex) deposits. *Economic Geology* 95, 1−18.

Cross A, 2007. SHRIMP U–Pb xenotime and Re–Os molybdenite dating of the Molyhil scheelite-molybdenite skarn, northeastern Arunta Region, central Australia. *Research School of Earth Sciences, Annual Report 2007.* Australian National University, Canberra.

Dahl PS and Frei R, 1998. Step-leach Pb–Pb dating of inclusion-bearing garnet and staurolite, with implications for early Proterozoic tectonism in the Black Hills collisional orogen, South Dakota, United States. *Geology* 26, 111–114.

Deyhle A, Kopf AJ and Aloisi G, 2003. Boron and boron isotopes as tracers for diagenetic reactions and depth of mobilization using muds and authigenic carbonates from eastern Mediterranean mud volcanoes: in van Rensbergen RP, Hilhs AJ, Maltman and Morley CK (editors). '*Subsurface Sediment Mobilization*'. *Geological Society of London*, *Special Publication* 216, 491–503.

DeWolf CP and Mezger K, 1994. Lead isotope analyses of leached feldspars: constraints on the early crustal history of the Grenville Orogen. *Geochimica et Cosmochimica Acta* 58, 5537–5550.

Dobos S, 1978. *Phase relations, element distributions and geochemistry of metamorphic rocks from eastern Arunta Block, NT.* PhD Thesis, Macquarie University, Sydney.

Duncan RJ, Wilde AR, Bassano K and Maas R, 2006. Geochronological constraints on tourmaline formation in the Western Fold Belt of the Mount Isa Inlier, Australia: Evidence for large-scale metamorphism at 1.57 Ga? *Precambrian Research* 146, 120–137.

Duncan RJ, Buick IS, Kobayashi K and Wilde AR, 2014. Chemical and stable isotopic characteristics of

syn-tectonic tourmaline from the Western fold belt, Mount Isa inlier, Queensland, Australia. *Chemical Geology* 381, 131–143.

Duncan RJ and Maas R, 2014. Assessing the origin of old apparent ages derived by Pb stepwise leaching of vein-hosted epidote from Mount Isa, northwest Queensland, Australia. *Contributions to Mineralogy and Petrology* 168, 1085

Dutrow BL and Henry DJ, 2011. Tourmaline: a geologic DVD. *Elements* 7, 301–306.

Dyar MD, Wiedenbeck M, Robertson D, Cross LR, Delaney JS, Ferguson K, Francis CA, Grew ES, Guidotti CV, Hervig RL, Hughes JM, Husler J, Leeman W, McGuire AV, Rhede D, Rothe H, Paul RL, Richards I and Yates M, 2001. Reference minerals for microanalysis of light elements. *Geostandards Newsletter* 25, 441–463.

Ellis AJ and Mahon WAJ, 1977. *Chemistry and geothermal systems.* Academic Press, New York.

Evans DAD, 2006. Proterozoic low orbital obliquity and axial-dipolar geomagnetic field from evaporite palaeolatitudes. *Nature* 444, 51–55.

Fandrich R, Gu Y, Burrows D and Moeller K, 2007. Modern SEM-based mineral liberation analysis. *International Journal of Mineral Processing* 84, 310–320.

Farquhar J, Wu N, Canfield DE and Oduro H, 2010. Connections between sulfur cycle evolution, sulfur isotopes, sediments and base metal sulfide deposits. *Economic Geology* 105, 509–533.

Faure G and Mensing TM, 2005. *Isotopes: principles and applications.* Third edition. Wiley, Hoboken, New Jersey.

Feely RA, Gendron JF, Baker ET and Lebon GT, 1994. Hydrothermal plumes along the East Pacific Rise 8°40' to 11°50'N: Particle distribution and composition. *Earth and Planetary Science Letters* 128, 19–36.

Fitzherbert JA and Downes PM, 2017. Curnamona Province – geological history and mineral systems: in Phillips NP (editor). *'Australian Ore Deposits'. AusIMM Monograph* 32, 635–640.

Foster GL, Pogge von Strandman PAE and Rae JWB, 2010. Boron and magnesium isotopic composition of seawater. *Geochemistry Geophysics Geosystems* 11, 1–10.

Frater M, 2006. New insights into the Jervois mineral field: :in *'Annual Geoscience Exploration Seminar (AGES) Record of abstracts'. Northern Territory Geological Survey, Record* 2006-002.

Freeman MJ, 1986. *Huckitta, Northern Territory (Second Edition). 1:250 000 geological map series explanatory notes, SF53-11.* Northern Territory Geological Survey, Darwin.

Frei R and Kamber BS, 1995. Single mineral Pb–Pb dating. *Earth and Planetary Science Letters* 129, 261–268.

Frei R and Pettke T, 1996. Mono-sample Pb–Pb dating of pyrrhotite and tourmaline: Proterozoic vs Archean intracratonic gold mineralisation in Zimbabwe. *Geology* 24, 823–826.

Frey M, 1987. *Low Temperature Metamorphism*. Chapman and Hall, London.

Fuchs Y and Lagache M, 1994. La transformation chlorite-tourmaline en milieu hydrothermal, exemples naturels et approche experimentale. *Comptes Rendus de l'Académie des Sciences* 319, 907–913.

Fyfe WS, Price NJ and Thompson AB, 1978. *Fluids in the Earth's crust: Their significance in metamorphic, tectonic, and chemical transport processes*. Elsevier, Amsterdam.

Giles D, Betts P and Lister G, 2002. Far-field continental back-arc setting for the 1.80–1.67 Ga basins of northeastern Australia. *Geology* 30, 823–826.

Giles C and Just T, 2017. Copper-gold deposits of the Benagerie Ridge, Curnamona Province: in Phillips NP (editor). *'Australian Ore Deposits'. AusIMM Monograph* 32. Australasian Institute of Mining and Metallurgy, Melbourne, 647–650.

Gilmour P, 1976. Some transitional types of mineral deposits in volcanic and sedimentary rocks: in Wolf KH (editor). '*Handbook of strata-bound and stratiform ore deposits, Volume* 1'. Elsevier, 111–60.

Grainger D, 1967. Jervois Range copper and lead deposits. *Northern Territory Geological Survey Files, Alice Springs,* MBR/67/5.

Greene DC, 2010. Neoproterozoic rifting in the southern Georgina Basin, central Australia: implications for reconstructing Australia in Rodinia. *Tectonics* 29(5). TC5010, doi: 10.1029/2009TC002543.

Greenop R, Hain MP, Sosdian SM, Oliver KIC, Goodwin P, Chalk TB, Lear CH, Wilson PA and Foster GL, 2016. A record of Neogene seawater $D^{11}B$ reconstructed from paired $D^{11}B$ analyses on benthic and planktic foraminifera. *Climate of the Past* 13, 149-170.

Groves I and Plimer I, 2017. Broken Hill Pb-Zn-Ag deposit: in Phillips NP (editor). *'Australian Ore Deposits'. AusIMM Monograph* 32. Australasian Institute of Mining and Metallurgy, Melbourne, 641–646.

Hammerli J, Spandler C, Oliver NH, Sossi P and Dipple GM, 2015. Zn and Pb mobility during metamorphism of sedimentary rocks and potential implications for some base metal deposits. *Mineralium Deposita* 50, 657–664.

Hand M, Mawby J, Kinny P and Foden, J, 1999. U–Pb ages from the Harts Range, central Australia: evidence for early Ordovician extension and constraints on Carboniferous metamorphism. *Journal of the Geological Society, London* 156, 715–730.

Hawthorne FC and Henry DJ, 1999. Classification of the minerals of the tourmaline group. *European Journal of Mineralogy* 11, 201–215.

Hedstroem P, Simeonov L and Malmstrom L, 1989. The Zinkgruvan ore deposit, south-central Sweden; a Proterozoic, proximal Zn-Pb-Ag deposit in distal volcanic facies. *Economic Geology* 84, 1235–1261.

Heimann A, Spry PG, Teale GS, Conor CHH and Leyh WR, 2009. Geochemistry of garnet-rich rocks in the Southern Curnamona Province, Australia, and their genetic relationship to Broken Hill-type Pb-Zn-Ag mineralisation. *Economic Geology* 104, 687–712.

Helvaci C and Palmer MR, 2017. Origin and distribution of evaporite borates: the primary economic sources of boron. *Elements* 13, 249–254.

Henry DJ and Dutrow BL, 1996. Metamorphic tourmaline and its petrological implications. *Reviews in Mineralogy and Geochemistry* 33, 503–555.

Henry DJ, Novak M, Hawthorne FC, Ertl A, Dutrow BL, Uher P and Pezzotta F, 2011. Nomenclature of the tourmaline-supergroup minerals. *American Mineralogist* 96, 895–913.

Hoffman D, 1993. *Aspects of the geology, geochemistry and metamorphism of the lower orebody, Broken Hill deposit, Aggeneys*. MSc thesis, University of Cape Town, Cape Town.

Howlett D, Raimondo T and Hand M, 2015. Evidence for 1808–1770 Ma bimodal magmatism, sedimentation, high-temperature deformation and metamorphism in the Aileron Province, central Australia. *Australian Journal of Earth Sciences* 62, 831–852.

Hussey KJ, Huston DL and Claoué-Long JC, 2005. Geology and origin of some Cu-Pb-Zn (-Au-Ag) deposits in the Strangways Metamorphic Complex, Arunta Region, Northern Territory. *Northern Territory Geological Survey, Report* 17.

Huston DL, 1999. Stable isotopes and their significance for understanding the genesis of volcanic-hosted massive sulfide deposits: a review: in Barrie CT and Hannington MD (editors). *'Volcanic-associated massive sulfide deposits: processes and examples in modern and ancient settings'. Reviews in Economic Geology* 8, Society of Economic Geologists, 157–179.

Huston DL, Hussey K and Frater M, 2006a. Zinc-copper-lead metallogeny of the eastern Arunta: in Lyons P and Huston DL (editors). '*Evolution and metallogenesis of the North Australian Craton, Conference abstracts. NAPWRAP, 17–19'. Geoscience Australia, Record* 2006/16.

Huston DL, Maidment D, Hussey K and Frater M, 2006b. Iron oxide copper-gold deposits in the Tennant and Arunta regions: in Lyons P and Huston DL (editors). *Evolution and metallogenesis of the North Australian Craton, Conference Abstracts, NAPWRAP, 23–25.' Geoscience Australia, Record* 2006/16.

Huston DL, Maidment D and Hussey K, 2006c. Regional geology and metallogeny of the eastern Aileron and Irindina Provinces: a field guide. *Geoscience Australia, Record* 2006/13.

Huston DL, Stevens B, Southgate PN, Muhling P and Wyborn L, 2006d. Australian Zn-Pb-Ag ore-forming systems: a review and analysis. *Economic Geology* 101, 1117–1157.

Huston DL, Maas R, Cross A, Hussey KJ, Mernagh TP, Fraser G and Champion DC, 2016. The Nolans Bore rare-earth element-phosphorus-uranium mineral system: geology, origin and post-depositional modifications. *Mineralium Deposita* 51, 797–822.

Ishikawa T and Nakamura E, 1993. Boron isotope systematics of marine sediments. *Chemical Geology* 177, 567-580.

James RH, Rudnicki MD and Palmer MR, 1999. The alkali element and boron geochemistry of the Escanaba Trough sediment-hosted hydrothermal system. *Earth and Planetary Science Letters* 171, 157–169.

Jiang S-Y and Palmer MR, 1998. Boron isotope systematics of tourmaline from granites and pegmatites: a synthesis. *European Journal of Mineralogy* 10, 1253–1265.

Jiang S, 1998. Stable and radiogenic isotope studies of tourmaline: An overview. *Journal of the Czech Geological Society* 43, 75–90.

Jiang S-Y, Han F, Shen J and Palmer MR, 1999. Chemical and Rb–Sr, Sm–Nd isotopic systematics of tourmaline from the Dachang Sn-polymetallic ore deposit, Guangxi Province, PR China. *Chemical Geology* 157, 49–67.

Kamber BS, Freim R and Gibb AJ, 1998. Pitfalls and new approaches in granulite chronometry, an example from the Limpopo Belt, Zimbabwe. *Precambrian Research* 91, 269–285.

Kamber BS and Gladu AH, 2009. Comparison of Pb purification by anion-exchnage resins methods and assessment of long-term reproducibility of Th/U/Pb ratio measurements by quadrupole ICP–MS. *Geostandards and Geoanalytical Research* 33, 169–181.

Kampmann TC, Jansson NF, Stephens MB, Majka J and Lasskogen J, 2017. Systematics of hydrothermal alteration at the Falun base metal sulfide deposit and implications for ore genesis and exploration, Bergslagen Ore District, Fennoscandian Shield, Sweden. *Economic Geology* 112, 1111–1152.

Kim H, Cheong C and Cho M, 2007. The effect of allanite inclusions on U–Pb step-leaching ages and Sm–Nd isotope systematics of garnet from the Ogcheon metamorphic belt, South Korea. *Chemical Geology* 236, 27–41.

Kositcin N, Reno BL and Whelan JA, 2015. Summary of results. Joint NTGS–GA SHRIMP geochronology project: Arunta Region, July 2014–June 2015. *Northern Territory Geological Survey, Record* 2015−007.

Kruse PD, Dunster JN and Munson TJ, 2013. Chapter 28: Georgina Basin: in Ahmad M and Munson TJ (compilers). '*Geology and Mineral Resources of the Northern Territory'. Northern Territory Geological Survey, Special Publication* 5.

Laing WP, 1996. The Diamantina orogen linking the Willyama and Cloncurry terranes, eastern Australia. *University of Tasmania, Centre for Ore Deposit and Exploration Studies Special Publication* 1, 67–70.

Lal N, Parchad R and Nagpaul KK, 1977. Fission track etching and annealing of tourmaline. *Nuclear Track Detection* 1, 145–148.

Lambert-Smith JS, Rocholl A, Treloar PJ and Lawrence DM, 2016. Discriminating fluid source regions in orogenic gold deposits using B-isotopes. *Geochimica et Cosmochimica Acta* 194, 57–76.

Large RR, Bull SW, McGoldrick PJ and Walters S, 2005. Stratiform and stratabound Zn-Pb-Ag deposits in Proterozoic sedimentary basins, northern Australia. *Economic Geology 100th Anniversary Volume*, 931–963.

Leach DL, Sangster DF, Kelley KD, Large RR, Garven G, Allen CR, Gutzmer J and Walters S, 2005. Sediment-hosted zinc deposits: A global perspective. *Economic Geology 100th Anniversary Volume*, 561–608.

Leach DL, Bradley, DC, Huston D, Pisarevsky SA, Taylor RD and Gardoll SJ, 2010. Sediment-hosted lead-zinc deposits in earth history. *Economic Geology* 105, 593 –625.

Liu W and McPhail DC, 2005. Thermodynamic properties of copper chloride complexes and copper transport in magmatic-hydrothermal solutions. *Chemical Geology* 221, 21–39.

Lode S, Piercey SJ and Devine CA, 2015. Geology, mineralogy, and lithogeochemistry of metalliferous

mudstones associated with the Lemarchant volcanogenic massive sulfide deposit, Tally Pond Belt, Central Newfoundland. *Economic Geology* 110, 1835–1859.

Maas R, Grew ES and Carson CJ, 2015. Isotopic constraints (Pb, Rb–Sr, Sm–Nd) on the sources of Early Cambrian pegmatites with boron and beryllium minerals in the Larseman Hills, Prydz Bay, Antarctica. *The Canadian Mineralogist* 53, 249–272

Mackie AM, 1984. Geology of the Green Parrot and Marshall–Reward silver-lead deposits – Jervois Range, Northern Territory. *Proceedings Darwin Conference 1984. Australian Institute of Mining and Metallurgy Transactions*, 323–328.

Maidment DW, Hand M and Williams IS, 2005. Tectonic cycles in the Strangways Metamorphic Complex, Arunta Inlier, central Australia: geochronological evidence for exhumation and basin formation between two high-grade metamorphic events. *Australian Journal of Earth Sciences* 52, 205–215.

Marshall B and Spry PG, 2000. Discriminating between regional metamorphic remobilisation and syntectonic emplacement in the genesis of massive sulfide ores. *Reviews in Economic Geology* 11, 39–73.

Marschall HR, 2018. Chapter 8: Boron isotopes in the ocean floor realm and the mantle: in Marschall H and Foster G (editors). '*Boron isotopes. Advances in isotope geochemistry*'. Springer, 189–216.

Marschall HR and Jiang S-Y, 2011. Tourmaline isotopes: No element left behind. *Elements* 7, 313 –319.

Mayes K and Bennett M, 2017. The Rockface copper discovery at Jervois: in '*Annual Geoscience Exploration Seminar (AGES) Proceedings, Alice Springs, Northern Territory 28–29 March 2017*'. Northern Territory Geological Survey, Darwin.

McGloin MV, 2017. The significance of metaexhalites, seafloor alteration and retrograde processes for metamorphosed mineral deposits: examples of distinct alteration styles from the Aileron Province: in '*Annual Geoscience Exploration Seminar (AGES) Proceedings, Alice Springs, Northern Territory 28–29 March 2017*'. Northern Territory Geological Survey, Darwin.

McGloin MV and Bradey RS, 2017, Molyhil tungsten-molybdenum deposit: in Phillips NP (editor). '*Australian Ore Deposits'. AusIMM Monograph* 32. Australasian Institute of Mining and Metallurgy, Melbourne, 565–566.

McGloin MV and Weisheit A, 2015. Base metal and tungsten mineralisation in the Jervois Ranges and Bonya Hills: Characterisation, potential genetic models and exploration implications: in '*Annual Geoscience Exploration Seminar (AGES) 2015. Record of abstracts'. Northern Territory Geological Survey, Record* 2015−002.

McGloin MV and Weisheit A, in review. Epigenetic copper and tungsten mineralisation on Jinka and Jervois Range, northeastern Aileron Province. *Northern Territory Geological Survey, Record*.

McGloin MV, Weisheit A, Maas R and Creaser R, in prep. The geology and origin of copper-silver-lead-zinc sulfide deposits in the Jervois mineral field. *Northern Territory Geological Survey, Record*.

McGloin MV, Whelan JA, Reno BL, Beyer EE, Weisheit A, Meffre S, Thompson J and Zhukova I, 2017. Summary of results. NTGS LA–ICPMS geochronology project: Jervois mineral field, Bonya Hills and Jinka Plain, northeastern Aileron Province, Arunta Region, May 2014–Dec 2015. *Northern Territory Geological Survey, Record* 2017-006.

McGloin MV, Whelan JA, Reno BL, Beyer EE, Weisheit A, Thompson JM, Meffre S and Zhukova I, 2018. Summary of results. NTGS LA–ICP–MS geochronology project: Jervois mineral field, Bonya Hills and Jinka Plain in HUCKITTA, northeastern Aileron Province, May 2014–Dec 2015. *Northern Territory Geological Survey, Record* 2018-012.

McGoldrick PJ and Large RR, 1998. Proterozoic stratiform sediment-hosted Zn-Pb-Ag deposits. *AGSO Journal of Australian Geology and Geophysics* 17, 189–196.

Mercadier J, Richard A and Cathelineau M, 2012. Boron- and magnesium-rich marine brines at the origin of giant unconformity-related uranium deposits: $\delta^{11}B$ evidence from Mg-tourmalines. *Geology* 40, 231–234.

Mercier-Langevin P, McNicoll V, Allen RL, Blight JHS and Dube B, 2013. The Boliden gold-rich volcanogenic massive sulfide deposit, Skellefte district, Sweden: new U–Pb age constraints and implications at deposit and district scale. *Mineralium Deposita* 48, 485–504.

Meyer C, Wunder B, Meixner A, Romer RL and Heinrich W, 2008. Boron-isotope fractionation between tourmaline and fluid: an experimental re-investigation. *Contributions to Mineralogy and Petrology* 156, 259–267.

Morgan GB and London D, 1989. Experimental reactions of amphibolite with boron-bearing aqueous fluids at 200 MPa: implications for tourmaline stability and partial melting in mafic rocks. *Contributions to Mineralogy and Petrology* 102, 281–297.

Northern Territory Geological Survey, in prep. *Jinka, Northern Territory (First Edition). 1:100 000 geological map series, 6052*. Northern Territory Geological Survey, Darwin.

Oliver NHS, Butera KM, Rubenach MJ, Marshall LJ, Cleverley JS, Mark G, Tullemans F and Esser D, 2008. The protracted hydrothermal evolution of the Mount Isa Eastern Succession: a review and tectonic implications. *Precambrian Research* 163, 108–130.

Palmer MR and Slack JF, 1989. The boron isotopic composition of tourmaline from massive sulphide deposits and tourmalinites. *Contributions to Mineralogy and Petrology* 103, 403–451.

Palmer MR, Spivack AJ and Edmond JM, 1987. Temperature and pH controls over isotopic fractionation during adsorption of boron on marine clay. *Geochimica et Cosmochimica Acta* 51, 2319–2323.

Palmer MR, 1991. Boron isotope systematics of hydrothermal fluids and tourmalines: A synthesis. *Chemical Geology* 94, 111–121.

Parr JM and Plimer IR, 1993. Models for Broken Hill-type lead-zinc-silver deposits: in Kirkham RV, Sinclair WD, Thorpe RI and Duke JM (editors). '*Mineral deposit modelling'. Geological Association of Canada, Special Paper* 40, 253–288.

Perry EA, 1972. Diagenesis and the validity of the boron paleosalinity technique. *American Journal of Science* 272, 150–60.

Peters M, Kehrens P and van Gils H, 1985. *Geology and mineralisation of the Jervois Range, NT, Australia*. MSc Thesis, State University of Utrecht, The Netherlands.

Phillips GN and Powell R, 2010. Formation of gold deposits: a metamorphic devolitilization model. *Journal of Metamorphic Geology* 28, 689–718.

Plimer I, 1988. Tourmalinites associated with Australian Proterozoic submarine exhalative ores: in Freidrich GH and Herzig PM (editors). '*Base metal sulfide deposits in sedimentary and volcanic environments'*. Springer-Verlag, Berlin, 255–283.

Plimer I, 1994. Strata-bound scheelite in meta-evaporites, Broken Hill, Australia. *Economic Geology* 89, 423–437.

Raith JG, Riemer N and Meisel T, 2004. Boron metasomatism and behaviour of rare earth elements during formation of tourmaline rocks in the eastern Arunta Inlier, central Australia. *Contributions to Mineralogy and Petrology* 147, 91–109.

Ransom DM, 1978. The scheelite prospects of the Jervois Range, Bonya Creek and Molyhil areas. *Northern Territory Geological Survey, Open File Company Report* CR1978-0186.

Raveggi M, Giles D, Foden J, Meffre S, Nicholls I and Raetz M, 2015. Lead and Nd isotopic evidence for a crustal Pb source of the giant Broken Hill Pb–Zn–Ag deposit, New South Wales, Australia. *Ore Geology Reviews* 65, 228–244.

Reno BL, Whelan JA, Weisheit A, Kraus S, Beyer EE, Meffre S and Thompson J, 2016. Summary of results. NTGS laser ablation ICP-MS in situ monazite and xenotime geochronology project: Arunta Region, Jervois Range 1:100 000 mapsheet. *Northern Territory Geological Survey, Record* 2016-004.

Reno BL, Weisheit A, Beyer EE, Whelan JA and Kraus S, in review. *Jervois Range special Jervois Range–Tarlton, Northern Territory (First Edition). 1:100 000 geological map series, 6152*. Northern Territory Geological Survey, Darwin.

Reno BL, Weisheit A, Beyer EE, Whelan JA and McGloin M, 2017. Proterozoic tectonothermal evolution of the eastern Arunta Region, Central Australia: in '*Annual Geoscience Exploration Seminar (AGES) Proceedings, Alice Springs, Northern Territory 28–29 March 2017*'. Northern Territory Geological Survey, Darwin.

Ridler RH, 1971. Analysis of Archean volcanic basins in the Canadian Shield using the exhalite concept. *Bulletin of the Canadian Institute of Mining and Metallurgy* 64, 20.

Romer RL and Meixner A, 2014. Lithium and boron isotopic fractionation in sedimentary rocks during metamorphism – The role of rock composition and protolith mineralogy. *Geochimica et Cosmochimica Acta* 128, 158–177.

Romer RL, Meixner A and Hahne K, 2014. Lithium and boron isotopic composition of sedimentary rocks – The role of source history and depositional environment: A 250 Ma record from the Cadomian orogeny to the Variscan orogeny. *Gondwana Research* 26, 1093–1110.

Rudnick RL and Gao S, 2014. Volume 4.1 Composition of the Continental Crust: in Holland HD and Turekian KK (editors). '*Treatise on Geochemistry (Second Edition)*'. Elsevier Ltd, Oxford, 1–51.

Ryan PJ, Lawrence AL, Lipson RD, Moore JM, Patterson A, Stedman DP and Van Zyl D, 1986. The Aggeneys Base Metal Sulphide Deposits, Namaqualand, South Africa: in Anhaeusser CR and Maske S, (editors). *'Mineral Deposits of Southern Africa'. Geological Society of South Africa, Johannesburg* 2, 1447–1473.

Scrimgeour IR, 2013. Chapter 12: Aileron Province: in Ahmad M and Munson TJ (compilers). '*Geology and Mineral Resources of the Northern Territory'. Northern Territory Geological Survey, Special Publication* 5.

Shaw RD, Warren RG, Offe LA, Freeman MJ and Horsfall CL, 1984. Geology of Arunta Block in the southern part of the Huckitta 1:250 000 sheet area, central Australia - preliminary data, 1980 survey. Scale 1:250 000. *Bureau of Mineral Resources, Geology and Geophysics, Record* 1984/003.

Shaw RD, 1990. Arunta Block – regional geology and mineralisation: in Hughes FE (editor). '*Geology of the Mineral Deposits of Australia and Papua New Guinea*'. The Australian Institute of Mining and Metallurgy, Melbourne, 869–874.

Shnyukov EF, Naumenko PI, Lebedev Y.S, Usenko VP, Gordievich VA, Yukhanov IS and Shchiritsa AS, 1971. Mud volcanism and ore formation: Kiev, Naukova Dumka, 332 p. [in Russian].

Simon L, Lecuyer C, Marechal C and Coltice N, 2006. Modelling the geochemical cycle of boron: Implications for the long-term $D^{11}B$ evolution of seawater and oceanic crust. *Chemical Geology* 255, 61–76.

Skirrow RG and Ashley PM, 2000. Proterozoic Cu-Au systems of the Curnamona Province – members of a global family? *MESA Journal* 19, 48–50.

Slack JF, 1982. Tourmaline in Appalachian-Caledonian massive sulphide deposits and its exploration significance. *Transactions of the Institution of Mining and Metallurgy. Section B Applied Earth Science* 91, 81–89.

Slack JF, 1996. Tourmaline associations with hydrothermal ore deposits. *Reviews in Mineralogy* 33, 559–643.

Slack JF, 2002. Tourmaline associations with hydrothermal ore deposits: in Grew ES and Anovitz LM (editors). *'Boron: Mineralogy, petrology and geochemistry (second printing with corrections and additions)'. Reviews in Mineralogy* 33, 559–644.

Slack JF and Coad PR, 1989. Multiple hydrothermal and metamorphic events in the Kidd Creek volcanogenic massive sulphide deposit, Timmins, Ontario: Evidence from tourmalines and chlorites. *Canadian Journal of Earth Science* 26, 694–715.

Slack, JF and Trumbull R, 2011. Tourmaline as a recorder of ore forming processes. *Elements* 7, 321–326.

Slack JF and Stevens BPJ, 1994. Clastic metasediments of the Early Proterozoic Broken Hill Group, New South Wales, Australia: geochemistry, provenance, and metallogenic significance. *Geochimica et Cosmochimica Acta* 58, 3633–3652.

Slack JF, Herriman N, Barnes RG and Plimer IR, 1984. Stratiform tourmalinites in metamorphic terranes and their geologic significance. *Geology* 12, 713–716.

Slack JF, Palmer MR and Stevens BPJ, 1989. Boron isotope evidence for the involvement of non-marine evaporites in the origin of Broken Hill ore deposits. *Nature* 342, 913–916.

Slack JF, Palmer MR, Stevens BPJ and Barnes RG, 1993. Origin and significance of tourmaline-rich rocks in the Broken Hill district, Australia. *Economic Geology* 88, 505–541.

Slack JF, Shaw DR, Leitch CHB and Turner RJW, 2000. Tourmalinites and coticules from the Sullivan Pb-Zn-Ag deposit and vicinity, British Columbia: Geology, geochemistry and genesis: in Lydon JW (editor). *'Geological environment of the Sullivan deposit, British Columbia'. Geological Association of Canada, Mineral Deposit Division, Special Publication* 1.

Slack JF, Turner RJW and Ware P, 1998. Boron-rich mud volcanoes of the Black Sea region: modern analogues to ancient sea-floor tourmalinites associated with Sullivan-type Pb-Zn deposit? *Geology* 26, 439–442.

Smith MP and Yardley BWD, 1996. The boron isotopic composition of tourmaline as a guide to fluid processes in the southwestern England orefield: An ion microprobe study. *Geochimica et Cosmochimica Acta* 60, 1415–1427.

Smith BR, McGloin MV and Reno BL, 2016. *Garnet composition variations identified using HyLogger from Jervois, Arunta Region, Northern Territory, Australia*. AESC 2016 – Australian Earth Sciences Convention. Uncover Earth's Past to Discover Our Future, 26–30 June, Adelaide Convention Centre.

Spivack AJ and Edmond JM, 1987. Boron isotope exchange between seawater and the oceanic crust. *Geochimica et Cosmochimica Acta* 51, 1033–1043.

Spivack AJ, Palmer MR and Edmond JM, 1987. The sedimentary cycle of the boron isotopes. *Geochimica et Cosmochimica Acta* 51, 1939–1949.

Spry PG, 1990. Geochemistry and origin of coticules (spessartine-quartz rocks) associated with metamorphosed massive sulfide deposits: in Spry PG and Bryndzia LT (editors). '*Regional metamorphism of ore deposits and genetic implications*'. VSP, Utrecht, 49–75.

Spry PG, Peter JM and Slack JF, 2000. Meta-exhalites as exploration guides to ore. *Reviews in Economic Geology* 11, 163–202.

Spry PG, Teale GS and Steadman JA, 2009. *Classification of Broken Hill-type Pb-Zn-Ag deposits: a refinement*. American Geophysical Union, Spring Meeting, 2009, abstract #V21A–02.

Stacey JS and Kramers JD, 1975. Approximation of terrestrial lead isotope evolution by a two-stage model. *Earth and Planetary Science Letters* 26, 207–221.

Stanton RL, 1972. A preliminary account of the chemical relationships between sulfide lode and 'banded iron formation' at Broken Hill, New South Wales. *Economic Geology* 67, 1128–1145.

Steinmetz RL, 2017. Lithium- and boron-bearing brines in the Central Andes: exploring hydrofacies on the eastern Puna plateau between 23° and 23°30'S. *Mineralium Deposita* 52, 35–50.

Stevens BPJ, 2015. Magnetite-bearing zones in metasediments at Broken Hill, Australia: signatures of black smokers? *Australian Journal of Earth Sciences* 62, 605–624.

Stevens BPJ, Barnes RG, Brown RE, Stroud WJ and Willis IL, 1988. The Willyama Supergroup in the Broken Hill and Euriowie Blocks, New South Wales. *Precambrian Research* 40, 297–327.

Swihart GH, Moore B and Callis EL, 1986. Boron isotopic composition of marine and nonmarine evaporite borates. *Geochimica et Cosmochimica Acta* 50, 1297–1301.

Teale G, 1982. *Base metal mineralisation within low grade metamorphics of the Jervois Range, NE Arunta Block: a comparison with the Mine Sequence Suite of the Broken Hill area*. Marathon Petroleum Company Report.

Tomkins AG, 2007. Three mechanisms of ore re-mobilisation during amphibolite facies metamorphism at the Montauban Zn–Pb–Au–Ag deposit. *Mineralium Deposita* 42, 627–637.

Tomkins AG, 2013. On the source of orogenic gold. *Geology* 41, 1255–1256.

Trumbull RB and Slack JF, 2018. Chapter 10: Boron isotopes in the continental crust: granites, pegmatites, felsic volcanic rocks, and related ore deposits: in Marschall H and Foster G (editors). '*Boron isotopes. Advances in isotope geochemistry*'. Springer, 249–272.

van Hinsberg VJ, Henry DJ and Dutrow BL, 2011a. Tourmaline as a petrologic forensic mineral: A unique recorder of its geologic past. *Elements* 7, 327–332.

van Hinsberg VJ, Henry DJ and Marschall HR, 2011b. Tourmaline: an ideal indicator of its host environment. *The Canadian Mineralogist* 49, 1–16.

Vengosh A, Chivas AR, Starinsky A, Kolodny Y, Zhang B and Zhang P, 1995. Chemical and boron isotope compositions of non-marine brines from the Qaidam Bain, Qinghai, China. *Chemical Geology* 120, 135–154.

Vengosh A, Starinsky A, Kolodny Y, Chivas AR and Raab M, 1992. Boron isotope variations during fractional evaporation of seawater – new constraints on the marine vs nonmarine debate. *Geology* 20, 799–802.

Walters SJ, 1996. An overview of Broken Hill type deposits: in Pongratz J and Davidson GJ (editors). '*New developments in Broken Hill type deposits'*. CODES Special Publication 1. Centre for Ore Deposit and Exploration Studies, University of Tasmania, Hobart, Tasmania, 1–10.

Walters SJ, 1998. Broken Hill-type deposits. *AGSO Journal of Australian Geology and Geophysics* 17, 229–237.

Warren JK, 1996. Evaporites, brines and base metals: What is an evaporite? Defining the rock matrix. *Australian Journal of Earth Sciences* 43, 115–132.

Warren JK, 1997. Evaporites, brines and base metals: Fluids, flow and 'the evaporite that was'. *Australian Journal of Earth Sciences* 44, 149–183.

Warren JK, 2010, Evaporites through time: Tectonic, climatic and eustatic controls in marine and nonmarine deposits. *Earth-Science Reviews* 98, 217–268.

Warren JK, 2016. *Evaporites: a geological compendium*. Springer International Publishing, Switzerland.

Warren RG, Thorpe RI, Dean JA and Mortensen JK, 1995. Pb-isotope data from base-metal deposits in central Australia: implications for Proterozoic stratigraphic

correlations. *AGSO Journal of Australian Geology and Geophysics* 15, 501–509.

Weisheit A, Reno BL and Beyer EE, 2017. Proterozoic and Palaeozoic evolution of a crustal-scale shear zone system in the northeastern Aileron and Irindina provinces, central Australia: in Pearce, MA (compiler). *'Abstract Volume. Specialist Group in Tectonics and Structural Geology (SGTSG) Conference 8–12 November 2017, Denmark, WA, Australia'. Geological Survey of Western Australia, Record* 2017/17.

Weisheit A, Reno BL, Beyer EE, in review. *Jervois Range Special, Northern Territory. 1:100 000 geological map explanatory notes, 6152 and part 6252*. Northern Territory Geological Survey, Darwin.

Weisheit A, Reno B, Beyer EE and Whelan JA, 2015. *Pulses of progressive shearing and reactivated fault structures: The 1.5 b.y. Palaeoproterozoic to Palaeozoic structural and metamorphic evolution of eastern Arunta Region, central Australia*. Specialist Group in Tectonics and Structural Geology (SGTSG) Conference, 22–27 November 2015, Caloundra, QLD, Australia.

Weisheit A, Reno BL, Beyer EE, Whelan JA and McGloin M, 2016. Multiply reactivated crustal-scale structures and a long-lived counter-clockwise P-T path: New insights into the 1.5 billion year tectonothermal evolution of the eastern Arunta Region, central Australia: in '*Annual Geoscience Exploration Seminar (AGES) Proceedings, Alice Springs, Northern Territory 15–16 March 2016*'. Northern Territory Geological Survey, Darwin.

Whiting TH, 1986. Aeromagnetics as an aid to geological mapping-a case history from the Arunta Inlier, Northern Territory. *Australian Journal of Earth Sciences* 33, 271–286.

Wilkinson JJ, 2014. Volume 13.9: Sediment-hosted zinc lead mineralization: processes and perspectives: in Holland HD and Turekian KK (editors). '*Treatise on Geochemistry (Second Edition)*'. Elsevier Ltd, Oxford, 219–249.

Woodhead JD, 2002. A simple method for obtaining highly accurate Pb isotope data by MC–ICP–MS. *Journal of Analytical Atomic Spectrometry* 17, 1–6.

Xavier RP, Wiedenbeck M, Trumbull RB, Dreher AM, Monteiro LVS, Rhede D, de Araújo CEG and Torresi I, 2008. Tourmaline B-isotopes fingerprint marine evaporites as the source of high salinity ore fluids in iron oxide-copper gold deposits, Carajás mineral province (Brazil). *Geology* 36, 743–746.

Xiao J, Xiao YK, Jin ZD, He MY and Liu CQ, 2013. Boron isotope variations and its geochemical application in nature. *Australian Journal of Earth Sciences* 60, 431–447.

Yardley BWD, 2005. Metal concentrations in crustal fluids and their relationship to ore formation. *Economic Geology Special 100th Anniversary Volume*, 613–632.

You C-F, Chan LH, Spivack AJ and Gieskes JM, 1995. Lithium, boron and their isotopes in sediments and pore waters of Ocean Drilling Program Site 808, Nankai Trough: Implications for fluid expulsion in accretionary prisms. *Geology* 23, 37–40.

Ypma PJ, 1983. Annual report due 2 April 1983 for exploration areas EL 3165, EL3202, EL3203, EL3204 and EL3301, Plenty River Mining Company. *Northern Territory Geological Survey, Open File Company Report* CR1983-0093.

Ypma PJ, 1985. Exploration report on EL3301, EL3202, EL3203 and EL3204 for the period 1 April 1984 to 1 June 1985. Plenty River Mining Company NL. *Northern Territory Geological Survey, Open File Company Report* CR1985/125.

Ypma PJ, 1986. Final report on exploration activities over the period 25 June 1982 to 30 June 1986, Plenty River Mining Company. *Northern Territory Geological Survey, Open File Company Report* CR1986-0235.

Ypma PJ, 1991. Annual report Jervois Range 6 December 1989 to 7 December 1990, Plenty River Mining Company. *Northern Territory Geological Survey, Open File Company Report* CR1991-0132.

Ypma PJ, De Boorder H, Van Gils H, Kehrens P, Ormsby W and Peters M, 1984. *Geology and mineralisation of the Jervois Range, NT. Proceedings Darwin Conference 1984*. Australian Institute of Mining and Metallurgy Transactions, 319–321.

Zhao J-X and McCulloch MT, 1995. Geochemical and Nd isotopic systematics of granites from the Arunta Inlier, central Australia: implications for Proterozoic crustal evolution. *Precambrian Research* 71, 265–299.

Appendix Table 1. EMP average analyses of major element compositions in tourmaline. Data reported as oxi

Point	Sample	Analysis position	SiO_2	Al_2O_3	TiO_2	FeO
#14	HU14MVM130-1_1	core	35,89	30,78	0,52	10,70
#15	*HU14MVM130-2_2*	*rim*	*35,54*	*31,64*	*0,32*	*8,57*
#16	HU14MVM130-3_3	core	35,59	31,29	0,18	8,01
#17	HU14MVM130-4_4	core	36,21	32,14	0,22	10,09
#18	*HU14MVM130-5_5*	*rim*	*36,43*	*31,69*	*0,44*	*8,59*
#19	HU14MVM130-6_6	core	35,94	30,02	0,57	9,80
#20	HU14MVM130-7_7	core	35,93	30,83	0,71	9,88
#21	HU14MVM130-8_8	core	35,86	31,29	0,40	9,50
#22	HU14MVM130-9_9	core	35,86	31,44	0,35	9,80
#23	HU14MVM130-10_10	core	36,05	31,92	0,27	10,04
#24	HU14MVM130-11_11	core	36,46	32,63	0,28	10,45
#25	HU14MVM130-12_12	core	35,87	31,55	0,34	9,68
#26	HU14MVM130-13_13	core	36,12	31,30	0,40	11,08
#27	HU14MVM130-14_14	core	35,81	32,50	0,29	7,73
#28	*HU14MVM130-15_15*	*rim*	*36,32*	*31,69*	*0,33*	*9,65*
#29	HU14MVM130-16_16	core	36,42	31,78	0,47	9,16
#30	HU14MVM130-17_17	core	35,59	31,18	0,42	10,01
#31	HU14MVM130-18_18	core	36,64	31,31	0,71	9,66
#32	HU14MVM130-19_19	core	35,42	31,30	0,46	9,77
#33	HU14MVM130-20_20	core	36,63	32,42	0,22	10,22
		rim mean	**36,10**	**31,67**	**0,36**	**8,94**
		core mean	**36,02**	**31,51**	**0,40**	**9,74**
#34	HU14MVM147-1_1	core	35,91	33,96	0,18	10,41
#35	HU14MVM147-2_2	core	35,79	33,88	0,16	10,17
#36	*HU14MVM147-3_3*	*rim*	*36,58*	*34,07*	*0,13*	*10,17*
#37	HU14MVM147-4_4	core	35,71	33,83	0,17	10,17
#38	HU14MVM147-5_5	core	35,94	33,84	0,25	9,38
#39	*HU14MVM147-6_6*	*rim*	*35,75*	*34,52*	*0,14*	*10,05*
#40	HU14MVM147-7_7	core	35,73	34,50	0,18	10,10
#41	HU14MVM147-8_8	core	35,93	34,02	0,13	10,26
#42	*HU14MVM147-9_9*	*rim*	*36,32*	*30,12*	*0,43*	*10,37*
#43	HU14MVM147-10_10	core	35,91	33,96	0,30	9,38
#44	HU14MVM147-11_11	core	35,97	33,74	0,14	9,99
#45	HU14MVM147-12_12	core	35,67	33,66	0,45	9,76
#46	HU14MVM147-13_13	core	36,07	33,66	0,35	9,33
#47	HU14MVM147-14_14	core	35,93	33,82	0,16	10,42
#48	HU14MVM147-15_15	core	36,14	33,97	0,15	10,15
#49	HU14MVM147-16_16	core	36,26	33,87	0,17	10,24
#50	HU14MVM147-17_17	core	36,11	30,82	0,30	10,85
#51	HU14MVM147-18_18	core	36,18	33,57	0,17	10,29
#52	HU14MVM147-19_19	core	35,63	34,22	0,12	9,61
#53	*HU14MVM147-20_20*	*rim*	*35,70*	*34,81*	*0,11*	*9,75*
		rim (mean)	**36,09**	**33,38**	**0,20**	**10,09**
		core (rim)	**35,93**	**33,71**	**0,21**	**10,03**
#54	HU14MVM132 -1_1	core	36,91	31,63	0,31	8,41
#55	HU14MVM132 -2_2	core	36,76	31,51	0,31	8,30
#56	HU14MVM132 -3_3	core	36,31	31,62	0,26	8,00
#57	HU14MVM132 -4_4	core	36,45	31,38	0,30	10,56
#58	HU14MVM132 -5_5	core	37,14	32,88	0,28	7,51
#59	HU14MVM132 -6_6	core	36,32	31,02	0,30	10,33
#60	HU14MVM132 -7_7	core	36,38	31,30	0,28	10,22
#61	HU14MVM132 -8_8	core	36,61	32,01	0,35	12,12

#62	HU14MVM132 -9_9	core	36,85	31,03	0,83	8,23
#63	*HU14MVM132 -10_10*	*rim*	*36,27*	*31,41*	*0,38*	*10,01*
#64	HU14MVM132 -11_11	core	36,39	31,52	0,30	8,20
#65	HU14MVM132 -12_12	core	35,74	31,19	0,27	10,34
#66	HU14MVM132 -13_13	core	36,55	30,58	0,53	9,87
#67	HU14MVM132 -14_14	core	36,57	31,23	0,28	10,15
#68	HU14MVM132 -15_15	core	36,42	30,98	0,37	9,34
#69	HU14MVM132 -16_16	core	36,59	31,40	0,34	9,19
#70	HU14MVM132 -17_17	core	36,27	31,38	0,27	9,71
#71	*HU14MVM132 -18_18*	*rim*	*36,48*	*31,44*	*0,27*	*9,56*
#72	HU14MVM132 -19_19	core	36,53	31,21	0,46	9,22
#73	*HU14MVM132 -20_20*	*rim*	*35,86*	*31,46*	*0,29*	*8,38*
#13	HU14MVM132 -21_21	core	35,06	29,60	0,23	14,13
		rim (mean)	36,20	31,44	0,31	9,32
		core (mean)	36,44	31,30	0,35	9,66
#76	HU14MVM129-1_1	core	36,03	31,87	0,33	9,94
#77	HU14MVM129-2_2	core	36,38	32,06	0,33	9,97
#78	HU14MVM129-3_3	core	36,36	31,88	0,37	9,86
#79	HU14MVM129-4_4	core	36,70	31,75	0,33	10,11
#80	HU14MVM129-5_5	core	36,41	32,28	0,33	10,07
#81	HU14MVM129-6_6	core	36,56	31,62	0,32	9,71
#82	*HU14MVM129-7_7*	*rim*	*36,50*	*32,30*	*0,33*	*9,95*
#83	HU14MVM129-8_8	core	36,46	31,17	0,56	9,74
#84	HU14MVM129-9_9	core	36,13	32,92	0,46	7,64
#85	HU14MVM129-10_10	core	36,32	32,27	0,31	11,99
#86	HU14MVM129-11_11	core	36,43	31,82	0,30	9,96
#87	HU14MVM129-12_12	core	36,36	31,86	0,37	10,15
#88	HU14MVM129-13_13	core	36,49	31,79	0,28	9,99
#89	*HU14MVM129-14_14*	*rim*	*36,50*	*31,52*	*0,31*	*10,29*
#90	HU14MVM129-15_15	core	36,13	31,99	0,41	11,73
#91	*HU14MVM129-16_16*	*rim*	*36,01*	*31,80*	*0,34*	*10,90*
#92	HU14MVM129-17_17	core	36,31	32,02	0,33	11,71
#93	*HU14MVM129-18_18*	*rim*	*36,48*	*31,89*	*0,32*	*9,67*
#94	HU14MVM129-19_19	core	36,60	31,17	0,35	10,53
#95	HU14MVM129-20_20	core	36,19	32,55	0,25	12,01
		rim (mean)	**36,37**	**31,88**	**0,33**	**10,20**
		core (mean)	**36,37**	**31,94**	**0,35**	**10,32**
#96	HU14MVM133-1_1	core	36,61	33,94	0,12	9,98
#97	*HU14MVM133-2_2*	*rim*	*36,48*	*31,73*	*0,29*	*10,29*
#98	HU14MVM133-3_3	core	36,41	31,96	0,32	11,14
#99	*HU14MVM133-4_4*	*rim*	*35,98*	*32,43*	*0,42*	*12,12*
#100	HU14MVM133-5_5	core	36,05	31,33	0,29	11,21
#101	*HU14MVM133-6_6*	*rim*	*35,50*	*31,94*	*0,40*	*12,68*
#102	HU14MVM133-7_7	core	36,35	32,78	0,17	9,77
#104	HU14MVM133-9_9	core	36,13	33,18	0,29	12,82
#105	*HU14MVM133-10_10*	*rim*	*36,16*	*33,33*	*0,33*	*12,61*
#106	HU14MVM133-11_11	core	35,78	30,80	0,34	10,50
#107	HU14MVM133-12_12	core	36,79	31,55	0,27	7,66
#108	HU14MVM133-13_13	core	35,66	33,29	0,26	13,24
#109	HU14MVM133-14_14	core	35,66	31,70	0,40	14,30
#110	*HU14MVM133-15_15*	*rim*	*36,49*	*31,26*	*0,30*	*7,99*
#111	HU14MVM133-16_16	core	36,29	32,15	0,31	9,35
#112	HU14MVM133-17_17	core	35,71	31,69	0,38	13,63
#113	HU14MVM133-18_18	core	36,46	30,99	0,24	9,84

#114	HU14MVM133-19_19	core	36,62	31,78	0,33	9,26
#115	HU14MVM133-20_20	core	36,18	32,17	0,28	10,67
#116	HU14MVM133-21_21	core	35,91	31,48	0,37	13,76
#117	HU14MVM133-22_22	core	36,41	30,90	0,34	10,72
		rim (mean)	36,12	32,14	0,35	11,14
		core (mean)	36,19	31,98	0,29	11,12

de weight percent.

MnO	MgO	Cr_2O_3	CaO	Na_2O	K_2O	B_2O_3	Sum Oxide%	B
0,06	6,13	0,00	0,94	2,13	0,04	10,51	101,34	3,00
0,07	*6,81*	*0,02*	*1,07*	*1,87*	*0,02*	*10,49*	*100,03*	*3,00*
0,06	7,40	0,06	1,05	1,87	0,03	10,47	99,63	3,00
0,04	5,80	0,01	0,72	1,97	0,04	10,60	101,51	3,00
0,05	*7,21*	*0,00*	*1,22*	*1,92*	*0,04*	*10,69*	*101,96*	*3,00*
0,09	7,30	0,01	1,43	1,86	0,03	10,52	101,20	3,00
0,04	6,54	0,00	0,93	1,97	0,03	10,53	101,03	3,00
0,04	6,74	0,00	1,17	1,97	0,04	10,56	101,21	3,00
0,08	6,32	0,00	0,91	1,98	0,01	10,53	100,93	3,00
0,10	6,00	0,01	0,76	1,94	0,02	10,57	101,33	3,00
0,07	4,99	0,00	0,47	1,79	0,03	10,61	101,44	3,00
0,05	6,48	0,00	0,82	2,02	0,04	10,55	101,04	3,00
0,08	5,91	0,01	0,92	1,99	0,03	10,59	102,10	3,00
0,09	6,79	0,00	1,21	1,68	0,02	10,58	100,35	3,00
0,08	*6,21*	*0,00*	*0,86*	*2,04*	*0,02*	*10,60*	*101,46*	*3,00*
0,05	6,75	0,02	0,88	2,04	0,01	10,67	101,92	3,00
0,05	6,08	0,00	0,98	1,95	0,04	10,46	100,37	3,00
0,07	6,39	0,00	0,83	1,95	0,03	10,65	101,92	3,00
0,02	6,50	0,01	1,09	1,93	0,03	10,48	100,61	3,00
0,05	5,11	0,02	0,41	1,80	0,03	10,59	101,13	3,00
0,07	**6,74**	**0,01**	**1,05**	**1,94**	**0,03**	**10,59**		
0,06	**6,31**	**0,01**	**0,91**	**1,93**	**0,03**	**10,56**		
0,54	4,19	0,01	0,42	2,00	0,06	10,64	101,99	3,00
0,53	4,02	0,00	0,35	1,89	0,05	10,56	101,05	3,00
0,51	*4,30*	*0,00*	*0,43*	*2,00*	*0,06*	*10,74*	*102,69*	*3,00*
0,51	4,23	0,01	0,45	1,94	0,06	10,58	101,30	3,00
0,19	5,35	0,00	0,93	1,72	0,06	10,70	102,06	3,00
0,65	*3,92*	*0,00*	*0,41*	*1,84*	*0,05*	*10,63*	*101,63*	*3,00*
0,64	3,95	0,00	0,37	1,89	0,03	10,63	101,69	3,00
0,61	4,06	0,00	0,39	1,91	0,07	10,62	101,65	3,00
0,13	*6,28*	*0,01*	*1,04*	*1,99*	*0,04*	*10,48*	*100,84*	*3,00*
0,11	5,18	0,00	0,77	1,79	0,07	10,68	101,83	3,00
0,54	4,30	0,01	0,38	1,92	0,04	10,59	101,28	3,00
0,15	4,89	0,01	0,85	1,64	0,05	10,62	101,42	3,00
0,12	5,47	0,02	0,92	1,69	0,04	10,70	102,06	3,00
0,38	4,29	0,01	0,41	1,92	0,05	10,62	101,66	3,00
0,49	4,21	0,00	0,37	1,92	0,06	10,64	101,77	3,00
0,50	4,42	0,00	0,39	1,96	0,04	10,68	102,22	3,00
0,11	6,06	0,00	1,06	2,04	0,04	10,53	101,55	3,00
0,41	4,46	0,00	0,40	1,96	0,06	10,64	101,82	3,00
0,59	3,89	0,01	0,34	1,78	0,06	10,53	100,42	3,00
0,57	*3,96*	*0,04*	*0,37*	*1,76*	*0,07*	*10,63*	*101,44*	*3,00*
0,47	**4,62**	**0,01**	**0,56**	**1,90**	**0,06**	**10,62**		
0,40	**4,56**	**0,01**	**0,55**	**1,87**	**0,05**	**10,62**		
0,06	7,36	0,00	0,61	2,34	0,02	10,73	102,10	3,00
0,08	7,27	0,01	0,65	2,28	0,01	10,67	101,52	3,00
0,11	7,34	0,02	0,66	2,30	0,01	10,61	100,91	3,00
0,19	5,99	0,01	0,35	2,38	0,03	10,60	101,89	3,00
0,07	6,93	0,00	0,37	2,02	0,01	10,77	101,70	3,00
0,13	5,96	0,00	0,16	2,56	0,02	10,51	100,93	3,00
0,17	6,02	0,03	0,17	2,47	0,02	10,56	101,25	3,00
0,17	4,29	0,00	0,07	2,37	0,05	10,60	102,31	3,00

0,08	7,48	0,00	0,50	2,29	0,01	10,69	101,68	3,00
0,17	*6,30*	*0,02*	*0,47*	*2,36*	*0,03*	*10,60*	*101,67*	*3,00*
0,11	7,22	0,00	0,61	2,25	0,02	10,61	100,89	3,00
0,18	5,71	0,04	0,17	2,45	0,02	10,43	100,14	3,00
0,13	6,66	0,02	0,47	2,50	0,02	10,59	101,57	3,00
0,15	6,44	0,00	0,24	2,53	0,03	10,62	101,90	3,00
0,15	6,65	0,01	0,39	2,44	0,02	10,56	100,97	3,00
0,13	6,70	0,00	0,50	2,40	0,01	10,63	101,56	3,00
0,13	6,08	0,00	0,25	2,38	0,04	10,52	100,65	3,00
0,20	*6,26*	*0,00*	*0,35*	*2,47*	*0,03*	*10,59*	*101,29*	*3,00*
0,13	6,70	0,02	0,52	2,34	0,03	10,61	101,43	3,00
0,11	*7,03*	*0,10*	*0,60*	*2,26*	*0,03*	*10,52*	*100,27*	*3,00*
0,14	5,37	0,26	0,12	1,88	0,04	10,29	100,67	3,00
0,16	6,53	0,04	0,47	2,36	0,03	10,57		
0,13	6,45	0,02	0,38	2,34	0,02	10,59		
0,11	5,68	0,02	0,21	2,19	0,04	10,51	100,56	3,00
0,07	5,80	0,00	0,25	2,24	0,04	10,60	101,41	3,00
0,14	5,80	0,00	0,29	2,20	0,04	10,58	101,16	3,00
0,13	5,57	0,04	0,21	2,23	0,04	10,59	101,35	3,00
0,08	5,71	0,02	0,15	2,29	0,03	10,63	101,67	3,00
0,12	6,01	0,01	0,32	2,27	0,04	10,59	101,22	3,00
0,09	*5,55*	*0,03*	*0,35*	*2,09*	*0,04*	*10,62*	*101,53*	*3,00*
0,05	6,12	0,06	0,22	2,28	0,04	10,55	100,89	3,00
0,04	6,59	0,03	1,19	1,56	0,03	10,66	100,91	3,00
0,07	3,87	0,06	0,11	1,98	0,02	10,51	101,13	3,00
0,07	5,58	0,03	0,17	2,26	0,03	10,55	100,84	3,00
0,08	5,53	0,00	0,18	2,20	0,02	10,55	100,94	3,00
0,09	5,73	0,01	0,17	2,18	0,03	10,56	100,96	3,00
0,09	*5,83*	*0,21*	*0,19*	*2,32*	*0,06*	*10,59*	*101,56*	*3,00*
0,08	4,26	0,03	0,12	2,11	0,04	10,49	101,02	3,00
0,08	*4,84*	*0,02*	*0,11*	*2,28*	*0,03*	*10,47*	*100,49*	*3,00*
0,12	4,51	0,06	0,14	2,17	0,03	10,55	101,56	3,00
0,10	*5,75*	*0,01*	*0,24*	*2,21*	*0,03*	*10,57*	*100,92*	*3,00*
0,12	5,74	0,00	0,20	2,25	0,14	10,56	101,31	3,00
0,06	3,68	0,01	0,06	1,88	0,03	10,48	100,83	3,00
0,09	**5,49**	**0,07**	**0,22**	**2,23**	**0,04**	**10,56**		
0,09	**5,39**	**0,02**	**0,25**	**2,14**	**0,04**	**10,56**		
0,12	4,04	0,00	0,04	1,83	0,02	10,62	100,99	3,00
0,14	*5,54*	*0,01*	*0,11*	*2,43*	*0,02*	*10,57*	*101,23*	*3,00*
0,14	4,80	0,00	0,13	2,38	0,03	10,56	101,51	3,00
0,12	*3,72*	*0,00*	*0,17*	*2,06*	*0,00*	*10,49*	*101,13*	*3,00*
0,17	4,94	0,01	0,12	2,43	0,03	10,45	100,62	3,00
0,11	*3,33*	*0,03*	*0,05*	*2,20*	*0,02*	*10,35*	*100,19*	*3,00*
0,19	4,79	0,00	0,18	1,96	0,01	10,53	100,36	3,00
0,22	2,31	0,00	0,03	1,68	0,01	10,45	100,73	3,00
0,16	*2,75*	*0,01*	*0,06*	*1,78*	*0,02*	*10,52*	*101,36*	*3,00*
0,17	5,49	0,00	0,44	2,20	0,05	10,38	99,72	3,00
0,16	7,44	0,00	0,70	2,23	0,02	10,66	101,16	3,00
0,16	2,72	0,01	0,03	1,80	0,01	10,47	101,25	3,00
0,17	2,42	0,00	0,04	2,12	0,03	10,34	100,77	3,00
0,18	*7,03*	*0,00*	*0,59*	*2,22*	*0,04*	*10,56*	*100,30*	*3,00*
0,18	5,77	0,00	0,18	2,37	0,03	10,57	100,83	3,00
0,21	2,87	0,02	0,05	2,05	0,02	10,35	100,55	3,00
0,16	5,88	0,00	0,17	2,36	0,06	10,48	100,25	3,00

0,15	6,11	0,00	0,51	2,31	0,02	10,62	101,38	3,00
0,08	4,98	0,01	0,09	2,36	0,03	10,53	101,01	3,00
0,18	3,13	0,00	0,09	2,14	0,04	10,40	101,09	3,00
0,17	5,45	0,00	0,11	2,52	0,02	10,48	100,73	3,00
0,14	4,47	0,01	0,20	2,14	0,02	10,50		
0,16	4,57	0,00	0,18	2,17	0,03	10,49		

Si	Al T-site	Al Z-site	Al Y-site	Al_{tot}	Cr	Ti	Fe	Mn
5,93	0,07	5,93	0,00	6,00	0,00	0,07	1,48	0,01
5,89	*0,11*	*6,00*	*0,07*	*6,18*	*0,00*	*0,04*	*1,19*	*0,01*
5,91	0,09	6,00	0,03	6,12	0,01	0,02	1,11	0,01
5,94	0,06	6,00	0,15	6,21	0,00	0,03	1,38	0,01
5,92	*0,08*	*6,00*	*0,00*	*6,07*	*0,00*	*0,05*	*1,17*	*0,01*
5,94	0,06	5,78	0,00	5,84	0,00	0,07	1,35	0,01
5,93	0,07	5,93	0,00	6,00	0,00	0,09	1,36	0,01
5,90	0,10	5,97	0,00	6,07	0,00	0,05	1,31	0,01
5,92	0,08	6,00	0,04	6,12	0,00	0,04	1,35	0,01
5,92	0,08	6,00	0,11	6,18	0,00	0,03	1,38	0,01
5,97	0,03	6,00	0,28	6,30	0,00	0,04	1,43	0,01
5,91	0,09	6,00	0,04	6,13	0,00	0,04	1,33	0,01
5,93	0,07	5,98	0,00	6,06	0,00	0,05	1,52	0,01
5,88	0,12	6,00	0,18	6,29	0,00	0,04	1,06	0,01
5,95	*0,05*	*6,00*	*0,08*	*6,12*	*0,00*	*0,04*	*1,32*	*0,01*
5,93	0,07	6,00	0,03	6,10	0,00	0,06	1,25	0,01
5,92	0,08	6,00	0,03	6,11	0,00	0,05	1,39	0,01
5,98	0,02	6,00	0,00	6,02	0,00	0,09	1,32	0,01
5,87	0,13	5,99	0,00	6,12	0,00	0,06	1,36	0,00
6,01	0,00	6,00	0,27	6,27	0,00	0,03	1,40	0,01
5,87	0,13	6,00	0,41	6,54	0,00	0,02	1,42	0,07
5,89	0,11	6,00	0,46	6,57	0,00	0,02	1,40	0,07
5,92	*0,08*	*6,00*	*0,42*	*6,50*	*0,00*	*0,02*	*1,38*	*0,07*
5,87	0,13	6,00	0,42	6,55	0,00	0,02	1,40	0,07
5,84	0,16	6,00	0,32	6,48	0,00	0,03	1,28	0,03
5,85	*0,15*	*6,00*	*0,50*	*6,66*	*0,00*	*0,02*	*1,38*	*0,09*
5,84	0,16	6,00	0,49	6,65	0,00	0,02	1,38	0,09
5,88	0,12	6,00	0,45	6,56	0,00	0,02	1,41	0,08
6,02	*0,00*	*5,89*	*0,00*	*5,89*	*0,00*	*0,05*	*1,44*	*0,02*
5,84	0,16	6,00	0,36	6,51	0,00	0,04	1,28	0,02
5,90	0,10	6,00	0,43	6,52	0,00	0,02	1,37	0,08
5,84	0,16	6,00	0,34	6,50	0,00	0,06	1,34	0,02
5,86	0,14	6,00	0,30	6,44	0,00	0,04	1,27	0,02
5,88	0,12	6,00	0,41	6,53	0,00	0,02	1,43	0,05
5,90	0,10	6,00	0,44	6,54	0,00	0,02	1,39	0,07
5,90	0,10	6,00	0,40	6,49	0,00	0,02	1,39	0,07
5,96	0,04	5,95	0,00	5,99	0,00	0,04	1,50	0,02
5,91	0,09	6,00	0,38	6,47	0,00	0,02	1,41	0,06
5,88	0,12	6,00	0,54	6,66	0,00	0,02	1,33	0,08
5,84	*0,16*	*6,00*	*0,55*	*6,71*	*0,01*	*0,01*	*1,33*	*0,08*
5,98	0,02	6,00	0,02	6,04	0,00	0,04	1,14	0,01
5,99	0,01	6,00	0,03	6,05	0,00	0,04	1,13	0,01
5,95	0,05	6,00	0,05	6,10	0,00	0,03	1,10	0,02
5,98	0,02	6,00	0,04	6,06	0,00	0,04	1,45	0,03
5,99	0,01	6,00	0,24	6,25	0,00	0,03	1,01	0,01
6,00	0,00	6,00	0,04	6,04	0,00	0,04	1,43	0,02
5,99	0,01	6,00	0,07	6,07	0,00	0,03	1,41	0,02
6,00	0,00	6,00	0,19	6,19	0,00	0,04	1,66	0,02

5,99	0,01	5,94	0,00	5,95	0,00	0,10	1,12	0,01
5,95	*0,05*	*6,00*	*0,02*	*6,07*	*0,00*	*0,05*	*1,37*	*0,02*
5,96	0,04	6,00	0,05	6,09	0,00	0,04	1,12	0,02
5,96	0,04	6,00	0,09	6,13	0,01	0,03	1,44	0,03
6,00	0,00	5,92	0,00	5,92	0,00	0,07	1,36	0,02
5,98	0,02	6,00	0,01	6,02	0,00	0,04	1,39	0,02
6,00	0,00	6,00	0,01	6,01	0,00	0,05	1,29	0,02
5,98	0,02	6,00	0,03	6,05	0,00	0,04	1,26	0,02
5,99	0,01	6,00	0,10	6,11	0,00	0,03	1,34	0,02
5,99	*0,01*	*6,00*	*0,07*	*6,08*	*0,00*	*0,03*	*1,31*	*0,03*
5,98	0,02	6,00	0,01	6,02	0,00	0,06	1,26	0,02
5,92	*0,08*	*6,00*	*0,05*	*6,13*	*0,01*	*0,04*	*1,16*	*0,02*
5,92	0,08	5,82	0,00	5,89	0,03	0,03	2,00	0,02

5,96	0,04	6,00	0,17	6,21	0,00	0,04	1,37	0,02
5,96	0,04	6,00	0,16	6,20	0,00	0,04	1,37	0,01
5,98	0,03	6,00	0,15	6,17	0,00	0,05	1,36	0,02
6,02	0,00	6,00	0,14	6,14	0,01	0,04	1,39	0,02
5,96	0,05	6,00	0,18	6,22	0,00	0,04	1,38	0,01
6,00	0,00	6,00	0,12	6,12	0,00	0,04	1,33	0,02
5,97	*0,03*	*6,00*	*0,20*	*6,23*	*0,00*	*0,04*	*1,36*	*0,01*
6,01	0,00	6,00	0,05	6,05	0,01	0,07	1,34	0,01
5,89	0,11	6,00	0,22	6,33	0,00	0,06	1,04	0,01
6,01	0,00	6,00	0,29	6,29	0,01	0,04	1,66	0,01
6,00	0,00	6,00	0,18	6,18	0,00	0,04	1,37	0,01
5,99	0,01	6,00	0,17	6,18	0,00	0,05	1,40	0,01
6,01	0,00	6,00	0,17	6,17	0,00	0,03	1,38	0,01
5,99	*0,01*	*6,00*	*0,09*	*6,10*	*0,03*	*0,04*	*1,41*	*0,01*
5,99	0,02	6,00	0,23	6,25	0,00	0,05	1,63	0,01
5,98	*0,02*	*6,00*	*0,21*	*6,22*	*0,00*	*0,04*	*1,51*	*0,01*
5,98	0,02	6,00	0,20	6,22	0,01	0,04	1,61	0,02
6,00	*0,00*	*6,00*	*0,18*	*6,18*	*0,00*	*0,04*	*1,33*	*0,01*
6,03	0,00	6,00	0,05	6,05	0,00	0,04	1,45	0,02
6,00	0,00	6,00	0,36	6,36	0,00	0,03	1,66	0,01

5,99	0,01	6,00	0,54	6,55	0,00	0,02	1,37	0,02
6,00	*0,00*	*6,00*	*0,15*	*6,15*	*0,00*	*0,04*	*1,42*	*0,02*
5,99	0,01	6,00	0,19	6,20	0,00	0,04	1,53	0,02
5,96	*0,04*	*6,00*	*0,29*	*6,33*	*0,00*	*0,05*	*1,68*	*0,02*
6,00	0,01	6,00	0,14	6,14	0,00	0,04	1,56	0,02
5,96	*0,04*	*6,00*	*0,28*	*6,32*	*0,00*	*0,05*	*1,78*	*0,02*
6,00	0,00	6,00	0,37	6,38	0,00	0,02	1,35	0,03
6,01	0,00	6,00	0,50	6,50	0,00	0,04	1,78	0,03
5,97	*0,03*	*6,00*	*0,46*	*6,49*	*0,00*	*0,04*	*1,74*	*0,02*
5,99	0,01	6,00	0,07	6,08	0,00	0,04	1,47	0,03
6,00	0,00	6,00	0,06	6,06	0,00	0,03	1,04	0,02
5,92	0,08	6,00	0,43	6,51	0,00	0,03	1,84	0,02
5,99	0,01	6,00	0,27	6,28	0,00	0,05	2,01	0,03
6,01	*0,00*	*6,00*	*0,07*	*6,07*	*0,00*	*0,04*	*1,10*	*0,03*
5,97	0,03	6,00	0,20	6,23	0,00	0,04	1,29	0,03
6,00	0,01	6,00	0,27	6,27	0,00	0,05	1,91	0,03
6,05	0,00	6,00	0,06	6,06	0,00	0,03	1,36	0,02

5,99	0,01	6,00	0,12	6,13	0,00	0,04	1,27	0,02
5,97	0,03	6,00	0,23	6,26	0,00	0,03	1,47	0,01
6,00	0,00	6,00	0,20	6,20	0,00	0,05	1,92	0,03
6,04	0,00	6,00	0,04	6,04	0,00	0,04	1,49	0,02

Mg	Z- and Y-site$_{tot}$	Ca	Na	K	X-site □	X-site $_{tot}$	Na/(Na+ K)
1,51	8,99	0,17	0,68	0,01	0,14	0,86	0,99
1,68	*8,99*	*0,19*	*0,60*	*0,00*	*0,21*	*0,79*	*0,99*
1,83	9,01	0,19	0,60	0,01	0,20	0,80	0,99
1,42	8,99	0,13	0,63	0,01	0,24	0,76	0,99
1,75	*8,97*	*0,21*	*0,61*	*0,01*	*0,17*	*0,83*	*0,99*
1,80	9,02	0,25	0,60	0,01	0,15	0,86	0,99
1,61	9,00	0,16	0,63	0,01	0,20	0,80	0,99
1,65	8,99	0,21	0,63	0,01	0,16	0,84	0,99
1,56	9,00	0,16	0,64	0,00	0,20	0,80	1,00
1,47	9,01	0,14	0,62	0,00	0,24	0,76	0,99
1,22	8,97	0,08	0,57	0,01	0,34	0,66	0,99
1,59	9,01	0,15	0,65	0,01	0,20	0,80	0,99
1,45	9,01	0,16	0,64	0,01	0,20	0,80	0,99
1,66	8,95	0,21	0,54	0,01	0,25	0,75	0,99
1,52	*8,97*	*0,15*	*0,65*	*0,01*	*0,20*	*0,81*	*0,99*
1,64	8,98	0,15	0,65	0,00	0,20	0,80	1,00
1,51	8,98	0,18	0,63	0,01	0,19	0,81	0,99
1,55	8,97	0,15	0,62	0,01	0,23	0,77	0,99
1,61	9,01	0,19	0,62	0,01	0,18	0,82	0,99
1,25	8,96	0,07	0,57	0,01	0,35	0,65	0,99
1,02	8,95	0,07	0,63	0,01	0,28	0,72	0,98
0,99	8,94	0,06	0,60	0,01	0,33	0,68	0,98
1,04	*8,92*	*0,08*	*0,63*	*0,01*	*0,29*	*0,72*	*0,98*
1,04	8,95	0,08	0,62	0,01	0,29	0,71	0,98
1,30	8,95	0,16	0,54	0,01	0,28	0,72	0,98
0,96	*8,94*	*0,07*	*0,58*	*0,01*	*0,33*	*0,67*	*0,98*
0,96	8,95	0,07	0,60	0,01	0,33	0,67	0,99
0,99	8,94	0,07	0,61	0,01	0,31	0,69	0,98
1,55	*8,95*	*0,19*	*0,64*	*0,01*	*0,17*	*0,83*	*0,99*
1,26	8,94	0,13	0,56	0,02	0,29	0,71	0,97
1,05	8,94	0,07	0,61	0,01	0,32	0,69	0,99
1,19	8,94	0,15	0,52	0,01	0,32	0,68	0,98
1,33	8,95	0,16	0,53	0,01	0,30	0,70	0,98
1,05	8,95	0,07	0,61	0,01	0,31	0,69	0,98
1,02	8,94	0,07	0,61	0,01	0,32	0,68	0,98
1,07	8,95	0,07	0,62	0,01	0,31	0,70	0,99
1,49	8,99	0,19	0,65	0,01	0,15	0,85	0,99
1,09	8,95	0,07	0,62	0,01	0,29	0,71	0,98
0,96	8,92	0,06	0,57	0,01	0,36	0,64	0,98
0,97	*8,94*	*0,06*	*0,56*	*0,02*	*0,36*	*0,64*	*0,97*
1,78	8,99	0,11	0,74	0,00	0,16	0,85	0,99
1,76	8,98	0,11	0,72	0,00	0,16	0,84	1,00
1,79	8,99	0,12	0,73	0,00	0,15	0,85	1,00
1,46	9,01	0,06	0,76	0,01	0,17	0,83	0,99
1,67	8,97	0,06	0,63	0,00	0,30	0,70	1,00
1,47	8,99	0,03	0,82	0,00	0,15	0,85	1,00
1,48	9,01	0,03	0,79	0,00	0,18	0,82	0,99
1,05	8,96	0,01	0,75	0,01	0,22	0,78	0,99

1,81	8,98	0,09	0,72	0,00	0,19	0,81	1,00
1,54	*9,01*	*0,08*	*0,75*	*0,01*	*0,16*	*0,84*	*0,99*
1,76	8,99	0,11	0,71	0,01	0,17	0,83	0,99
1,42	9,01	0,03	0,79	0,00	0,17	0,83	0,99
1,63	8,99	0,08	0,79	0,01	0,12	0,88	0,99
1,57	9,02	0,04	0,80	0,01	0,15	0,85	0,99
1,63	8,99	0,07	0,78	0,01	0,15	0,85	0,99
1,63	8,98	0,09	0,76	0,00	0,15	0,85	1,00
1,50	8,99	0,04	0,76	0,01	0,19	0,81	0,99
1,53	*8,98*	*0,06*	*0,79*	*0,01*	*0,15*	*0,85*	*0,99*
1,64	8,98	0,09	0,74	0,01	0,16	0,84	0,99
1,73	*9,00*	*0,11*	*0,72*	*0,01*	*0,16*	*0,84*	*0,99*
1,35	9,25	0,02	0,62	0,01	0,35	0,65	0,99

1,40	9,00	0,04	0,70	0,01	0,25	0,75	0,99
1,42	8,99	0,04	0,71	0,01	0,24	0,76	0,99
1,42	8,99	0,05	0,70	0,01	0,24	0,76	0,99
1,36	8,95	0,04	0,71	0,01	0,25	0,76	0,99
1,39	9,00	0,03	0,73	0,01	0,24	0,76	0,99
1,47	8,98	0,06	0,72	0,01	0,21	0,79	0,99
1,35	*8,97*	*0,06*	*0,66*	*0,01*	*0,27*	*0,73*	*0,99*
1,50	8,98	0,04	0,73	0,01	0,23	0,77	0,99
1,60	8,93	0,21	0,49	0,01	0,29	0,71	0,99
0,95	8,96	0,02	0,64	0,00	0,34	0,66	0,99
1,37	8,97	0,03	0,72	0,01	0,24	0,76	0,99
1,36	8,99	0,03	0,70	0,00	0,26	0,74	0,99
1,41	8,99	0,03	0,69	0,01	0,27	0,73	0,99
1,43	*9,00*	*0,03*	*0,74*	*0,01*	*0,22*	*0,78*	*0,98*
1,05	8,97	0,02	0,68	0,01	0,29	0,71	0,99
1,20	*8,97*	*0,02*	*0,73*	*0,01*	*0,24*	*0,76*	*0,99*
1,11	8,99	0,02	0,69	0,01	0,28	0,72	0,99
1,41	*8,97*	*0,04*	*0,71*	*0,01*	*0,25*	*0,75*	*0,99*
1,41	8,97	0,04	0,72	0,03	0,22	0,78	0,96
0,91	8,97	0,01	0,61	0,01	0,38	0,62	0,99

0,98	8,92	0,01	0,58	0,01	0,41	0,59	0,99
1,36	*8,98*	*0,02*	*0,77*	*0,00*	*0,20*	*0,80*	*0,99*
1,18	8,96	0,02	0,76	0,01	0,21	0,79	0,99
0,92	*8,96*	*0,03*	*0,66*	*0,00*	*0,31*	*0,69*	*1,00*
1,23	8,98	0,02	0,78	0,01	0,19	0,81	0,99
0,83	*8,96*	*0,01*	*0,72*	*0,01*	*0,27*	*0,73*	*0,99*
1,18	8,95	0,03	0,63	0,00	0,34	0,66	1,00
0,57	8,92	0,01	0,54	0,00	0,45	0,55	1,00
0,68	*8,94*	*0,01*	*0,57*	*0,00*	*0,41*	*0,59*	*0,99*
1,37	8,98	0,08	0,71	0,01	0,20	0,80	0,99
1,81	8,96	0,12	0,70	0,00	0,17	0,83	0,99
0,67	9,00	0,01	0,58	0,00	0,42	0,59	1,00
0,61	8,96	0,01	0,69	0,01	0,29	0,71	0,99
1,72	*8,95*	*0,11*	*0,71*	*0,01*	*0,18*	*0,82*	*0,99*
1,41	8,96	0,03	0,76	0,01	0,21	0,79	0,99
0,72	8,98	0,01	0,67	0,01	0,32	0,68	0,99
1,46	8,93	0,03	0,76	0,01	0,20	0,80	0,98

1,49	8,94	0,09	0,73	0,01	0,17	0,83	0,99
1,23	8,97	0,02	0,76	0,01	0,22	0,78	0,99
0,78	8,98	0,02	0,69	0,01	0,28	0,72	0,99
1,35	8,94	0,02	0,81	0,00	0,17	0,83	1,00

Na/(Na + Ca)	X-site □ /(Na + X-site □)	(OH, F)	Fe/(Fe + Mg)	Tourmaline composition
0,80	0,17	4,00	0,49	dravite
0,76	*0,26*	*4,00*	*0,41*	*dravite*
0,76	0,25	4,00	0,38	dravite
0,83	0,28	4,00	0,49	dravite
0,74	*0,22*	*4,00*	*0,40*	*dravite*
0,70	0,20	4,00	0,43	dravite
0,79	0,24	4,00	0,46	dravite
0,75	0,20	4,00	0,44	dravite
0,80	0,24	4,00	0,46	dravite
0,82	0,28	4,00	0,48	dravite
0,87	0,38	4,00	0,54	schorl
0,82	0,24	4,00	0,46	dravite
0,80	0,24	4,00	0,51	schorl
0,72	0,32	4,00	0,39	dravite
0,81	*0,23*	*4,00*	*0,47*	*dravite*
0,81	0,24	4,00	0,43	dravite
0,78	0,23	4,00	0,48	dravite
0,81	0,27	4,00	0,46	dravite
0,76	0,23	4,00	0,46	dravite
0,89	0,38	4,00	0,53	schorl
0,90	0,31	4,00	0,58	schorl
0,91	0,35	4,00	0,59	schorl
0,89	*0,31*	*4,00*	*0,57*	*schorl*
0,89	0,32	4,00	0,57	schorl
0,77	0,34	4,00	0,50	dravite
0,89	*0,36*	*4,00*	*0,59*	*schorl*
0,90	0,35	4,00	0,59	schorl
0,90	0,34	4,00	0,59	schorl
0,78	*0,21*	*4,00*	*0,48*	*dravite*
0,81	0,34	4,00	0,50	schorl
0,90	0,34	4,00	0,57	schorl
0,78	0,38	4,00	0,53	schorl
0,77	0,36	4,00	0,49	dravite
0,89	0,34	4,00	0,58	schorl
0,90	0,34	4,00	0,58	schorl
0,90	0,33	4,00	0,57	schorl
0,78	0,19	4,00	0,50	schorl
0,90	0,32	4,00	0,56	schorl
0,90	0,39	4,00	0,58	schorl
0,90	*0,40*	*4,00*	*0,58*	*schorl*
0,87	0,17	4,00	0,39	dravite
0,86	0,19	4,00	0,39	dravite
0,86	0,17	4,00	0,38	dravite
0,92	0,19	4,00	0,50	dravite
0,91	0,32	4,00	0,38	dravite
0,97	0,15	4,00	0,49	dravite
0,96	0,19	4,00	0,49	dravite
0,98	0,23	4,00	0,61	schorl

0,89	0,21	4,00	0,38	dravite
0,90	*0,18*	*4,00*	*0,47*	*dravite*
0,87	0,20	4,00	0,39	dravite
0,96	0,18	4,00	0,50	schorl
0,91	0,13	4,00	0,45	dravite
0,95	0,16	4,00	0,47	dravite
0,92	0,16	4,00	0,44	dravite
0,90	0,16	4,00	0,44	dravite
0,95	0,20	4,00	0,47	dravite
0,93	*0,16*	*4,00*	*0,46*	*dravite*
0,89	0,18	4,00	0,44	dravite
0,87	*0,18*	*4,00*	*0,40*	*dravite*
0,97	0,36	4,00	0,60	schorl

0,95	0,26	4,00	0,50	dravite
0,94	0,25	4,00	0,49	dravite
0,93	0,25	4,00	0,49	dravite
0,95	0,26	4,00	0,50	schorl
0,96	0,25	4,00	0,50	dravite
0,93	0,23	4,00	0,48	dravite
0,92	*0,29*	*4,00*	*0,50*	*schorl*
0,95	0,24	4,00	0,47	dravite
0,70	0,37	4,00	0,39	dravite
0,97	0,35	4,00	0,64	schorl
0,96	0,25	4,00	0,50	schorl
0,96	0,27	4,00	0,51	schorl
0,96	0,28	4,00	0,49	dravite
0,96	*0,23*	*4,00*	*0,50*	*dravite*
0,97	0,30	4,00	0,61	schorl
0,97	*0,25*	*4,00*	*0,56*	*schorl*
0,97	0,29	4,00	0,59	schorl
0,94	*0,26*	*4,00*	*0,49*	*dravite*
0,95	0,23	4,00	0,51	schorl
0,98	0,38	4,00	0,65	schorl

0,99	0,41	4,00	0,58	schorl
0,98	*0,21*	*4,00*	*0,51*	*schorl*
0,97	0,22	4,00	0,57	schorl
0,96	*0,32*	*4,00*	*0,65*	*schorl*
0,97	0,19	4,00	0,56	schorl
0,99	*0,27*	*4,00*	*0,68*	*schorl*
0,95	0,35	4,00	0,53	schorl
0,99	0,45	4,00	0,76	schorl
0,98	*0,42*	*4,00*	*0,72*	*schorl*
0,90	0,22	4,00	0,52	schorl
0,85	0,19	4,00	0,37	dravite
0,99	0,42	4,00	0,73	schorl
0,99	0,30	4,00	0,77	schorl
0,87	*0,20*	*4,00*	*0,39*	*dravite*
0,96	0,21	4,00	0,48	dravite
0,99	0,32	4,00	0,73	schorl
0,96	0,21	4,00	0,48	dravite

0,89	0,19	4,00	0,46	dravite
0,98	0,23	4,00	0,55	schorl
0,98	0,29	4,00	0,71	schorl
0,98	0,17	4,00	0,52	schorl